PACIFIC EARTHQUAKE ENGINEERING
RESEARCH CENTER

Application of the PEER PBEE Methodology to the I-880 Viaduct

I-880 Testbed Committee

Sashi K. Kunnath
Testbed Coordinator
University of California, Davis

PEER 2006/10
FEBRUARY 2007

Application of the PEER PBEE Methodology to the I-880 Viaduct

I-880 Testbed Committee

Sashi K. Kunnath
Testbed Coordinator
Department of Civil and Environmental Engineering
University of California, Davis

PEER Report 2006/10
Pacific Earthquake Engineering Research Center
College of Engineering
University of California, Berkeley

February 2007

ABSTRACT

This report summarizes the efforts of several investigators involved in reviewing, assessing, and applying the PEER performance-based methodology (PBM) to an existing viaduct in California. The expected seismic performance of the 5th and 6th Street viaduct, denoted in this report as the I-880 viaduct, is investigated probabilistically within the context of the PEER framework. The PEER approach consists of four essential components: development of a site-specific hazard curve; estimation of seismic demands given a set of ground motions consistent with the site hazard; prediction of damage measures as a function of the computed demands; and evaluation of the influence of the damage measures on selected decision variables. The damage measures considered in this study are the spalling of the column cover concrete and buckling of the longitudinal reinforcement in the columns, and the decision variable of primary focus is the probability of closure of the viaduct.

The evaluation presented in this report examines the performance of a three-frame section of the I-880 viaduct subjected to a series of ground motions representing three hazard levels. Fragility functions for demand, damage, and economic loss are derived, and the total probability theorem implied in the PEER framework equation is applied to estimate the closure probability of the bridge using the specified hazard at the site. Also included in the study is a reliability analysis of the simulation model to gain an understanding of model sensitivity to the demand estimates. A practitioner perspective of the PEER methodology in the context of seismic bridge design provides insight into the current state of practice and an outlook on the future of probabilistic PBM in engineering practice.

ACKNOWLEDGMENTS

This work was supported primarily by the Earthquake Engineering Research Centers Program of the National Science Foundation under award number EEC-9701568 through the Pacific Earthquake Engineering Research (PEER) Center.

The contributions of UC Davis graduate students Keith Bauer, Anna von Felten, and Leah Larson to the contents of Chapters 2, 3, and 5 are gratefully acknowledged.

Any opinions, findings, and conclusions or recommendations expressed in this material are those of the authors and do not necessarily reflect those of the National Science Foundation.

CONTENTS

LIST OF FIGURES

LIST OF TABLES

1 Introduction

Sashi K. Kunnath[1] and Terje Haukaas[2]
[1]*University of California, Davis*
[2]*University of British Columbia, Vancouver, Canada*

Performance-based earthquake engineering (PBEE) is an emerging framework that seeks to go beyond traditional design practice and address issues related to safety, functionality, and economy from the perspective of all stakeholders of the facility. The release of FEMA-356 (2000) is now widely recognized as the first resource document that lays out a comprehensive and systematic approach to PBEE. However, earlier efforts undertaken by the Structural Engineers Association of California (SEAOC) which led to development of Vision 2000 (Office of Emergency Services 1995) and the Conceptual Framework for Performance-Based Seismic Design (SEAOC 1999) can be regarded as precursors to the FEMA effort.

FEMA-356 is essentially a deterministic approach to PBEE. The range of uncertainties associated with predicting performance in a seismic environment has led to increased interest in probabilistic performance-based methods. A formal implementation utilizing a probabilistic treatment for seismic evaluation materialized with FEMA-350 (2000). The PEER performance-based framework may be regarded as an extension and an enhancement of the procedure developed for FEMA-350 (Cornell et al. 2002). The PEER framework is the first PBEE approach that incorporates loss modeling and provides an economic basis for evaluating future performance in probabilistic terms.

The I-880 testbed is one of several testbed projects conceived and developed by PEER to both demonstrate and evaluate the PEER methodology on real facilities of reasonable size and complexity. The I-880 testbed is a section of the rebuilt Caltrans-designed Interstate 880 known as the 5th and 6th Street viaduct and is located in Oakland, California. This report presents a comprehensive summary of the modeling, evaluation, and performance-based assessment of a selected section of the viaduct.

1.1 BASIC CONCEPTS IN PROBABILITY

It is recognized that practicing engineers — one of the target audiences for this report — are often unfamiliar with the concepts of reliability analysis. An effort is therefore made in the following discussion to provide a brief introduction to some of the concepts required to appreciate the presented methodology and results. Naturally, this report does not allow an in-depth review. The interested reader is urged to further explore the extensive literature on probabilistic analysis and structural reliability.

Consider an event of interest, denoted by E_1, for instance the event that a structural response exceeds a specific threshold. The probability that the event E_1 will occur is a number between 0 and 1, denoted $\mathrm{P}(E_1)$. $\mathrm{P}(E_1)=0$ signifies that the event is certain *not* to occur, while $\mathrm{P}(E_1)=1$ indicates that the event certainly *will* occur.

When dealing with multiple events it is often of interest to determine the probability that different events will occur simultaneously, or the probability that any one of selected events will occur. Symbols from the field of set theory are employed to specify such composite events: the intersection symbol, $\cap$, and the union symbol, $\cup$. For instance, the probability that *both* events E_1 and E_2 will occur is denoted $\mathrm{P}(E_1 \cap E_2)$. Conversely, the probability that *either* event E_1 or E_2 will occur is denoted $\mathrm{P}(E_1 \cup E_2)$. A third symbol is employed to denote *conditional* events. The probability $\mathrm{P}(E_1 \mid E_2)$ is read "the probability that E_1 will occur *given* that E_2 has occurred." This is called a conditional probability, which is a key ingredient in the PEER equation discussed below.

Several rules of probability apply when dealing with multiple events. These rules are all based on three fundamental axioms of probability. They state that (a) any probability is a number greater than or equal to 0, (b) the probability of the certain event is equal to 1, and (c) $\mathrm{P}(E_1 \cup E_2) = \mathrm{P}(E_1) + \mathrm{P}(E_2)$ for two mutually exclusive events E_1 and E_2. "Mutually exclusive" refers to the situation in which the events cannot happen simultaneously.

Of the rules that are derived from the axioms we will first devote attention to the conditional probability rule. It states that the conditional probability $\mathrm{P}(E_1 \mid E_2)$ is equal to the fraction $\mathrm{P}(E_1 \cap E_2)/\mathrm{P}(E_2)$. An obvious consequence of this rule is the multiplication rule, which reads $\mathrm{P}(E_1 \cap E_2) = \mathrm{P}(E_1 \mid E_2)\mathrm{P}(E_2)$. The significance of this rule becomes apparent when the concept of statistical independence is introduced. Two events E_1 and E_2 are said to be statistically independent if $\mathrm{P}(E_1 \mid E_2) = \mathrm{P}(E_1)$, or equivalently, if $\mathrm{P}(E_2 \mid E_1) = \mathrm{P}(E_2)$. In other words, two events are statistically independent if knowledge of the occurrence of one event does not affect the probability of occurrence of the other. From the multiplication rule we derive the important result that $\mathrm{P}(E_1 \cap E_2) = \mathrm{P}(E_1) \cdot \mathrm{P}(E_2)$ for two statistically independent events, E_1 and E_2. The issue of statistical independence is a subtle concept that must not be confused with events being mutually exclusive or not. Specifically, the probability that two statistically independent events will occur simultaneously is generally nonzero.

1.1.1 Random Variables and Probability Distributions

In the context of this report it is useful to extend the probabilistic concepts to include random variables. The parameters of a structural analysis (material properties, geometry, loads, and responses) are continuous variables with, generally, uncertain outcome. This makes them amenable to characterization as continuous random variables. The relative likelihood of different outcomes of a random variable of this type is available in its probability density function (PDF), or equivalently, its cumulative distribution function (CDF). For a random variable x these functions are written $f(x)$ and $F(x)$, respectively. In the literature the formal notational distinction is often made between the random variable and its outcome; a subtlety that is neglected here for brevity. The PDF assigns probability density to the range of possible outcomes of x and must be integrated to obtain a probability. For example, the integral $\int_{2.0}^{5.0} f(x)\mathrm{d}x$ provides the probability that the outcome of x will lie between 2.0 and 5.0. Conversely, the CDF $F(5.0)$ provides the probability that the outcome x will be less than or equal to 5.0. In the context of structural reliability it is useful to introduce the cumulative CDF (CCDF), which denotes the probability that the random variable, for example a response quantity, will *exceed* a certain value. The CCDF is herein denoted $G(x)$, so that $G(5.0)$ indicates the probability that the outcome of x will exceed 5.0. In passing it is noted that the PDF is obtained by differentiation of the CDF or CCDF: $f(x) = dF(x)/dx = \left| dG(x)/dx \right|$.

Numerous probability distribution *types* are available to characterize the probability distribution of continuous random variables. Examples include the normal, lognormal, and uniform distributions. For some parameters the distribution type is obvious from the physics of the problem, while oftentimes data fitting and judgment are required to select an appropriate distribution type. The lognormal distribution is often appealing in structural modeling and analysis because it allows only positive-valued outcomes and because of its close relationship with the fundamental normal distribution. In fact, the lognormal distribution is selected for a number of random variables in this study.

Random variables may be *correlated*; a concept related to the concept of statistical dependence introduced above. The correlation coefficient ρ_{12} between the two random variables x_1 and x_2 is a number between -1 and 1. ρ_{12}=1 signifies that the random variables are perfectly correlated; that is, their outcomes are directly proportional. Conversely, ρ_{12}=-1 indicates that they are inversely proportional. The reader is cautioned, however, that two *uncorrelated* random variables may not be entirely statistically independent. Correlation is merely a measure of *linear* statistical dependence between random variables. Hence, tendencies of higher order dependence, for example that the outcome of x_2 tends to be close to the square of the value of x_1 is not captured by the correlation coefficient.

1.1.2 Total Probability Theorem

Several of the rules of probability are applicable to random variables. Of particular interest in this study is the total probability theorem, which for events $A, E_1, E_2, \ldots, E_N$ reads

$$P(A) = \sum_{i=1}^{N} \mathrm{P}(A \mid E_i)\mathrm{P}(E_i) \tag{1.1}$$

where E_i represents a collection of mutually exclusive and collectively exhaustive events. In other words, none of the events E_i can happen simultaneously, and the probability of their union is equal to unity. The significance of Equation (1.1) lies in the fact that knowledge of the conditional probabilities $\mathrm{P}(A \mid E_i)$ and the individual probabilities $\mathrm{P}(E_i)$ enables the computation of the unconditional probability P(A). Translated into the domain of continuous random variables, the total probability theorem to obtain the CCDF of a random variable x is an integral of the form:

$$G(x) = \int_{-\infty}^{\infty} \mathrm{G}(x \mid y)\mathrm{f}(y)\mathrm{d}y \tag{1.2}$$

where the integration is performed over the entire outcome range of the continuous random variable y, and the conditional CCDF $\mathrm{G}(x \mid y)$ is interpreted as the CCDF of x given a certain outcome of y.

1.2 PEER PERFORMANCE-BASED FRAMEWORK

The PEER evaluation methodology is summarized in Figure 1.1. The methodology comprises four distinct but related phases: *hazard analysis* that characterizes the seismicity at the site; *structural analysis* of a simulation model that yields the necessary force and deformation measures; *damage analysis* to enable transformation of response measures into physical states of damage; and *loss analysis* that relates the damage to a measure of performance.

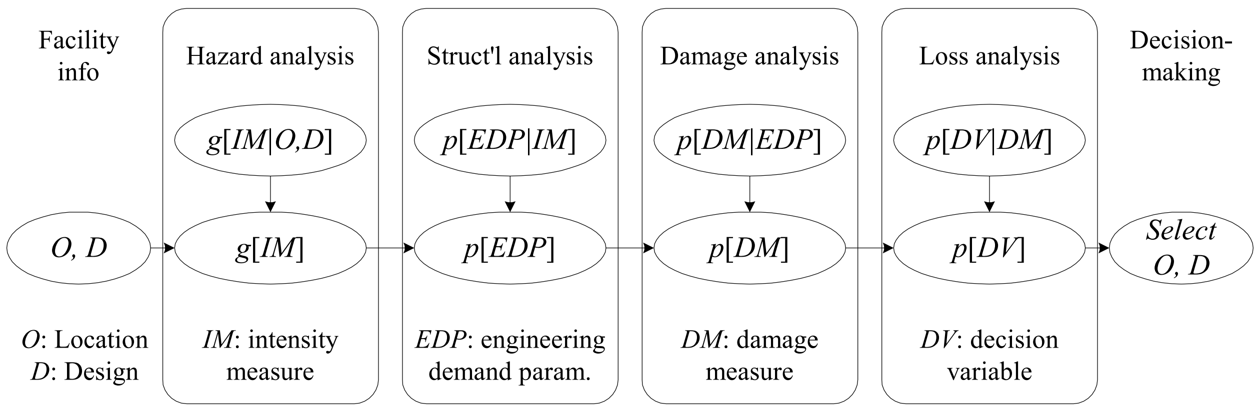

Fig. 1.1 PEER performance-based evaluation framework

Figure 1.1 also introduces abbreviations to describe measures of intensity, response, damage, and loss estimates. These abbreviations will be used liberally throughout this report and are, therefore, described briefly in the following paragraphs.

Intensity Measures (*IM*s). This denotes a measure of ground motion intensity. Several choices of this measure are possible: peak ground acceleration, spectral acceleration, and magnitude at some characteristic period of the structure. Recommendations have also been made to utilize a vector of *IM*s instead of simple scalar measures. Baker and Cornell (2004) recently proposed a method for determining an optimal vector of *IM*s for use in performance-based evaluation.

Engineering Demand Parameters (*EDP*s). Seismic demand needs to be characterized by a limited set of response measures that are referred to as *EDP*s. In the case of building structures, the displacement at the roof of the structure or the interstory drift ratio is a typical response measure that can be correlated with damage and performance. Other examples of demand parameters include: forces, stresses, strains, and cumulative measures such as plastic deformation and dissipated energy. For bridge structures a larger subset of response measures exists. Damage to bridges can result from movement of the foundation, substructure, or superstructure. Hence, in a realistic evaluation, it may be necessary to monitor a vector of *EDP*s. In the PEER framework, the measure of interest is the conditional probability p(*EDP*|*IM*). The choice of the *EDP* for the I-880 study will be discussed in Chapter 3.

Damage Measures (*DM*s). This refers to the conversion of response measures to quantifiable damage states. For bridge structures, possible damage states that can be identified during post-event bridge inspection include amount and degree of concrete spalling, buckling of longitudinal reinforcing bars, fracture of transverse reinforcement, and horizontal and vertical offsets at expansion joints. In the context of the PEER methodology, damage needs to be expressed as a fragility function for different response measures. Hence the outcome of a damage analysis will yield p(*DM*|*EDP*). It is clear that the damage measure relies on the choice of the *EDP*. Once a fragility curve (cumulative distribution function) is established for a defined damage state and p(*EDP*) is computed, it becomes possible to estimate p(*DM*). The outcome of this phase provides the essential ingredients to complete the next and final phase in the PEER PBEE evaluation process.

Decision Variables (*DV*s). It is expected that the performance of a structure be defined as a discrete or continuous function with realistic decision-making potential. Such a loss-modeling measure is defined as a *DV* in the PEER framework. An example of a *DV* for building evaluation is mean annual loss, for bridges the critical *DV* is the likelihood of closure of the facility. In either case, the *DV*s must be correlated with damage measures (*DM*s) selected in the previous phase so that p(*DV*|*DM*) can be calculated. If the measured damage is conditioned on the intensity measure so that p(*DM*|*IM*) is obtained, it is feasible to assess performance for different hazard levels.

Equation (1.2) forms the basis for the PEER equation, in which the CCDF of a decision variable (*DV*) is computed based on knowledge of conditional probabilities involving the structural performance. In this framework, structural performance is specified in terms of structural response quantities, which have previously been classified as engineering demand parameters (*EDP*s) which, in turn, are functions of the ground motion intensity, or intensity measures (*IM*s). On the other hand, from an owner's or decision-maker's perspective, performance events must be defined in terms of the decision variables, *DV*s, which characterize the cost and/or risk associated with different structural performance outcomes, e.g., the costs of repair and loss of function of a bridge as a result of an earthquake. *DV*s in general depend on the state of the structure as characterized by a set of damage measures (*DM*s). For example, different levels of drift may be used as indicators of different levels of damage to a bridge or building. *DM*s in general are functions of *EDP*s. Thus, one can write *DV*(*DM*(*EDP*(*IM*))). Each of the relationships *DV*(*DM*), *DM*(*EDP*) and *EDP*(*IM*) is, ideally, a probabilistic model that produces a conditional probability. For instance, researchers that study damage models enables the computation of the conditional CCDF $G(DM|EDP)$, that is, the probability that the damage will exceed a certain threshold *given* a certain value of the *EDP*. Some of these models are well developed, while others are subjects of current research within and outside PEER.

To understand the role of the total probability theorem in the development of the PEER equation, assume first that the PDF of the intensity measure, $f(IM)$ is available (an extension to the mean annual frequency is presented below). The total probability theorem in the form of Equation (1.2) is then applied to obtain the CCDF of the *EDP*:

$$G(EDP) = \int_0^\infty \mathrm{G}\left(EDP \mid IM\right) \mathrm{f}\left(IM\right) \mathrm{d}IM \tag{1.3}$$

The corresponding PDF is obtained by differentiation: $f(EDP) = \left| \mathrm{d}G(EDP) / \mathrm{d}EDP \right|$. With knowledge of the PDF of the engineering demand parameter, the theorem is subsequently applied to obtain the probability distribution for the damage measure, and thereafter to obtain the probability distribution for the decision variable. The combination of all equations leads to the triple integral:

$$G(DV) = \int_0^\infty \int_0^\infty \int_0^\infty \mathrm{G}\left(DV \mid DM\right) \left| \frac{\mathrm{d}G\left(DM \mid EDP\right)}{\mathrm{d}DM} \right| \left| \frac{\mathrm{d}G\left(EDP \mid IM\right)}{\mathrm{d}EDP} \right| \mathrm{f}\left(IM\right) \ \mathrm{d}IM \ \ \mathrm{d}EDP \ \ \mathrm{d}DM \tag{1.4}$$

Equation (1.4) is a variation of the PEER integral. However, in the above derivation it is assumed that *IM* is a random variable that represents the value of the intensity of the impending earthquake. Rather, in the PEER framework it is common to introduce a probabilistic occurrence model to describe the probability of occurrence of earthquakes of varying intensity. The Poisson process is the most frequently employed occurrence model in engineering practice. At each intensity level this process is uniquely defined by one parameter; the mean rate of occurrence, here denoted λ. If the time axis is in years, then λ is equal to the mean annual frequency. The mean rate λ as a function of *IM*, namely $\lambda(IM)$, is interpreted as a seismic hazard curve, which is determined, e.g., by probabilistic seismic hazard analysis. Notably, $\lambda(IM)$ is interpreted as a cumulative distribution function that is differentiated with respect to *IM* before replacing *f*(*IM*) in (1.4). Consequently, (1.4) is written as follows:

$$\lambda(DV) = \int_0^\infty \int_0^\infty \int_0^\infty \mathrm{G}(DV \mid DM) \; \left|\mathrm{d}G(DM \mid EDP)\right| \; \left|\mathrm{d}G(EDP \mid IM)\right| \; \left|\mathrm{d}\lambda(IM)\right| \tag{1.5}$$

In Equation (1.5), $\nu(DV)$ is the mean annual rate of a decision variable exceeding some threshold value *DV; DM* represents the damage measure; *EDP* is the selected engineering demand parameter (such as drift, plastic rotation, etc.); and *IM* represents the intensity measure. $d\lambda(IM)$ is the differential of the mean annual frequency of exceeding the intensity measure (which for small values is equal to the annual probability of exceedance of the intensity measure). It is necessary to use the absolute value of this quantity because the derivative (slope of the hazard curve) is negative. The expression of the form $G(A|B)$ is the complementary cumulative distribution function or the conditional probability that *A* exceeds a specified limit for a given value of *B*. The term of the form $dG(A|B)$ is the derivative with respect to *A* of the conditional probability $G(A|B)$. One useful partial result of Equation (1.5) results prior to the integration over $d\lambda(IM)$, which provides information about the variation of the $G(DV)$ as a function of *IM*. The advantage offered in expressing the methodology in the above format is that it lends itself to intermediate results of considerable value. These capabilities will be demonstrated later in this report as part of the I-880 testbed studies.

An important issue in probabilistic PBEE is the treatment of uncertainties that arise in each step of the process. While rigorous approaches exist to incorporate the propagation of uncertainties, this study is concerned with identifying opportunities to reduce uncertainty by improved modeling strategies.

1.3 OBJECTIVE AND SCOPE OF REPORT

PEER's methodology has now evolved to a point that validation exercises are expected to reveal strengths in the approach that researchers can continue to build upon, and drawbacks in the process that merit further scrutiny. The testbed project seeks to synthesize PEER's research efforts into a coherent methodology and to demonstrate and exercise that methodology on real facilities. In this study, the facility under consideration, one of six such "application" testbed projects, is a relatively new highway bridge structure built to current Caltrans specifications. This structure was selected for several reasons: it represents a new design with structural and geotechnical features that pose formidable modeling challenges; it permits application of all components of the PEER PBEE framework equation (Eq. 1.1); and the seismic performance of the viaduct is critical to the transportation network in the region.

Chapter 2 of this report will describe the I-880 structure and identify pertinent details of typical foundation, substructure and superstructure elements. This section will also outline the development of the simulation models used in the time-history analyses. Chapter 3 discusses uncertainty and reliability analyses to examine the sensitivity of model variables used in the simulation exercises. Since the PEER approach is probabilistic, an understanding of the sensitivities of model parameters will be useful in identifying the features of the model that can assist in minimizing the effects of epistemic uncertainties. The next chapter deals with hazard analysis at the I-880 bridge site and the selection and scaling of ground motions. The results of the numerical simulation of seismic demands are also summarized in this chapter. Damage analyses and the development of the fragility functions for use in the performance assessment of the viaduct are presented in Chapter 5. The third and final step in implementing the PEER framework equation, namely, loss modeling, forms the focus of the sixth chapter. One possible approach to incorporating a decision variable is introduced, and the closure probability of the viaduct is evaluated within the context of the variables used in the study to characterize demand and damage. Following the application of the PEER methodology to evaluate the seismic performance of the viaduct, the seventh chapter presents a practitioner perspective wherein the PEER methodology is compared to current practice in order to identify the merits of the methodology, its relevance in advancing the state of the art, and the issues and concerns in implementing the procedure in engineering practice.

2 I-880 Simulation Model

Sashi Kunnath and Boris Jeremić
University of California, Davis

In this chapter the development of an appropriate simulation model of a selected section of the viaduct is described. The simulation model is developed for use with OpenSees (2004), an open-source finite element software platform developed by PEER researchers. Consequently, the modeling of the viaduct conforms to element and material models available in the OpenSees framework. Prior to detailing the model development, a brief description of the highway bridge structure is presented.

2.1 DESCRIPTION OF I-880 VIADUCT

The 1989 Loma Prieta earthquake caused the collapse of the upper deck of a section of the double-decked Cypress viaduct, the main artery connecting Interstate 880 with Interstate 80 just east of San Francisco. The collapse resulted in 42 fatalities. By mid-1997, a new nondecked viaduct was constructed approximately one-half mile from the old structure, just east of the San Francisco-Oakland Bay Bridge toll plaza. The new viaduct consists of two side-by-side single-bay spans carrying traffic between the Interstate 880-980 split in downtown Oakland at the Macarthur maze (Fig. 2.1). This new viaduct, running from the Interstate 980 south connector ramp to the Union Street ramp, is what is now known as the 5th and 6th Street viaduct.

2.1.1 Structural Details

The specific section of I-880 to be evaluated in this project is a seven-frame structure consisting of 26 spans and a total length of 1138 m. The viaduct consists of two curved sections with radii of 975 m and 743 m, respectively, joined by an approximately straight section 207 m in length. A plan view of the structure is shown in Figure 2.2. Also identified in the figure is the interior segment that comprises frames 3-4-5 which were utilized in a simulation study to determine seismic demands.

Fig. 2.1 Partial view of rebuilt I-880 viaduct

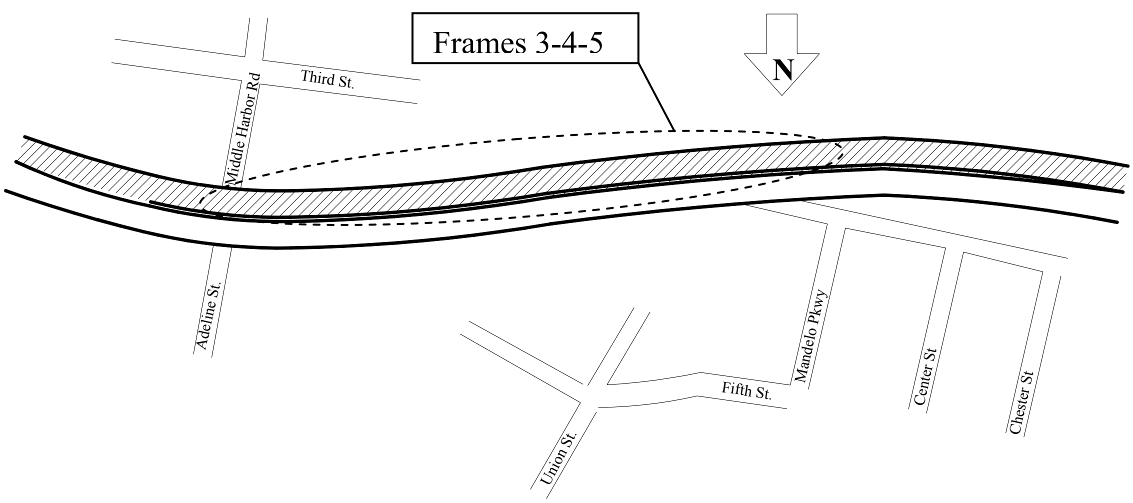

Fig. 2.2 Plan view of viaduct (shaded region is segment considered in study)

The superstructure of the viaduct is composed of 7 cast-in-place reinforced concrete box girders, approximately 22 m wide and 2 m high. A typical box girder section is displayed in Figure 2.3. The substructure, typically designed for a span length of approximately 46.5 m, is composed of 55 rectangular columns with circular reinforcement. Throughout the seven-frame section, 32 of the columns are 2.48 x 2.635 m, 12 are 2.17 m x 2.325 m, and 11 are 1.86 m x 2.015 m. The columns range in total height from approximately 5.2 m to approximately 18 m as measured from the top of the pile-caps to midheight of the superstructure. A majority of the columns have continuous moment connections at the bent pile cap locations, the remaining columns have pinned-connections (shear keys) at the bent pile cap locations. A typical bent cross section is presented in Figure 2.4. The transverse reinforcement for the columns is #8 hoops (25.4 mm diameter) at a center-to-center spacing of 103 mm. The longitudinal reinforcement for the columns consists of number #14 (43.0 mm diameter) bars. In general, the bents have two columns. However, some of the bents have three or four columns at the location of the off-ramp at the west end of the structure, and a few bents have outriggers.

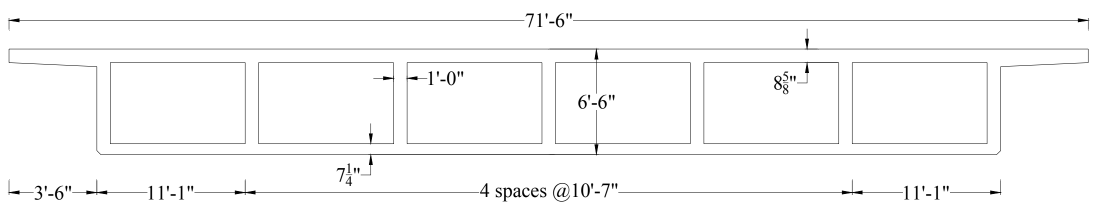

Fig. 2.3 Typical box girder cross section

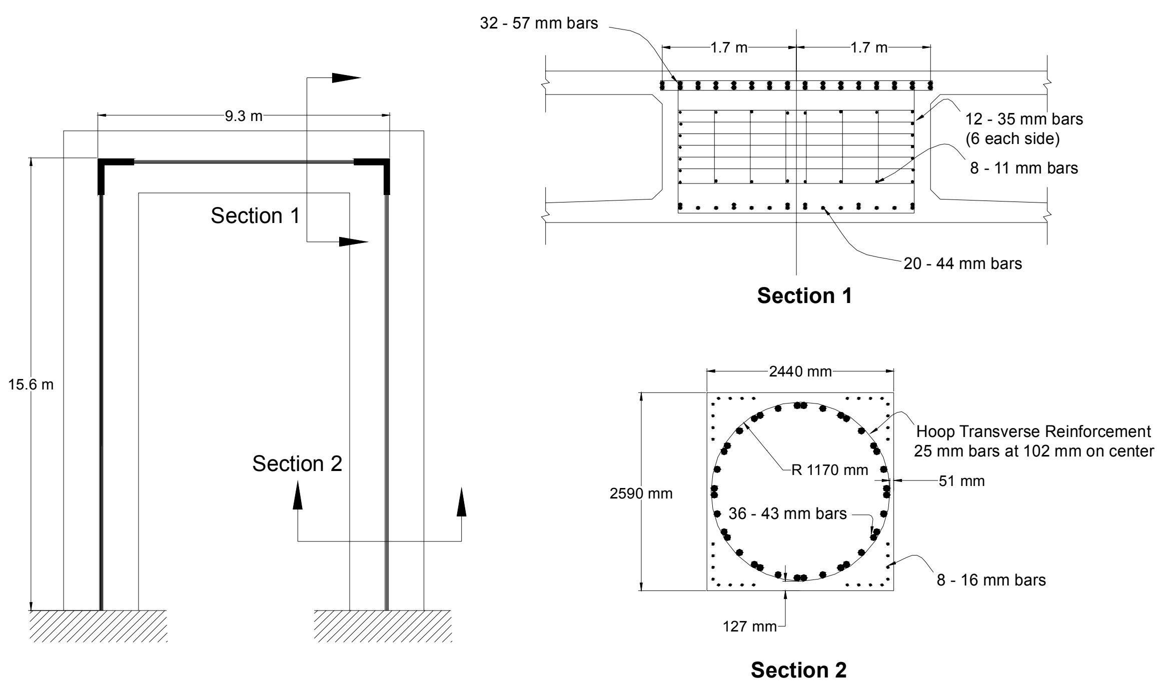

Fig. 2.4 Typical bent column and beam cross sections

2.1.2 Soil and Foundation Details

The soils on the site near the San Francisco Bay consist of dense fill, Bay mud and sand, underlain by deep clay deposits. Figure 2.5 shows the profile of the soil layers underlying the different bents throughout the length of the viaduct. Soft clay is predominant in the upper layers of bents 15–21. The foundation systems for the bents are generally square pile groups of between 15 and 25 piles. Most of the piles are 600 mm in diameter with nominal 400-ton capacity. Four of the bents have 900 mm diameter CIDH piles with 800-ton capacity. A typical 5x5 pile group is shown in Figure 2.6.

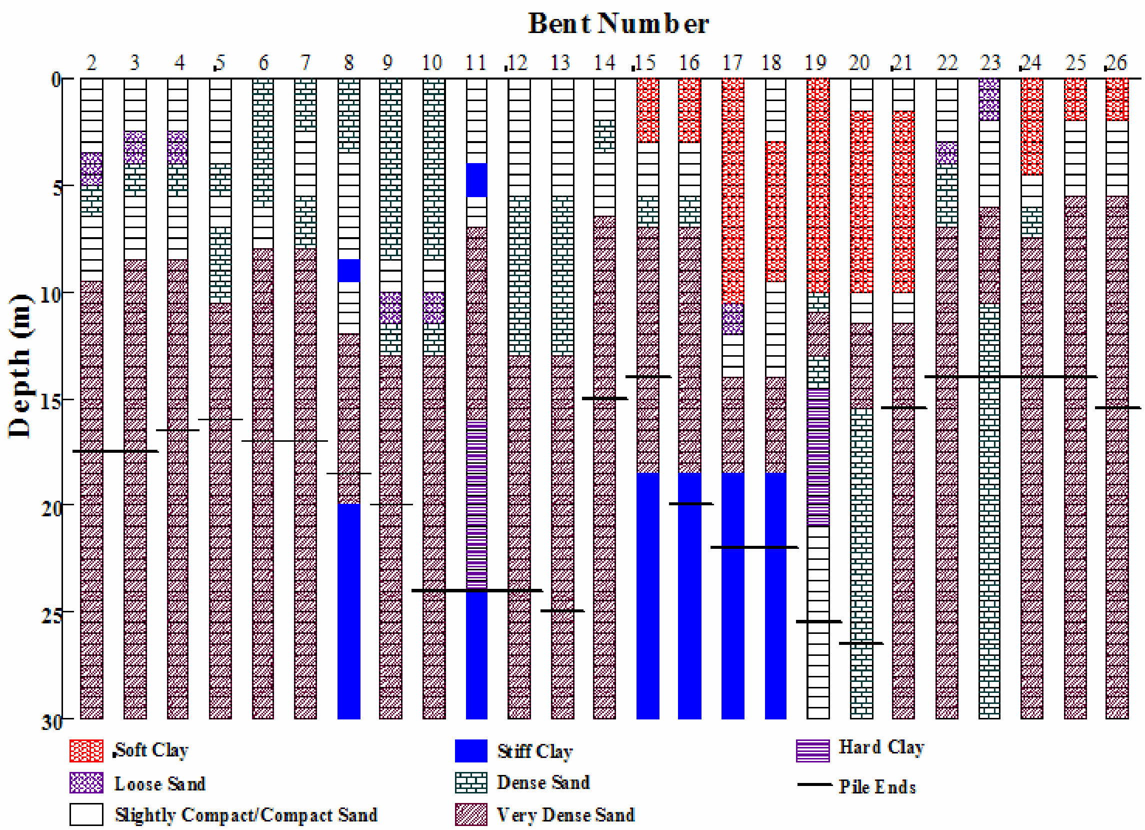

Fig. 2.5 Soil profile beneath each bent (dark horizontal lines indicate termination of pile group beneath that bent)

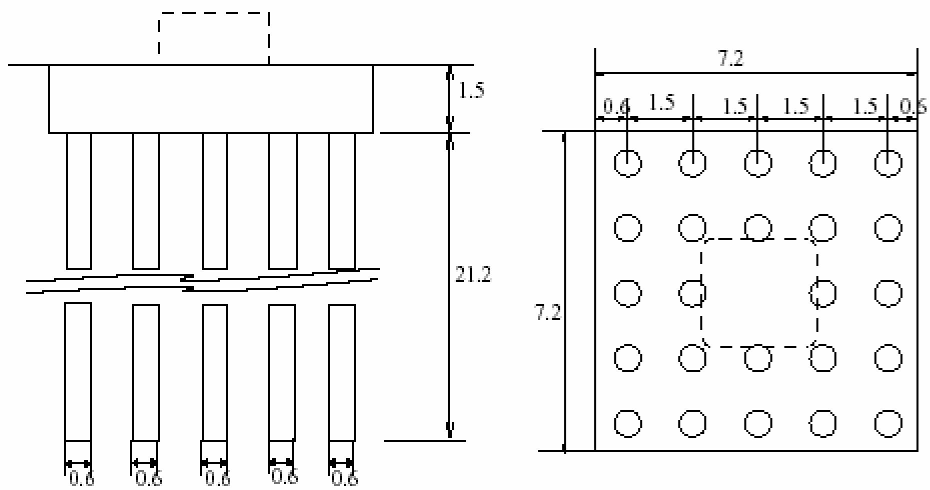

Fig. 2.6 Detail of typical pile cap and 5x5 pile group (in mm)

2.2 SIMULATION MODEL

A schematic of the eastbound bridge identifying the seven frames of the viaduct is shown in Figure 2.7. As indicated earlier, this segment of the I-880 consists of seven frames and twenty-five bents (bents 2–26). The frames are interconnected by expansion joints that comprise shear keys, restrainers, and bearing surfaces. For the purpose of this study it was resolved that a multiple-frame model incorporating at least a pair of expansion joints was essential. Consequently, the simulation model for the seismic demand analyses was derived to represent the section of the viaduct comprising frames 3–5 or bents 10–20. Frame 3 consists of bents 10–13, frame 4 includes bents 14–17, and frame 5 the remaining three bents (18–20), as displayed in Figure 2.7. Expansion joints are located between bents 13–14 and bents 17–18. In analyzing the three-frame model, consideration was given to the possible restraining action and interaction of the adjoining frames (frames 1 and 2 on the east side of the bridge and frames 6 and 7 on the west). Separate studies in which the effective stiffness of the adjoining frames was incorporated indicated that the interaction with these adjoining frames was marginal or negligible. Hence, the results reported in this study do not explicitly consider interaction of adjoining frames.

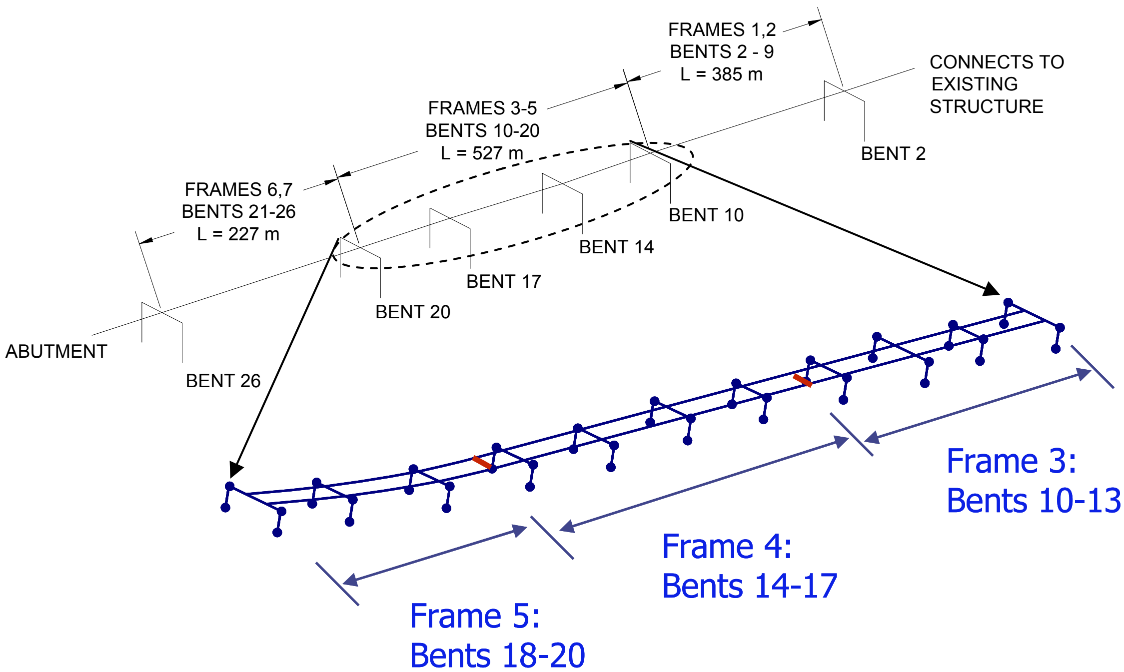

Fig. 2.7 Schematic view of eastbound I-880 viaduct showing frame configuration and selected section used in analytical simulation of seismic demand

Of the different element types used to build the OpenSees simulation model, the properties of the elastic beams and zero-length springs were derived independently (see details in subsequent sections) and input directly as stiffness and strength values. The nonlinear beam column elements used to model the piers are based on a fiber section discretization that requires the specification of constituent material properties. The sectional properties are then computed during the incremental analysis through integration of the sectional stress profile assuming plane sections to remain plane during the deformation. Details of the material and element models are described in the following sections.

2.2.1 Material Properties

The nominal material strengths for the structure are specified in the design drawings. The concrete compressive strength for both the columns and the box girder is specified as 28 MPa (4 ksi). To account for overstrength, as required by Caltrans design specifications, the nominal concrete strength is assumed to be 36 MPa (5.2 ksi) with an elastic modulus of 28,340 MPa

(4,110 ksi). Properties of the core concrete are derived using Mander's confinement model (Mander et al. 1988). The remaining parameters for the concrete model are listed in Table 2.1. Figure 2.8 illustrates the stress-strain parameters based on the Kent-Park (1971) model and denoted in OpenSees as *Concrete01*.

Table 2.1 Concrete material properties

Parameter	Section/region	Definition	Value MPa (ksi)
f'_c	Confined core	Peak compressive Stress	48.0 (6.94)
	Cover		36.0 (5.20)
ε_{co}	Confined core	Strain at peak compressive stress	0.003
	Cover		0.002
f_{cu}	Confined core	Residual stress	9.6 (1.4)
	Cover		0.0
ε_{cu}	Confined core	Strain at ultimate stress	0.02
	Cover		0.006

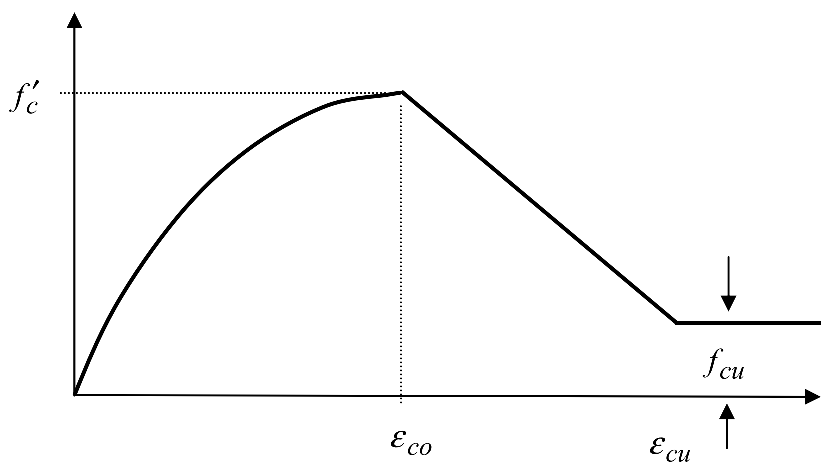

Fig. 2.8 OpenSees *Concrete01* model

The grade 60 longitudinal reinforcing steel used in all the piers is assumed to have a yield strength of 455 MPa (66 ksi). The reinforcing steel was modeled using the *Steel01* bilinear material model in OpenSees with an effective elastic stiffness of 200 GPa and 1% post-yield stiffness. The 19 mm (0.75 in.) nominal diameter longitudinal and vertical restrainer cables in the frame connections are assumed to have an actual yield stress of 1,215 MPa (176 ksi) and elastic modulus of 69,000 MPa (10000 ksi).

2.2.2 Member Modeling

The following element models were utilized to develop a simulation model of the three frames: force-based nonlinear beam-column elements; elastic beam elements; and zero-length spring elements. The pertinent details of the element models are now summarized.

Columns. The piers of the viaduct were considered to be the primary nonlinear elements in the model. Hence, force-based nonlinear beam-column elements that consider the spread of plasticity along the element were used to model the columns of every bent in the viaduct. The column is represented by fiber sections and the element stiffness matrix is derived through integration along the length using a Gauss-Lobatto quadrature rule. Following a separate sensitivity study, it was determined that five integration points and a sectional discretization displayed in Figure 2.9 were appropriate for the nonlinear transient analysis of the viaduct model. The force-based element in conjunction with the fiber model accounts for inelastic axial flexure interaction in bidirectional bending.

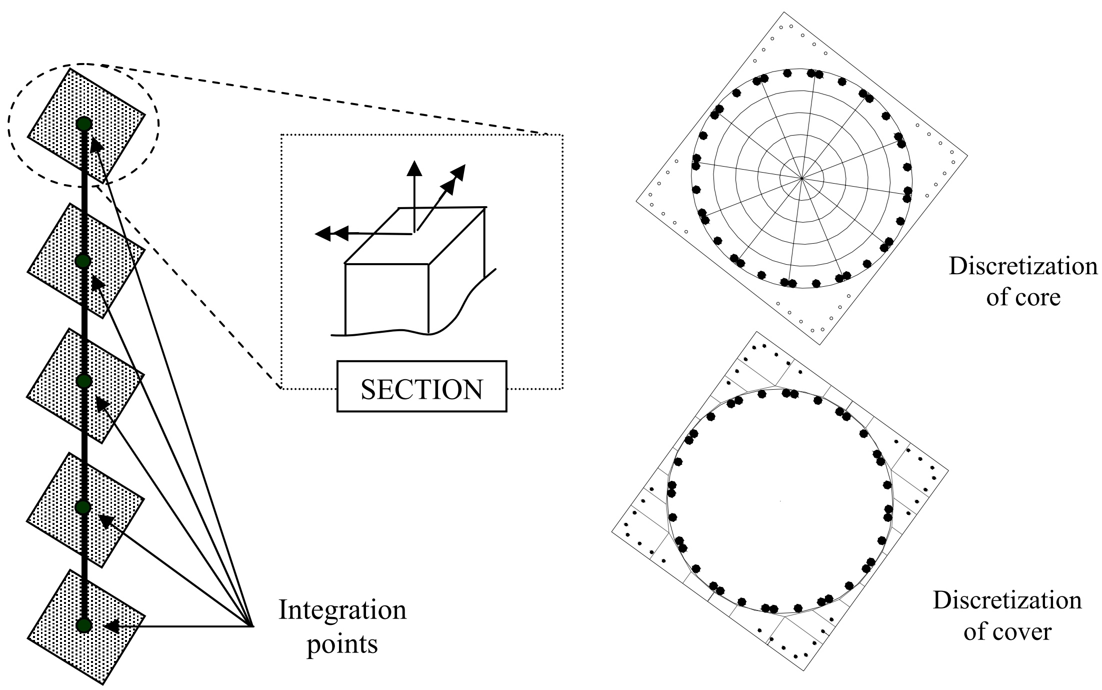

Fig. 2.9 Element and sectional discretization of force-based nonlinear beam-columns utilized to model piers of I-880 viaduct

Since the shear strength of the column sections are large enough to preclude shear yielding, only the elastic contribution to shear deformations are considered. Similarly, only the elastic component of torsional deformations is included in the beam-column model. Shear and torsional properties are aggregrated into the section as linear elastic constants. Relevant properties of the columns in each of the eleven bents of the three-frame model are given in Table 2.2. The ID refers to the north (N) or south (S) side of the bent, since the viaduct comprising the three frames is approximately oriented in the east-west direction.

Table 2.2 Column properties

Frame	Bent	ID	Height		Cross-Sectional Area		Moment of Inertia		Longitudinal Reinforcement Ratio	Axial Dead Load	
		N/S	m	ft	m^2	ft^2	I_y (m^4)	I_z (m^4)	%	kN	kips
3	10	N	18.20	58.71	6.32	68.00	5708	4718	0.92	10362	2313
		S	17.63	56.88	6.32	68.00	5708	4718	0.83	10362	2313
	11	N	17.66	56.98	6.32	68.00	5708	4718	1.01	9816	2191
		S	17.36	55.99	6.32	68.00	5708	4718	1.10	9816	2191
	12	N	18.14	58.51	6.32	68.00	5708	4718	1.29	9972	2226
		S	17.27	55.71	6.32	68.00	5708	4718	1.38	9972	2226
	13	N	17.64	56.89	6.32	68.00	5708	4718	1.10	9560	2134
		S	17.22	55.56	6.32	68.00	5708	4718	1.10	9560	2134
4	14	N	17.24	55.61	6.32	68.00	5708	4718	1.10	9493	2119
		S	16.84	54.33	6.32	68.00	5708	4718	1.10	9493	2119
	15	N	16.54	53.37	6.32	68.00	5708	4718	0.83	9498	2120
		S	16.51	53.26	6.32	68.00	5708	4718	0.83	9498	2120
	16	N	15.99	51.58	6.32	68.00	5708	4718	0.83	9587	2140
		S	15.81	51.00	6.32	68.00	5708	4718	0.83	9587	2140
	17	N	15.05	48.54	6.32	68.00	5708	4718	0.92	9628	2149
		S	14.85	47.90	6.32	68.00	5708	4718	0.92	9628	2149
5	18	N	13.70	44.20	4.88	52.50	1915	1522	1.01	9188	2051
		S	13.48	43.49	4.88	52.50	1915	1522	1.01	9188	2051
	19	N	12.56	40.51	4.88	52.50	1915	1522	1.01	8543	1907
		S	12.25	39.52	4.88	52.50	1915	1522	1.01	8543	1907
	20	N	10.96	35.34	4.88	52.50	1915	1522	1.01	7992	1784
		S	10.76	34.72	4.88	52.50	1915	1522	0.83	7992	1784

Beams. Three-dimensional beam elements were used to model both the bent-cap and the longitudinal box girders making up the deck and roadway of the bridge. A typical section of the longitudinal box girder was shown previously in Figure 2.3. Preliminary calculations of the respective strengths of the girder, bent caps, and bent piers indicated that yielding would be limited to critical sections of the bridge columns. Consequently, the bent caps and longitudinal box girders were modeled as elastic beam elements. The computed properties of the respective beams, based on the design drawings and assumed to be constant throughout the length of the viaduct model, are specified in Table 2.3.

Table 2.3 Beam properties

Property	Transverse Beam	Longitudinal Beam
E, MPa (ksi)	28360 (4110)	28361 (4110)
I, cm^4 (in^4)	2.18e8 (5.22e6)	7.49e8 (1.80e7)
A, cm^2 (in^2)	66450 (10300)	122200 (18940)
G, MPa (ksi)	11390 (1650)	11390 (1650)
J, cm^4 (in^4)	2.08e7 (5.0e5)	1.46e7 (3.5e5)

2.2.3 Soil-Structure Interaction Modeling

Modeling of soil-structure interaction was accomplished in OpenSees using *zeroLength* elements. These elements were given elastic properties to represent the stiffness of all six degrees of freedom provided by the soil-foundation system. No coupling between the degrees of freedom was considered.

The foundation system consisting of the pile group and surrounding soil was modeled using a separate 3D finite element model. For each of the eleven bents that comprise the three-frame model, equivalent spring constants for the simplified soil-foundation system were obtained from an analysis of a full 3D foundation model, using linear elastic material properties for both the soil and the concrete piles. Figure 2.10 shows the finite element mesh for this model. The model is made of solid 20 node quadratic brick elements for the soil and pile group cap, while elastic (Bernoulli) beam elements are used for piles. The model has approximately 1300 solid finite elements and 127 linear elastic beam elements. The boundaries on all five faces (four vertical and the base) were assumed to be fully restrained. Loading was separated into two stages: in the first stage, self weight was applied, followed by a static pushover analysis of the system. The elastic material properties used for the soil material were as follows: Young's modulus E = 11000 kPa; Poisson's ratio = 0.45 and unit weight of soil was assumed to be 13.7 kN/m^3. This mixing of solid and structural frame element exhibits two potential problems. The displacement interpolation function for beam elements (l'Hermite polynomials) and solid elements (quadratic polynomials) are incompatible. This might result in interpenetration (numerically) of pile material into the soil material. Additionally, the solid soil elements occupy volume that would be taken by the beam element (concrete pile). However, the model is simple enough and when considered in conjunction with the elastic assumption for soil, provides a good balance between sophistication and simplicity.

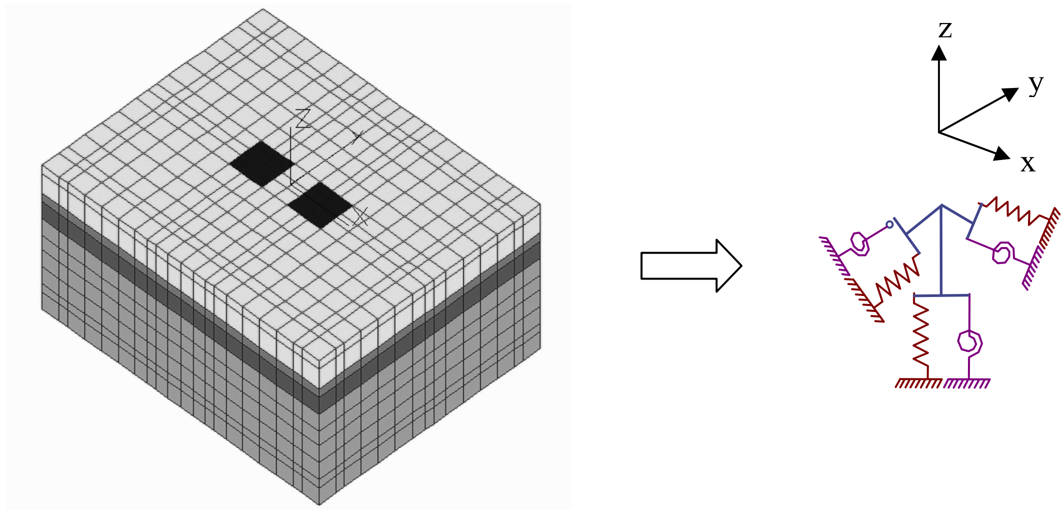

Fig. 2.10 Finite element model of typical pile group with surrounding soil and resulting equivalent translational and rotational soil springs

One feature that was excluded is radiation damping, which is clearly an important issue that can influence foundation-soil-structure interaction. Since radiation damping is a result of the stiffness differences between the piles (including pile cap) and the surrounding soil, it manifests primarily at higher frequencies and low soil damping. If gaps open between the foundation and soil, there can be no radiation damping. However, given the uncertainties in modeling the overall soil-foundation behavior and the fact that frequency-independent dashpots generally de-amplify the structural system response, it is not uncommon to neglect radiation damping altogether. Thus, based on findings from other research and the fact that the bridge pier yields well before the soil deformations become significant, the effects of radiation damping are not considered.

2.2.4 Modeling of Expansion Joints

Discrete zero-length spring elements are used to model the shear keys, restrainers, and bearing pads located at expansion joints. The connection elements at expansion joints are collectively referred to as “hinges.” The connection between frames 3 and 4 is known as hinge 13 and the connection between frames 4 and 5 is hinge 17. Cross sections of hinges 13 and 17 are shown in

Figures 2.11 and 2.12, respectively. Zero-length elements are defined by specifying two nodes at identical locations. The element behavior is defined by force-deformation properties in each desired degree-of-freedom.

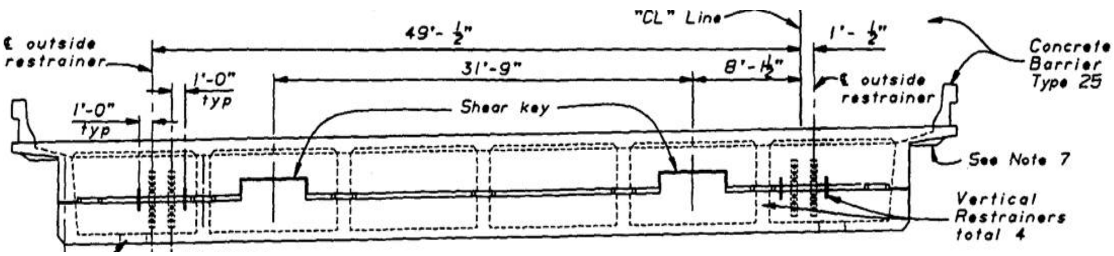

Figure 2.11 Hinge 13 cross section

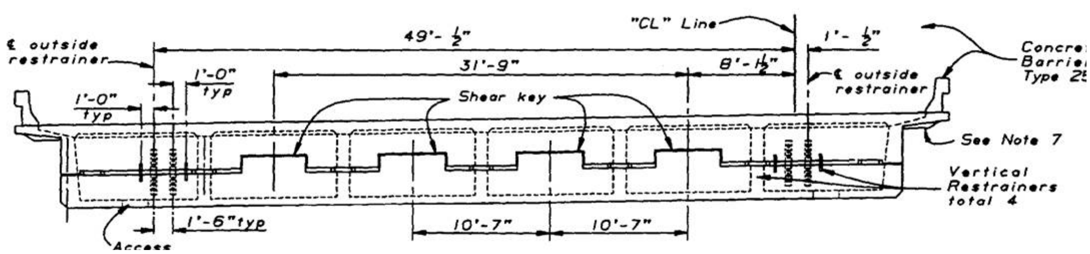

Figure 2.12 Hinge 17 cross section

Longitudinal restrainers and frame-to-frame interaction. Longitudinal restrainers and frame-to-frame impact represent the actions in the longitudinal direction of the bridge. Longitudinal restrainers at each expansion joint prevent longitudinal separation between adjacent frames. Longitudinal restrainers, whose details are shown in Figure 2.13, have movement ratings of 216 mm (8.5 in.) and 178 mm (7 in.) for hinges 13 and 17, respectively, that engage after longitudinal extension corresponding to the above values. The behavior of the restrainers was modeled by aggregating two materials, an elastic-perfectly-plastic gap material and an elastic material. The force-displacement relationship for the aggregated material is also shown in Figure 2.13. The axial stiffness of the restrainers (k_{LR}) is calculated from *EA/L*, where *E* is Young's modulus (given as 69,000 MPa), *A* is the cross-sectional area of the restrainer units, and *L* is the restrainer length.

Frame-to-frame interaction at each expansion joint is modeled using an elastic-perfectly-plastic material with material gaps of 57 mm (2.25 in.) and 44 mm (1.75 in.) for expansion joints 13 and 17, respectively. The actual gap between the frames varies seasonally due to the effects of weather conditions on the structure. For this model the gap was taken to be the smallest of the seasonal numbers given in the as-built drawings. The stiffness in the compression direction (k_F) represents the longitudinal stiffness of the adjoining frame. The opening of the longitudinal gap in the positive (or tension) direction of the model results in activation of the restrainers, whereas gap closure in the negative (or compression) direction results in impact. A linear elastic spring, whose stiffness is equal to the longitudinal stiffness of the adjoining frame, is activated upon impact. Such a representation is not truly an impact model but an approximate representation of forces transmitted upon gap closure. Separate studies indicate that increasing the stiffness of the spring by a factor of 10 or more to simulate near-infinite stiffness produced negligible effect on the transverse demand in the bent. Since introducing very high stiffness values at localized sections can lead to numerical instability when nonlinear elements in the system begin to yield, the compression stiffness was set equal to the longitudinal stiffness of the adjoining frame. Modeling of impact was beyond the scope of this study. The force-deformation model shown in Figure 2.13 depicts the complete behavior in the longitudinal direction of the viaduct.

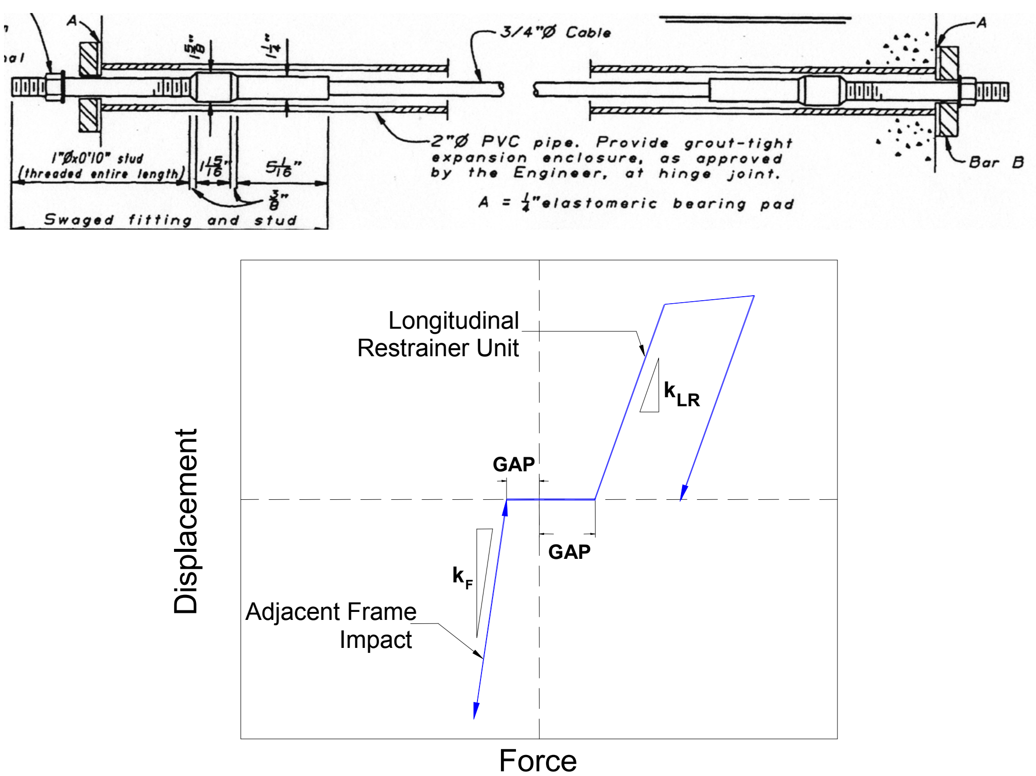

Fig. 2.13 Longitudinal restrainer unit and modeling of hinges in longitudinal direction

Modeling vertical movement at expansion joints. The vertical restraining system is made up of a total of 8–19 mm diameter cables with a specified elastic modulus of 69,000 MPa. Furthermore it is assumed that the vertical restrainers engage immediately if any vertical separation occurs between adjacent frames. Figure 2.14 shows the vertical restrainer detail provided in the as-built drawings. The restrainers are modeled using an elastic-perfectly-plastic material (with a capacity in tension of 1215 MPa) without a gap and that is aggregated with an elastic material for post-yield stiffness.

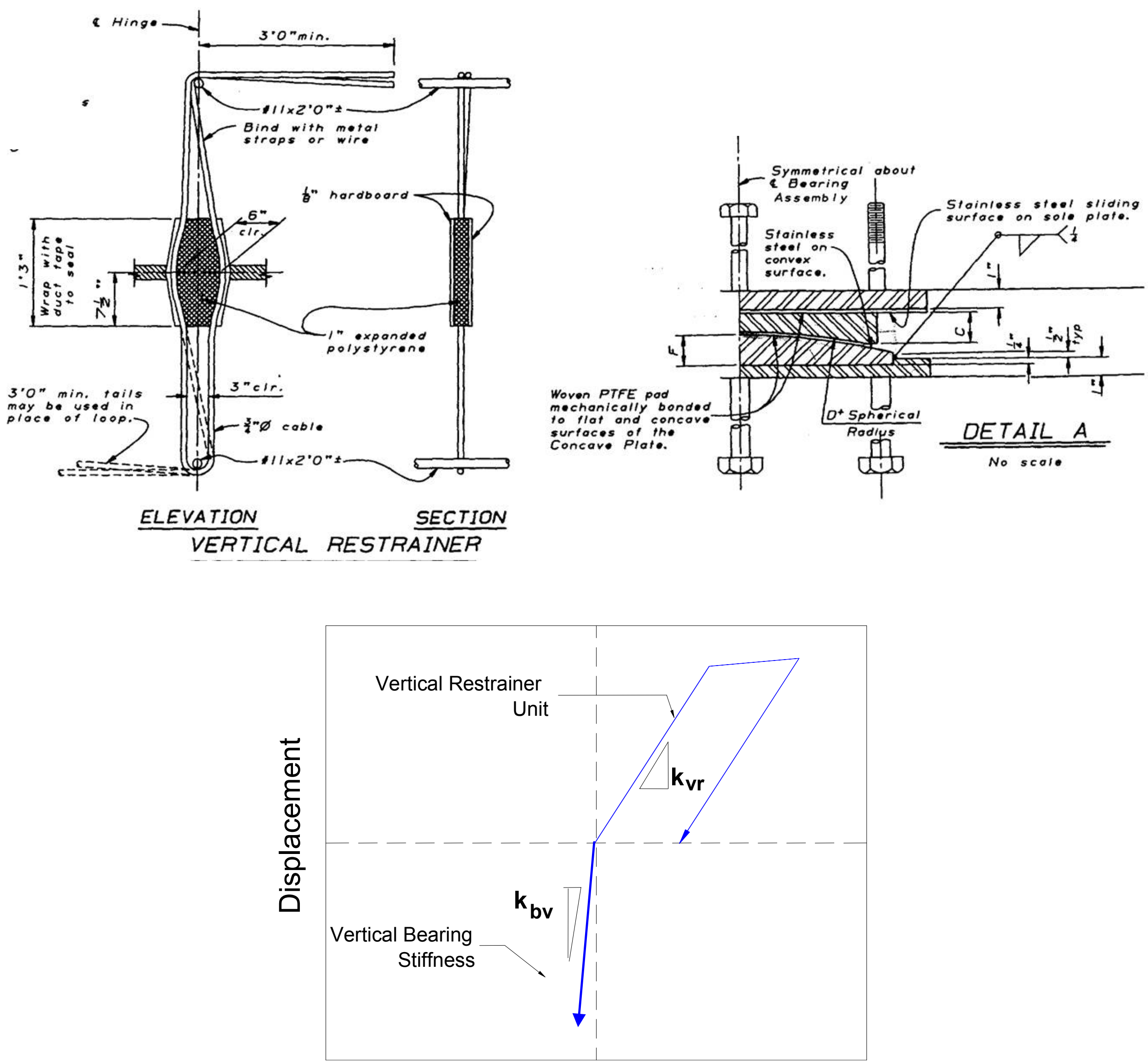

Fig. 2.14 Vertical restrainer unit and modeling of hinges in vertical direction

Both hinge 13 and hinge 17 have seven PTFE spherical bearing plates. These plates consist of a PTFE surfaced concave plate and mating stainless steel convex plate which accommodate rotation through sliding of the curved surfaces. The diameter of the concave contact surface is 24 cm (9.5 in.) and the height of the bearing is approximately 5 cm (2.5 in.). The bearing detail from the as-built drawings is shown in Figure 2.14. The plates are modeled as having an elastic stiffness of *GA/h* where *G* is the shear modulus for steel, *A* is the cross-sectional area of the contact surface, and *h* is the height of the bearing plate. This friction force is calculated using a coefficient of friction of 0.055 in accordance with Caltrans Bridge Design Specifications (2000) and based on bearing pressure. The bearing plates provide a static friction force that resists sliding, but because the force on the bearing plate due to dynamic loading is significantly greater than the bearing plate friction force, sliding occurs almost immediately upon loading. Therefore, the bearing plates are modeled using an elastic-perfectly-plastic material with a capacity of 6100 kN (1370 kips) in the longitudinal and transverse directions and with an arbitrarily high capacity to preclude yielding.

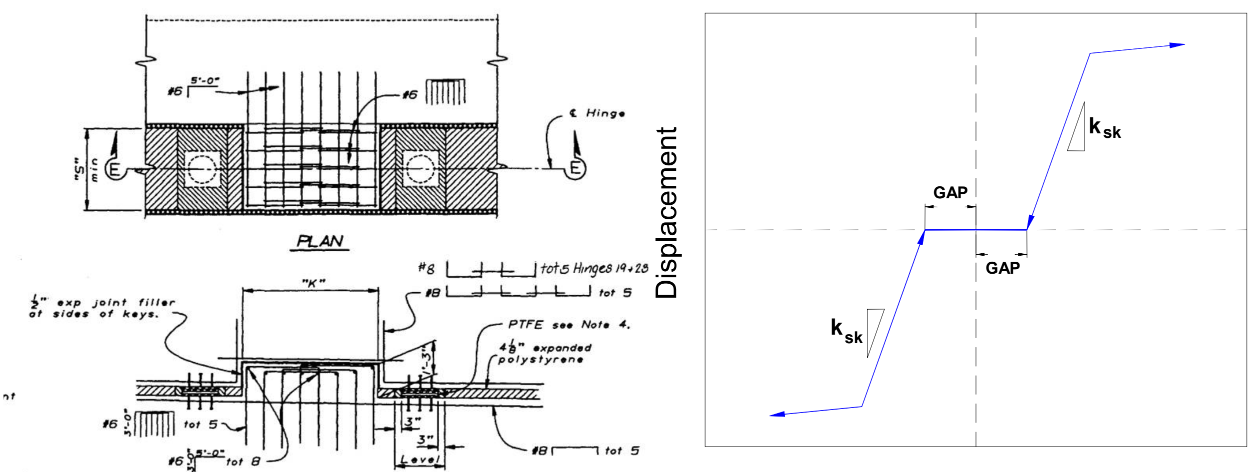

Fig. 2.15 Shear key detail and modeling

Shear keys. To restrain relative movement between adjacent frames in the transverse direction, hinges 13 and 17 have two and four shear keys, respectively (Figs. 2.11–2.12). Each rectangular shear key consists of concrete cover over an arrangement of 40 #6 bars and has a calculated shear capacity of approximately 7300 kN (1650 kips). The shear key detail from the as-built drawings is shown in Figure 2.15. The shear keys are modeled using elastic-perfectly-plastic gap elements with a shear stiffness of *GA/h,* where *G* is the shear modulus of the reinforcing steel, *A* is the total area of the steel in the keys for each hinge, and *h* is the height of the key (380 mm). The initial gap before the shear key is engaged is 12.5 mm (0.5 in.). This behavior is also shown in Figure 2.15.

2.2.5 Assembled Three-Frame Model

The assembly of elements comprising the expansion joint at each frame-to-frame connection is displayed in Figure 2.16. The diagram identifies four pairs of nodes denoted by C1–C4 and R1–R4. These represent restrained (R) and constrained (C) nodes of the zero-length elements. Figure 2.16 shows the complete three-frame model composed of the following: equivalent soil-foundation springs at the base of every bent pier; nonlinear columns, and elastic beams, comprising the eleven bents in the model; longitudinal beams representing the box girder and bridge deck; and the connection elements at the expansion joints.

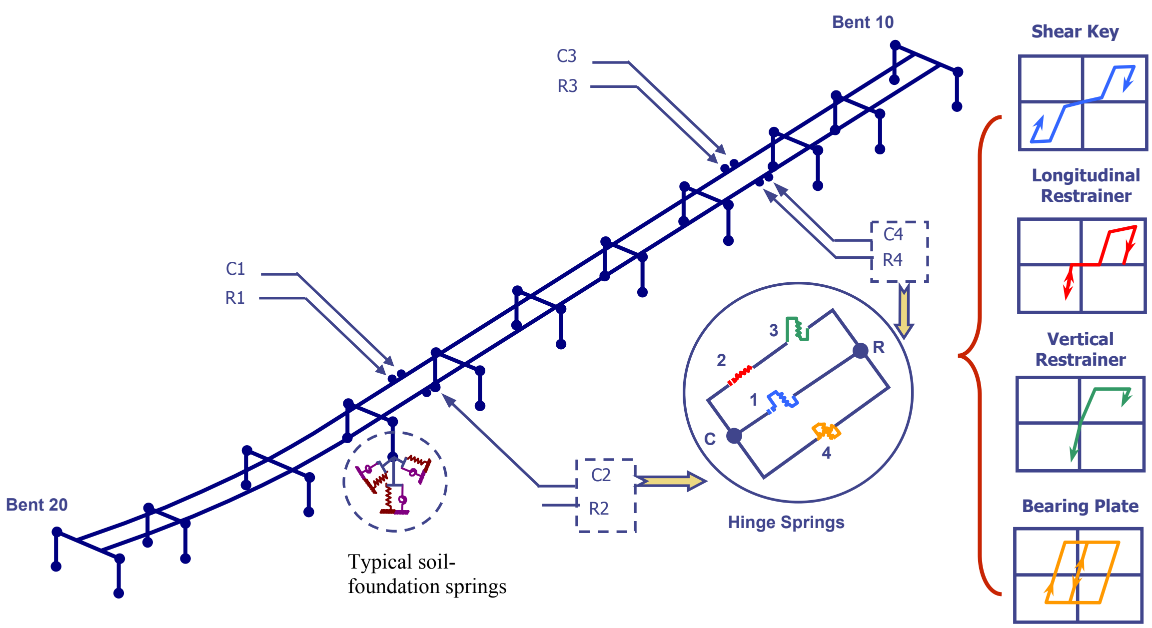

Fig. 2.16 Three-frame model of a section of I-880 viaduct used in simulation studies

The simulation model will form the basis of the *EDP* analysis to be presented in Chapter 4. In developing the above model, due attention was given to the influence of the adjoining frames. Separate analyses utilizing equivalent springs to represent the translational stiffness of the adjoining frames indicate that the restraining action and interaction of these frames with the proposed simulation model is negligible.

2.3 ESTABLISHING FIRST MODE PERIOD OF MODEL

The intensity measure (*IM*) selected for the study is the 5% damped elastic spectral acceleration at the characteristic period of the structure (see Section 3.1.2). In order to establish the characteristic period, the frequency of the structure was established at different lateral displacement demand levels for several simulation models. Since the structure retains its initial elastic state only for a very short time and at very small deformations, it was decided that a more rational choice of the period of the model needs to be established for purposes of scaling the ground motions. Several models of the I-880 structure were considered in determining the so-called "characteristic" period: models of a typical bent, a typical frame (comprising four bents), and the multiframe model with fixed base conditions and with equivalent springs representing the soil-foundation system. The variation of the fundamental period for different levels of lateral drift is shown in Figure 2.17. The "characteristic" period was selected as the mean fundamental period at a drift ratio of approximately 0.5% as shown in the figure.

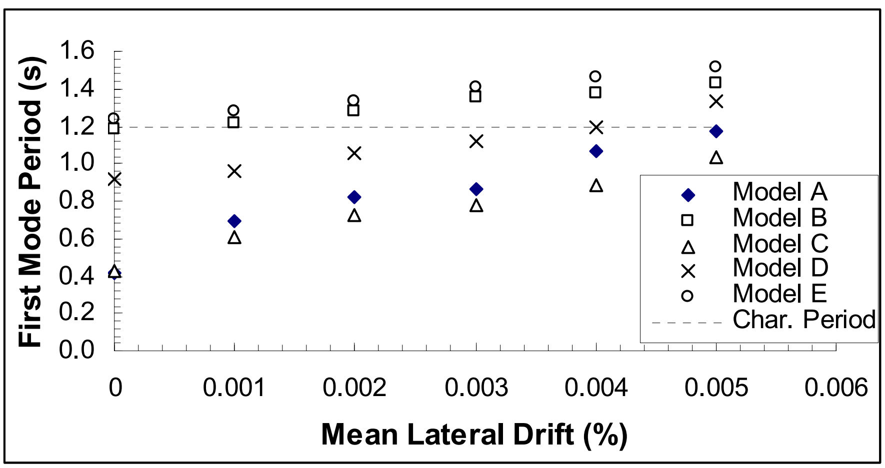

Fig. 2.17 Variation of fundamental period with increasing lateral deformation in pre-yield range of model response (Model A: Typical bent with fixed base; Model B: Typical bent with soil-foundation springs; Model C: Four-bent frame with fixed base; Model D: Four-bent frame with soil-foundation springs; Model E: Three-frame model with soil-foundation springs)

3 Hazard Analysis and *EDP* Simulation

Sashi Kunnath
University of California, Davis
Paul Somerville
URS Corporation, Pasadena, CA

In this chapter, the first two steps in the PEER PBEE framework are carried out. These tasks may be considered to be the essential steps in the methodology because the remainder of the evaluation process depends entirely on the *EDP*s and associated *IM*s. Beginning with the identification of the seismicity and geology at the site, a probabilistic description of the hazard is derived. The selection of the ground motions that collectively represent the site hazard is followed by a series of time-history analyses that yield a probabilistic representation of the expected seismic demands.

3.1 CHARACTERIZATION OF HAZARD

The preliminary step in the performance assessment of the I-880 structure is the characterization of the seismic hazard at the site. In the context of the PEER methodology, this entails the development of a site hazard curve that expresses the mean annual frequency (annual probability) as a function of the intensity measure (*IM*). The selection and scaling of ground motions also play an important role in the evaluation process and will be described in the following sections.

3.1.1 Uniform Hazard Spectra

Uniform hazard spectra for S_D (soil) site conditions were derived by Somerville and Collins (2002) for the bridge site corresponding to three hazard levels: events with a 50% probability of being exceeded in 50 years; events with a 10% probability of being exceeded in 50 years; and events with a 2% probability of being exceeded in 50 years. The ground motion model of

Abrahamson and Silva (1997) was used in generating the spectra. The spectra contain rupture directivity effects which were represented in the probabilistic hazard analysis using the empirical model proposed by Somerville et al. (1997). Separate response spectra are provided for the strike-normal (SN) and strike-parallel components (SP). The site hazard spectra for the three different hazard levels that were investigated are shown in Figure 3.1.

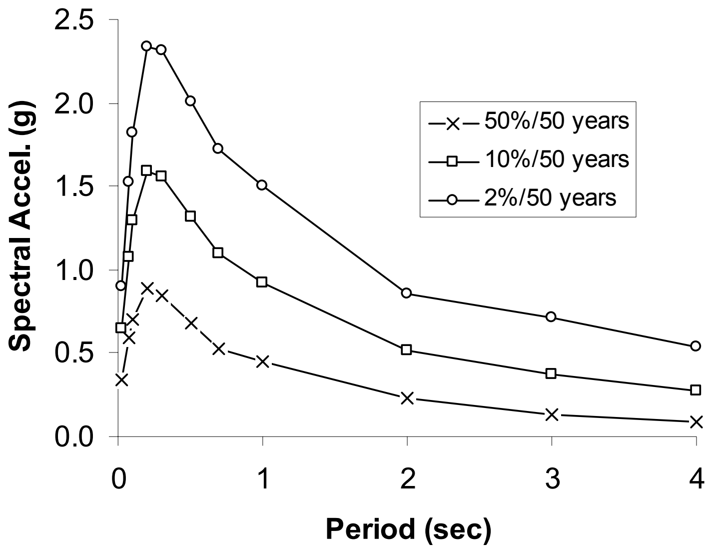

Fig. 3.1 Uniform hazard spectra for strike-normal component and S_D site condition

3.1.2 Intensity Measure *(IM)*

In the present study, *IM* will be measured in terms of the 5% damped elastic spectral acceleration (S_a) magnitude at the fundamental period of the structure. Other measures of seismic intensity may be considered but the objective here is to illustrate the application of the methodology and not to propose an intensity measure for general performance-based evaluation. Therefore, a separate evaluation comparing the effectiveness of different *IM*s or the appropriateness of the *IM* selection for this study was not carried out. Nonetheless, studies by Shome and Cornell (1996) suggest that median response estimates within a given confidence band are achieved with smaller number of records when scaling ground motions to the same spectral acceleration at the fundamental frequency of the structure. Since only ten records are being used in the *EDP* simulations for each hazard level, one of the objectives of the *IM* selection was to minimize the dispersion in the response. Finally, while it would be desirable to treat the selection of ground motions as a probabilistic phenomenon (given the uncertainty in ground motion characteristics from site to site and event to event), the selected records in this study have been assumed to have equal probabilities of occurrence.

3.1.3 Selection, Scaling, and Transformation of Ground Motions

The deaggregation of the hazard at a period of 1 sec is given in Table 3.1. At all three hazard levels, the hazard is dominated by earthquakes on the Hayward fault, which is located about 7 km east of the site. The Hayward fault is a strike-slip fault that has the potential to generate earthquakes having magnitudes as large as 7.0.

Table 3.1 Deaggregation of hazard spectra (5% damping)

Hazard Level	S_a at 1.0 sec	M mode	R (km)
50% in 50 years	0.291	6.6	7
10% in 50 years	0.580	6.8	7
2% in 50 years	0.931	7.0	7

Earthquakes were selected to satisfy to the extent possible the magnitude and distance combinations listed in Table 3.1 for strike-slip earthquakes. In general, it was not easy to satisfy these requirements. For example, though it was not possible to satisfy the distance requirement exactly, all of the selected recordings are within about 10 km of the fault. The selected time histories for all three hazard levels are listed in Table 3.2. The same set of time histories is used to generate both the 10%/50 and 2%/50 sets of ground motions. This is justified in part by the fact that the magnitude-distance combinations that dominate the hazard in each case are the same. However, this ignores the fact that the 2%-in-50-years time histories should be drawn from larger ground motion recordings than the 10%-in-50-years time histories. The selected ground motion time histories were all recorded sufficiently close to the fault to contain rupture directivity effects. Additional information on the selection of the ground motion histories is reported in a paper prepared for the testbed project by Somerville and Collins (2002).

The selected time histories have to be scaled in a manner that is consistent with the choice of the intensity measure. As indicated previously, the *IM* selected for this study is the 5%

damped elastic spectral acceleration magnitude at the fundamental period of the structure. This period was identified as 1.20 sec from an eigenvalue analysis of the three-frame simulation model outlined in Chapter 2. Using the strike-normal (SN) response spectra (Fig. 3.1), a scale factor is determined for each SN record in each of three hazard levels. This scale factor is applied to all three components of the earthquake recording to preserve the relative scaling between the components. Once the scaling process is complete, the records must be transformed into the longitudinal and parallel directions of the bridge.

Table 3.2 Selected ground motions representing seismic hazard at site

Hazard Level	Earthquake	Date	Magnitude	Station	Distance (km)
50% in 50 years	Coyote Lake	June 8, 1979	5.7	Coyote Lake Dam Abutment	4.0
				Gilroy #6	1.2
	Parkfield	June 27, 1966	6.0	Temblor	4.4
				Array # 5	3.7
				Array # 8	8.0
	Livermore	Jan. 27, 1980	5.5	Fagundes Ranch	4.1
				Morgan Territory Park	8.1
	Morgan Hill	April 24, 1984	6.2	Coyote Lake Abutment	0.1
				Anderson Dam Downstream	4.5
				Halls Valley	2.5
10% in 50 years AND 2% in 50 years	Loma Prieta	Oct.17, 1989	7.0	Los Gatos Presentation Ctr.	3.5
				Saratoga Aloha Ave.	8.3
				Corralitos	3.4
				Gavilan College	9.5
				Gilroy Historic	
				Lexington Dam Abutment	6.3
	Kobe, Japan	Jan. 17, 1995	6.9	Kobe JMA	0.5
	Tottori, Japan	Oct. 6, 2000	6.6	Kofu	10.0
				Hino	1.0
	Erzincan, Turkey	March 13, 1992	6.7	Erzincan	1.8

The recorded time histories represent free-field motions in the strike-normal (SN) and strike-parallel (SP) directions of the Hayward fault. In the vicinity of the I-880 bridge, the Hayward fault has a strike of N34^{o}W (Fig. 3.2a). This fixes the orientation of the two horizontal components for input into the simulation model. The bridge is curved, so there is no single rotation of the time histories that would yield transverse and longitudinal components that apply to the whole length of the bridge. However, a reasonable approximation of the orientation of the longitudinal axis of the three-frame model was determined to be S76°W resulting in transformation angle of $\theta = 70°$ (Fig. 3.2b). Therefore, the required transformations to generate ground motions in the longitudinal and transverse directions of the bridge are

$$Longitudinal = SP\cos\theta + SN\sin\theta \tag{3.1}$$

$$Transverse = SP\sin\theta - SN\cos\theta \tag{3.2}$$

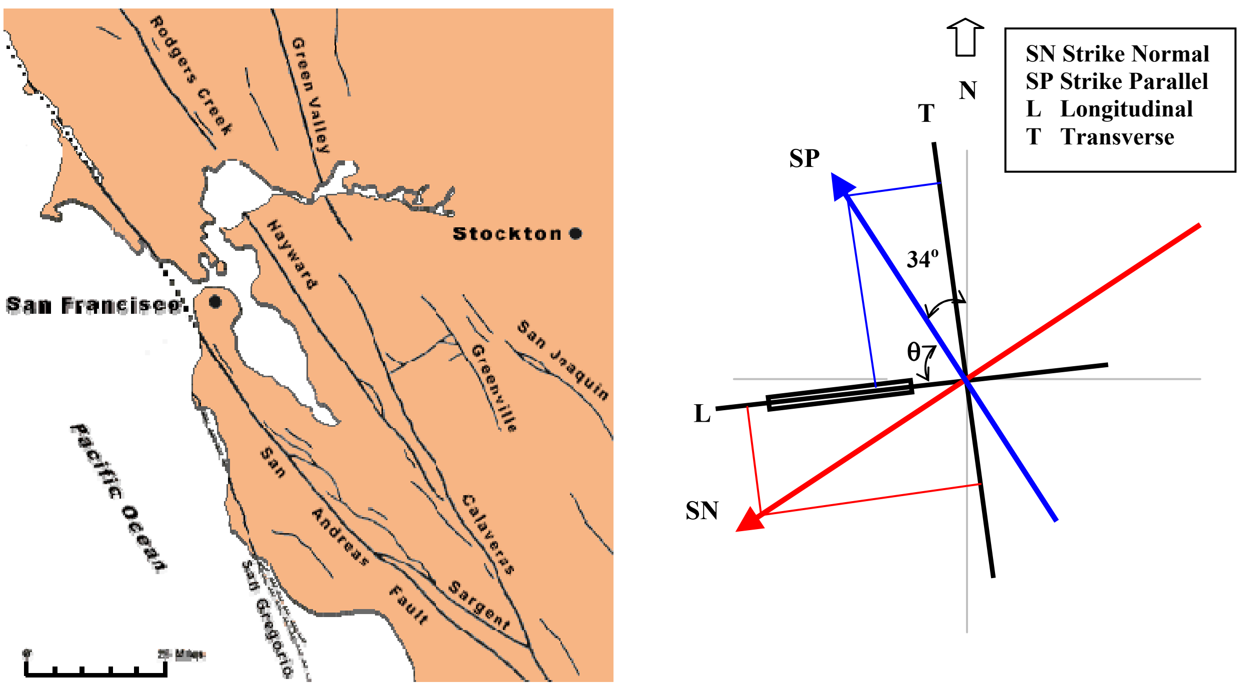

Fig. 3.2 Bay Area fault orientations and required transformation for I-880

The scheme outlined above was carried out for all 30 sets of recordings for three hazard levels. The outcome of the process is displayed in Figure 3.3 for a sample set of recordings corresponding to events with a 10% probability of being exceeded in 50 years (see Figs. A.1–A.2 for the remaining spectra plots). Shown in the figure are the spectra for the original records in all three orthogonal directions (transverse, longitudinal, and vertical) of the model followed by the spectra of the scaled and then transformed records. Note that only the spectra of the *scaled* strike-normal records match the hazard spectra at T = 1.2 sec. Transforming the records after scaling does not preserve the matching at the fundamental period. The consequence of this transformation is to increase the dispersion in the demands, an issue discussed later in this report.

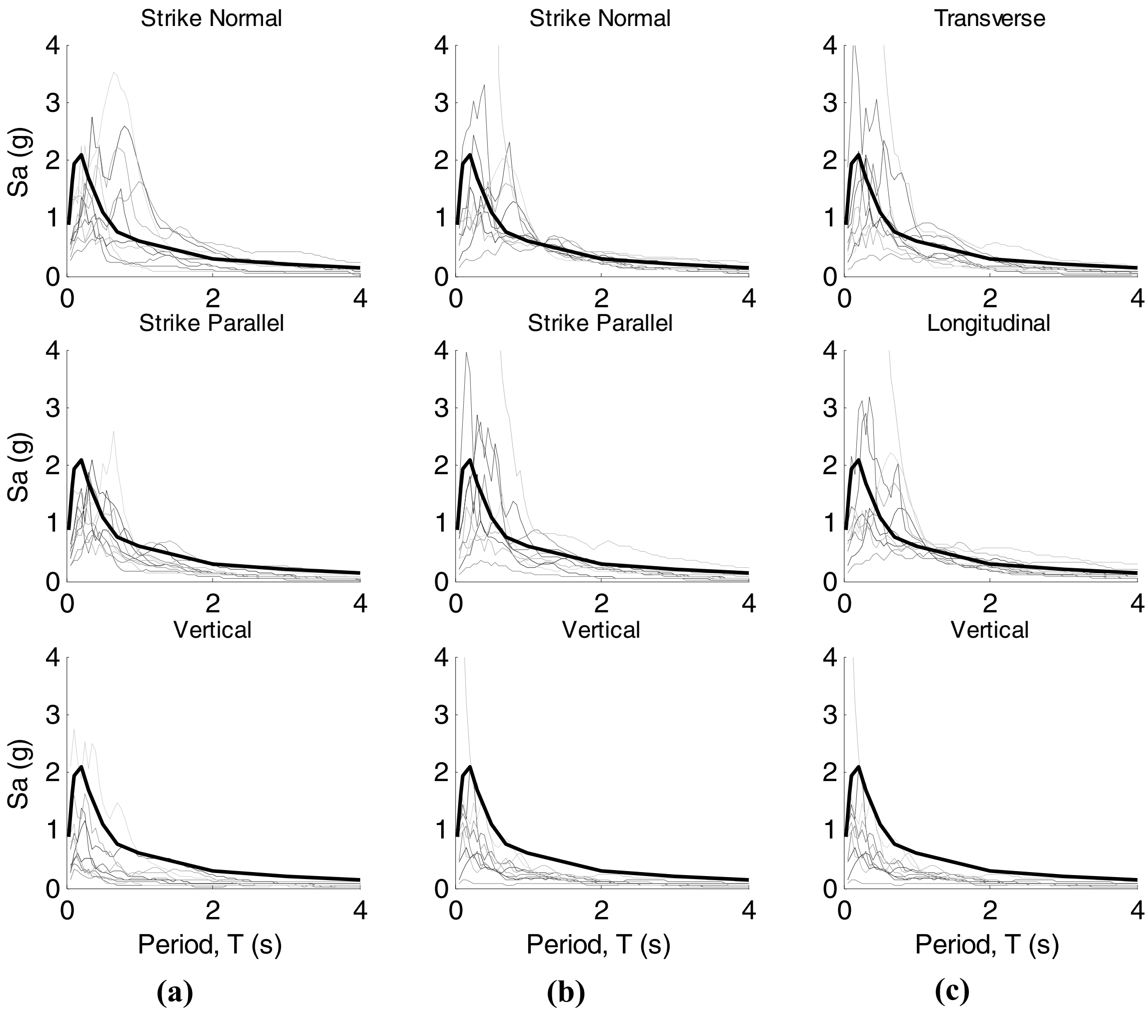

Fig. 3.3 Hazard spectra for 10% in 50 year earthquakes: (a) original, (b) scaled to T=1.2s, and (c) scaled and transformed ground motions

3.1.4 Hazard Curve

The performance of the I-880 viaduct, represented by the multiple frame model developed in Chapter 2, is being evaluated for three earthquake hazard levels. As already indicated, these hazard levels correspond to 50%, 10%, and 2% probability of being exceeded in 50 years. The mean return periods for each of these hazard levels are 72, 474, and 2475 years, respectively.

The seismic hazard curve is derived by plotting the return periods against the magnitude of the spectral accelerations at the characteristic structural period. Several studies have shown that for a relatively wide range of intensities, the seismic hazard curve can be approximated as a linear function on a log-log scale. In particular, Sewell, Toro, and McGuire (1991); Kennedy and Short (1994); and Cornell (1996) have proposed that the seismic hazard curve be approximated as

$$\lambda(IM) = k_0 (S_a)^{-k} \tag{3.3}$$

For the I-880 bridge site, it was determined that $k_0 = 0.0011$ and $k = 2.875$ (Fig. 3.4).

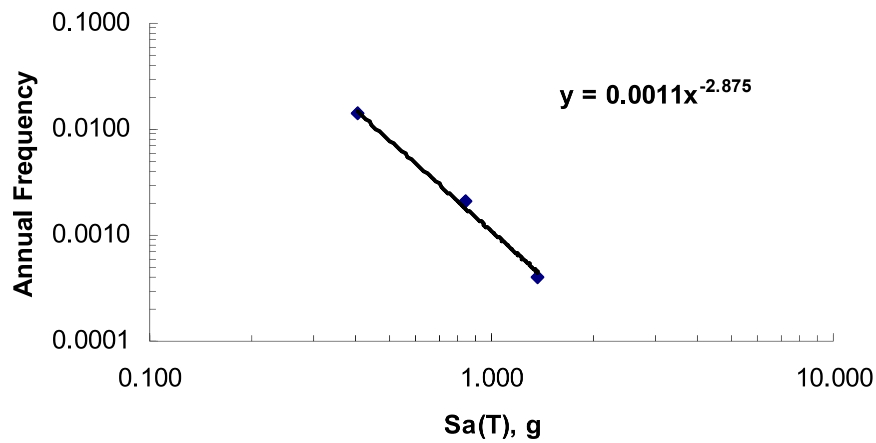

Fig. 3.4 Seismic hazard curve for I-880 bridge site

To utilize the hazard curve in the PEER evaluation methodology, it is necessary to find $\left[\frac{d\lambda(IM)}{dIM}\right]$, which is the slope of the best-fit line shown in Figure 3.4. Using the exponential form given by Equation 3.3 with $IM = S_a(T)$, the following expression is obtained:

$$d\lambda(IM) = \left[\frac{d\lambda(IM)}{dIM}\right] dIM = -kk_0 (IM)^{(-k-1)} dIM \tag{3.4}$$

This form of the slope of the hazard curve can be used in direct integration of the PEER framework equation described previously in Equation 1.5.

3.2 SIMULATION OF SEISMIC DEMAND (*EDP*s)

The simulation model developed for the three-frame section of the I-880 viaduct in Chapter 2 is subjected to each set of ten scaled and transformed earthquake recordings discussed in the previous section for each hazard level. The outcome of this phase of the evaluation generates the *EDP*s of interest for use in the performance assessment of the viaduct.

3.2.1 Primary *EDP* Used in Evaluation

Numerous *EDP*s at the structural level (displacements, rotations), foundation system (deformations in the soil-foundation springs), and hinges (forces and deformations in equivalent springs at expansion joints) can be recorded for each simulation. However, only those *EDP*s relevant to damage analysis and loss modeling can be utilized in the next step of the PEER performance-based framework. The choice of an *EDP* for this study was influenced by the damage measure available for the performance evaluation of the viaduct. As will be discussed in the next chapter, fragility functions have been developed by collaborative PEER researchers for several damage states as a function of the single-curvature drift of cantilever bridge columns. Hence, the primary *EDP* is the peak tangential drift of the individual columns. A typical bent and the corresponding tangential drift in each column is identified in Figure 3.5. The *EDP* is a measure of the larger relative lateral deformation from the inflection point to either the base or top of the column and is computed as follows:

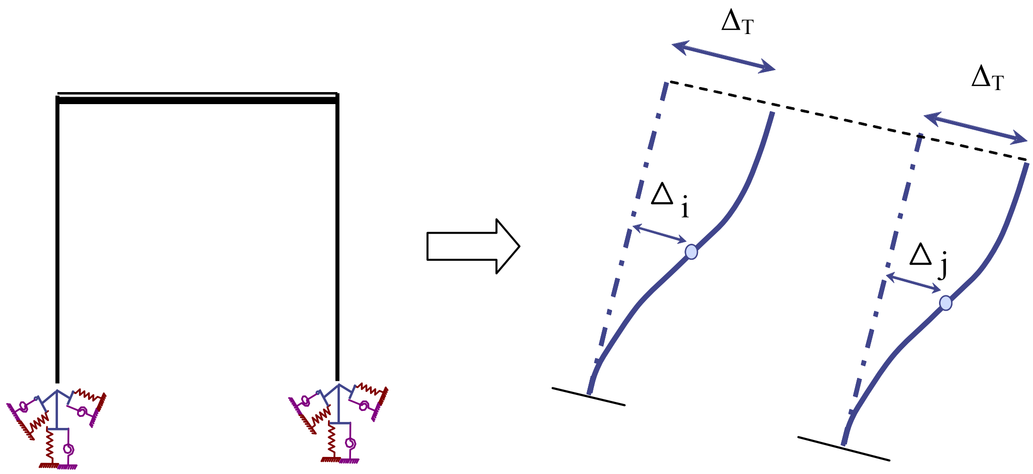

Fig. 3.5 Typical bent model and lateral deformed shape identifying deformation measures used in computation of tangential drift

$$Tangential\ drift)_{bent\ k} = {}_{max}\left|(\Delta_T - \Delta_i),(\Delta_T - \Delta_j),\Delta_i,\Delta_j\right| \tag{3.5}$$

The actual tangential drift was computed in the OpenSees simulations reported in this study; however, it is noted that the tangential drift for the particular case of two-column bents with a relatively rigid deck can be approximated as half the drift at the deck level, since the location of the inflection point will be close to the midheight of the columns in most cases.

3.2.2 Summary of Seismic Demands

All simulations were carried out using Newmark's implicit algorithm with $\gamma = 0.50$ and $\beta = 0.25$, which assumes average acceleration between two successive time steps and is unconditionally stable for any Δt, though it is essential to use time steps equal to or less than the interval of the earthquake input to ensure reliable results. Constant mass-proportional damping corresponding to a damping ratio of 5% in the first mode was used. The Newton-Raphson (NR) algorithm was specified for the iterative nonlinear analysis.

The OpenSees-computed response measures for the simulation model subjected to 30 ground motion records corresponding to three hazard levels were reviewed and summarized. The maximum tangential drift, as defined in Equation (3.5), was determined for each bent and these data are plotted in Figure 3.6. There are ten data points associated with each hazard level for each bent. Also shown in the figure is the mean and +/-σ (one standard deviation) of these demand parameters for each hazard level. It is seen that the dispersion in the demands increases with increased hazard levels and lower exceedance probabilities. Similarly, the variation in the demand from one bent to the next increases as the intensity of the ground motion increases. For example, in the case of the 50%/50 records, the mean maximum demand across all the bents is almost constant at approximately 0.35% with a standard deviation of about 0.2%. At a higher hazard level corresponding to 10%/50 and 2%/50 year events, the average demands vary considerably from one bent to the next. For example, the mean maximum demand on bent 3 is 0.34% and for bent 7 0.41% (a difference of about 20% with respect to the mean value for all bents) for the 50%/50 records; the demands on the same bents increase to 0.48% and 0.70%, respectively, (a difference of 38% with respect to the mean) for the 10%/50 year ground motions.

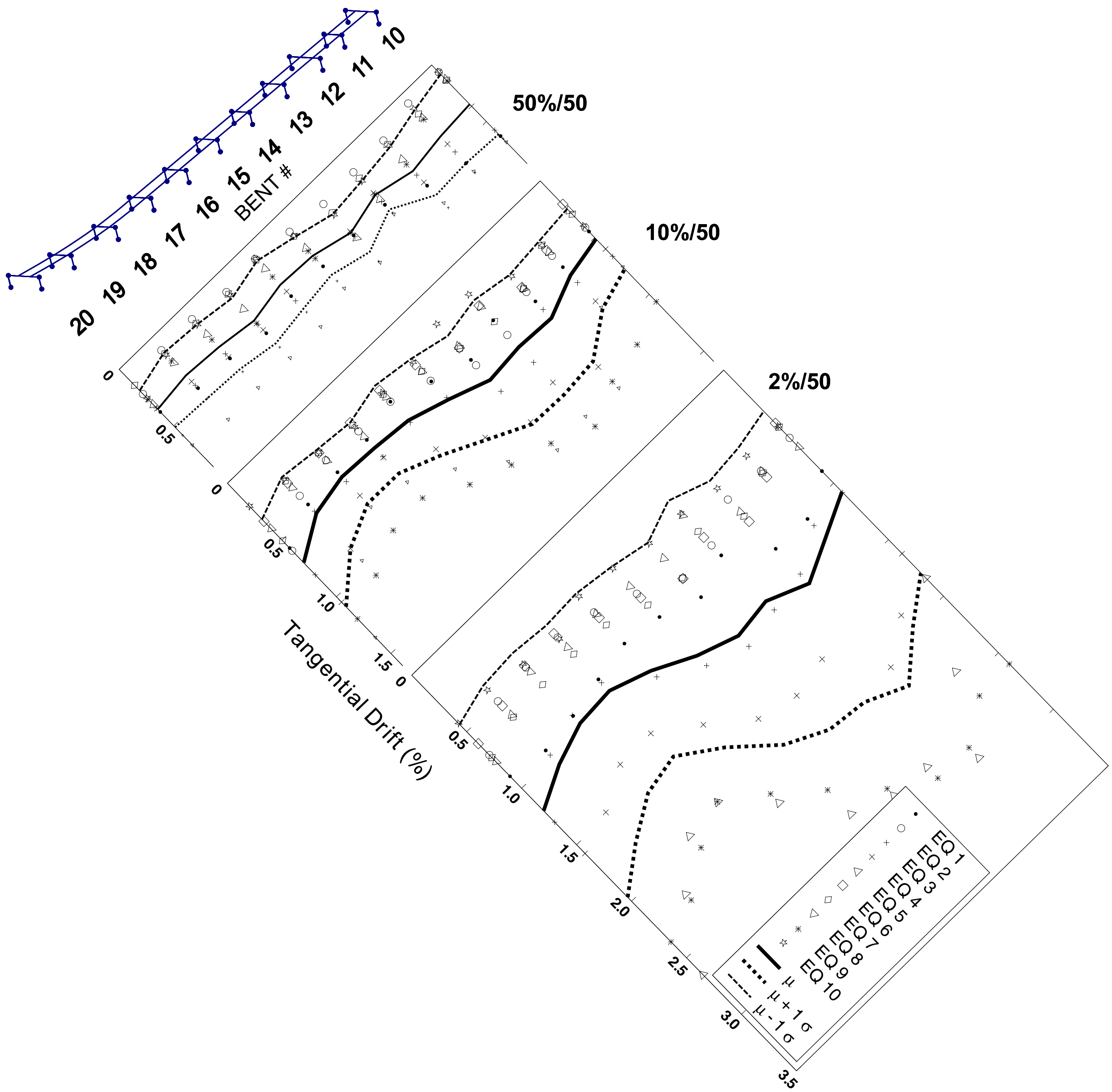

Fig. 3.6 Summary of maximum seismic demands for all three hazard levels

3.2.3 Probabilistic Demand Analysis

The distribution of *EDP*s conditioned on the intensity measure is assumed to have a lognormal distribution. Two statistical measures are required to describe the *EDP* distribution: a central tendency measure and a measure of variation. The central tendency is described by the geometric mean, which is the mean of the natural logarithms of the *EDP*s, represented by x_i, and is given by

$$\mu_{ln\,x} = \frac{1}{n}\sum_{i=1}^{n} ln\,x_i \tag{3.6}$$

where n is the number of observations. The geometric mean (referred to simply as *mean* hereon) assumes that a data set is normally distributed in log-space. The variation around the central tendency of a data set is the standard deviation of the natural logarithm of the *EDP*s, x_i, and is given by

$$\sigma_{\ln x} = \sqrt{\frac{1}{n-1}\sum_{i=1}^{n}\left(\ln x_i - \mu_{\ln x}\right)^2} \tag{3.7}$$

where $\mu_{ln\,x}$ is the best-fit line that represents the mean. In Figure 3.7, the computed *EDP*s defined by Equation (3.5) are plotted as a function of *IM*s. The scaled, nontransformed site-specific *IM*s are used in this step of the process, since they reflect the hazard at the site. As a result, the *IM* is the same for all *EDP*s for each intensity level. The best-fit line through the natural logarithm of the 30 values yields an expression, displayed in Figure 3.7, of the following form:

$$EDP = a\left(S_a\right)^b \tag{3.8}$$

where S_a, the spectral acceleration at the characteristic period of the simulation model, is the intensity measure used in the study.

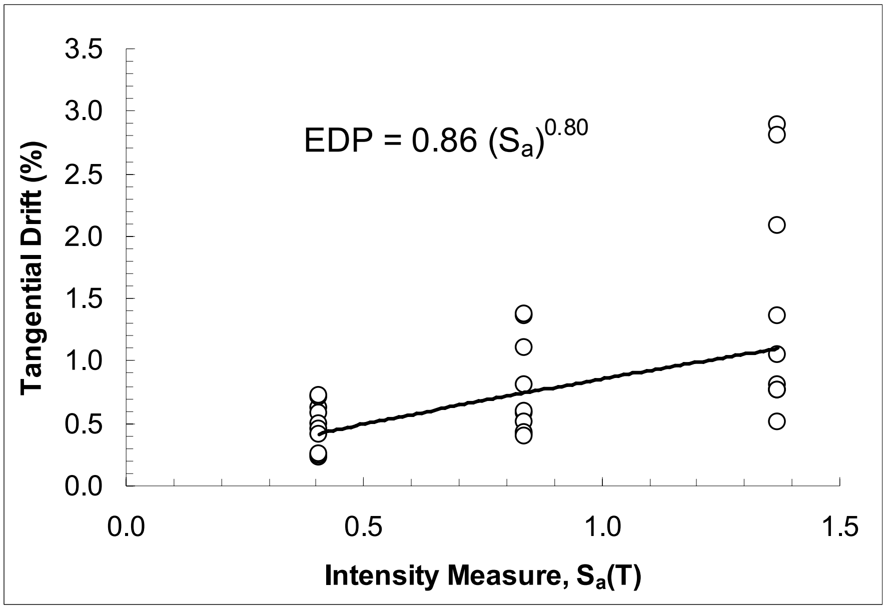

Fig. 3.7 Derived relationship between computed *EDP*s and *IM*

Since the probability of occurrence of the maximum tangential drift conditioned on the intensity measure is assumed to be lognormally distributed, the probability of exceeding a certain *EDP* limit can be evaluated as follows:

$$P(EDP > edp \mid IM = im) = 1 - \Phi\left(\frac{ln(EDP) - \mu_{ln\,EDP|IM}}{\sigma_{ln\,EDP|IM}}\right) \tag{3.9}$$

where Φ( ): standard normal distribution function

$\mu_{ln\,EDP|IM}$: mean of the natural log of the *EDP*s

$\sigma_{ln\,EDP|IM}$: standard deviation of the natural log of the *EDP*s

The results of the evaluation of Equation (3.9) are shown in Figure 3.8. The mean and standard deviation of the peak drifts at each hazard level were considered separately to generate independent probability distributions in each case.

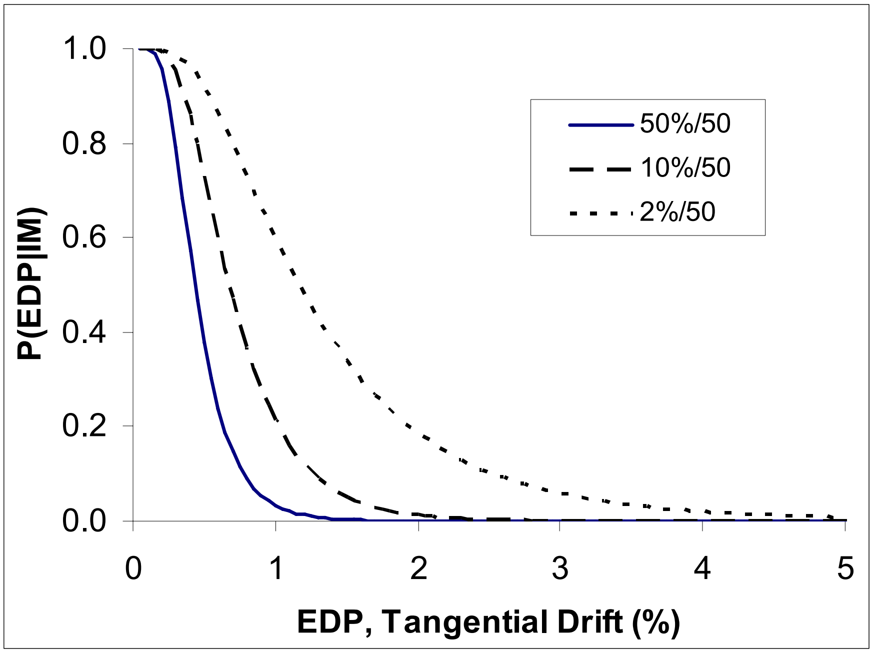

Fig. 3.8 Probability of exceeding demand for each hazard level

3.2.4 *EDP* Hazard Curve

Assuming that the *EDP* vs. *IM* relationship, based on the mean and dispersion measures represented in Figure 3.7, is valid across the entire hazard range of interest, an *EDP* hazard curve can be developed as follows:

$$\lambda(EDP > edp \mid IM) = \int_0^\infty [P(EDP > edp \mid IM = im)] \mid dv(IM) \mid \tag{3.10}$$

where $\lambda(EDP > edp \mid IM)$: mean annual frequency of *EDP* exceeding *edp*

$d\nu(IM)$: derivative of the mean hazard function or mean annual frequency of *IM* exceeding *im*

The first term on the right-hand side of Equation 3.10 was defined previously and $d\nu(IM) = \left[\frac{dv(IM)}{dIM}\right]dIM$ is the slope of the seismic hazard curve. The *EDP* hazard curve can be established through direct integration of Equation 3.10. If the intensity measure is expressed as indicated in Equation 3.3 and the *EDP-IM* relationship is assumed to have the form given in Equation 3.8, then it is possible to derive a closed-form expression for the solution of Equation 3.10, as follows:

$$\lambda(EDP) = k_0 \left[\left(\frac{EDP}{a} \right)^{\frac{1}{b}} \right]^{-k} \exp\left[\frac{1}{2} \frac{k^2}{b^2} \sigma_{\ln EDP|IM}{}^2 \right] \tag{3.11}$$

where k and k_0 were determined from the slope of the seismic hazard curve (Eq. 3.3), and a and b were determined from the slope of the best-fit line through the *EDP* data. The *EDP* hazard curve resulting from the solution of Equation 3.11 is displayed in Figure 3.9. Another important assumption in the derivation of the hazard curve is the fact that the dispersion implied in the curve-fitting of the *EDP* data (Fig. 3.7) is constant for all *IM*s. Generally, the dispersion increases for higher intensity measures as is evident in the data plotted in Figure 3.7.

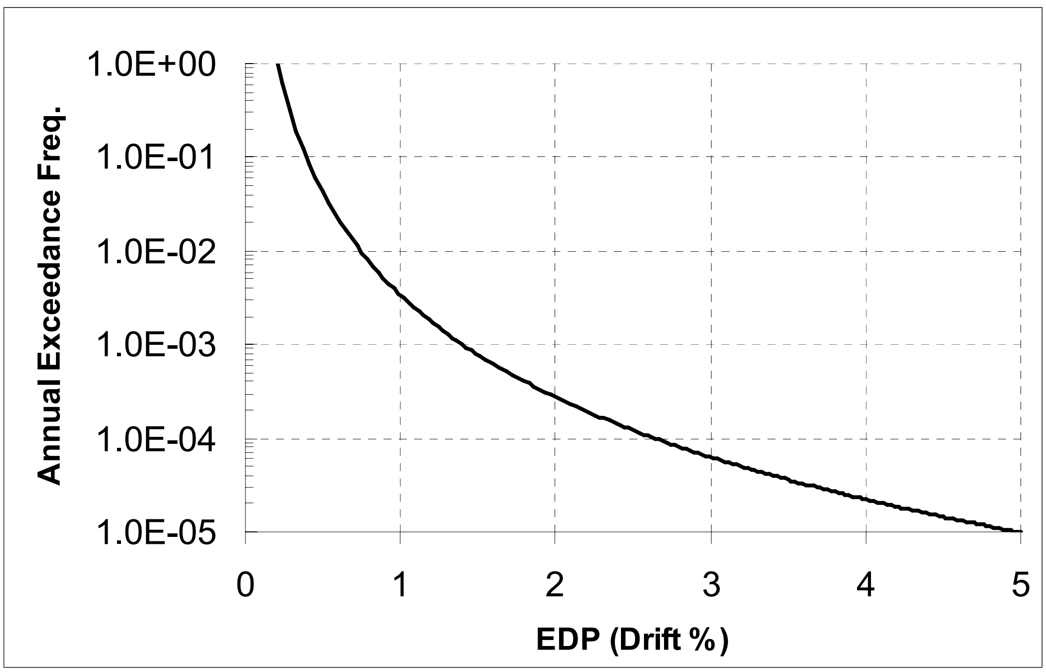

Fig. 3.9 ***EDP*** **hazard curve**

4 Damage Analysis

Mike Berry and Marc Eberhard
University of Washington, Seattle

4.1 INTRODUCTION

To implement performance-based earthquake engineering, it is necessary to relate engineering demand parameters (*EDP*s) with damage measures (*DM*s). Depending on the type of damage being considered and on the data available to calibrate damage models, the most appropriate *EDP*s could be relative displacements, rotations, or strains, and might account for the effects of cumulative deformation. For the purpose of this chapter, which focuses on reinforced concrete columns, the *EDP* is taken as the maximum column drift ratio, and the damage states considered are the onset of spalling of the concrete cover and the onset of buckling of the longitudinal bars. Spalling of the concrete cover is an important damage state (Fig. 4.1a) because it represents the first flexural damage state in which there may be a loss of function, and in which the cost to repair concrete spalling could be significant. The onset of buckling of longitudinal reinforcing bars (Fig. 4.1b) is also a key damage state, because unlike less severe levels of flexural damage, bar buckling requires extensive repairs (Lehman et al. 2001), significantly reduces the structure's functionality (Eberhard 2000), and has clear implications for structural safety.

This chapter describes the PEER Structural Performance Database used to calibrate the proposed damage models. The proposed relationships between column drift ratio and both damage states are derived, along with the associated fragility curves. The proposed relationships are applied to typical I-880 testbed columns.

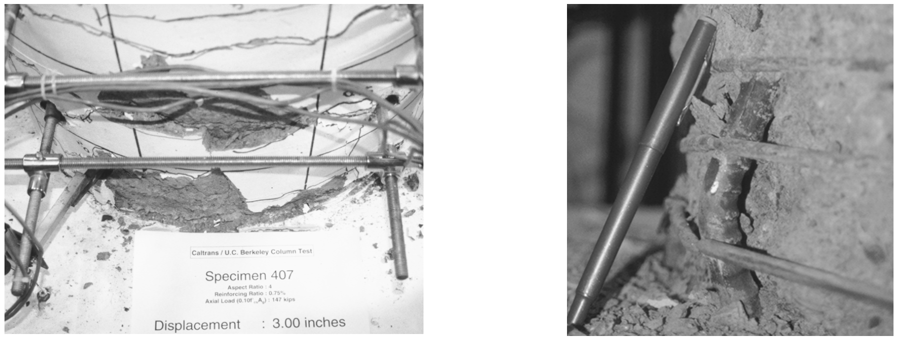

(a) **(b)**

Fig. 4.1 (a) Cover concrete spalling and (b) longitudinal bar buckling

4.2 PEER STRUCTURAL PERFORMANCE DATABASE

To calibrate models of column performance, the results of 467 cyclic lateral-load tests of reinforced concrete columns were assembled in the PEER Structural Performance Database, which is available on the World Wide Web at www.ce.washington.edu/~peera1 and http://nisee.berkeley.edu/spd/. For each test, the database provides the column geometry, material properties, reinforcement details, loading configuration, a reference, and test results. The test results provided include the digital force-displacement history for the column (or in a few cases, the force-displacement envelope), as well as the maximum column deflection imposed before reaching various damage states (Δ_{damage}), including cover concrete spalling (Δ_{spall}) and the onset of bar buckling (Δ_{bb}). The definition of Δ_{damage} is illustrated in Figure 4.2. The user's manual for the database (Berry and Eberhard 2004), which can be downloaded from either website, describes the database in detail.

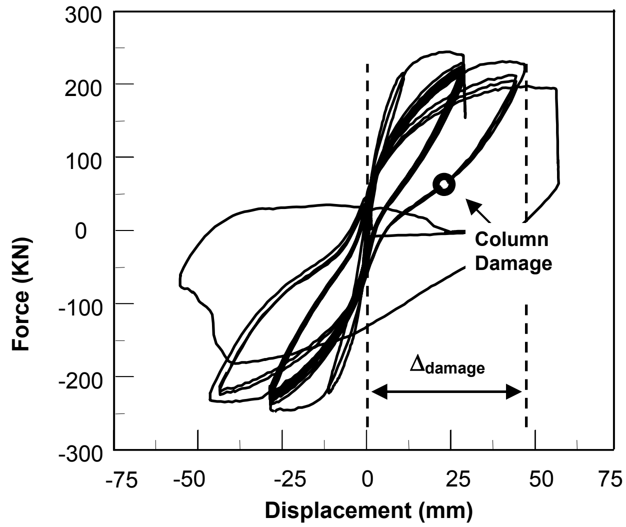

Fig. 4.2 Definition of displacement preceding column damage

The tests were screened according to the following criteria: (1) the column needed to be flexure-critical, as defined by Camarillo (2003), (2) the aspect ratio had to exceed 1.9, (3) the longitudinal reinforcement had to be continuous (unspliced), and (4) the displacement preceding cover concrete spalling or longitudinal bar buckling had to be documented. Table 4.1 provides statistics of the drift ratios at cover concrete spalling and longitudinal bar buckling for the column tests that met the screening criteria. Berry and Eberhard (2003) provide a list of the column tests and maximum column deformations prior to the onset of damage.

Table 4.1 Statistics of damage deformations

	Statistics	Rectangular	Spiral
D_{spall}/L (%)	n	102	40
	min	0.13	0.61
	max	3.04	4.51
	mean	1.53	2.29
	COV	0.48	0.44
D_{bb}/L (%)	n	62	42
	min	1.81	2.27
	max	9.25	14.58
	mean	5.34	6.55
	COV	0.33	0.43

4.3 DERIVATION OF *EDP/DM* DAMAGE FUNCTIONS

Damage progression in a reinforced concrete column is complex. A comprehensive model of column damage in seismic applications would account for the moment gradient along the column length; the complex strain-dependent interaction between the concrete cover, concrete core, transverse ties, and longitudinal reinforcement; and the full cyclic deformation history of the column (Berry and Eberhard 2003). Although existing models provide valuable insight into key factors that contribute to cover concrete spalling and bar instability, complete models of cover spalling or bar buckling have not yet been developed.

A practical model, calibrated with numerous observations of cover spalling and bar buckling during cyclic lateral tests of reinforced concrete columns, is needed for earthquake engineering applications. Berry and Eberhard (2003) combine plastic-hinge analysis with approximations for the column yield displacement, plastic curvature, buckling strain, and plastic-hinge length to develop three relationships linking column damage to three commonly used engineering demand parameters (plastic rotation, drift ratio, and displacement ductility). This chapter focuses on the drift ratio relationship (Eq. 4.1), since drift ratio is the easiest of these quantities to compute. In particular, the drift ratio can be calculated without estimating the yield displacement, an estimate that introduces further error.

$$\frac{\Delta_{damage}}{L} = \frac{\lambda}{3E_s} f_y \frac{L}{D} + C_0\left(1 + C_1\rho_{eff}\right)\left(1 + C_2\frac{P}{A_g f'_c}\right)^{-1}\left(1 + C_3\frac{L}{D} + C_4\frac{f_y d_b}{D}\right) \tag{4.1}$$

where C_0 to C_4 are constants that can be determined upon calibration with experimental results.

The experimental data support the general form of Equation 4.1. For example, Figure 4.3 (rectangular-reinforced columns) and Figure 4.4 (spiral-reinforced columns) show the variation of the drift ratio at the onset of bar buckling as a function of key column properties. To isolate the effect of each property, the database was organized into families, in which all columns in a family had similar properties except for the property being studied. These families are connected with lines in the figures. It should be noted that the families do not take into consideration variations in the displacement history imposed on each column. As expected from (Eq. 4.1), the drift ratio at the onset of longitudinal bar buckling decreases with an increase in $P / A_g f'_c$, and increases with an increase in ρ_{eff}, $f_y d_b / D$ and L / D.

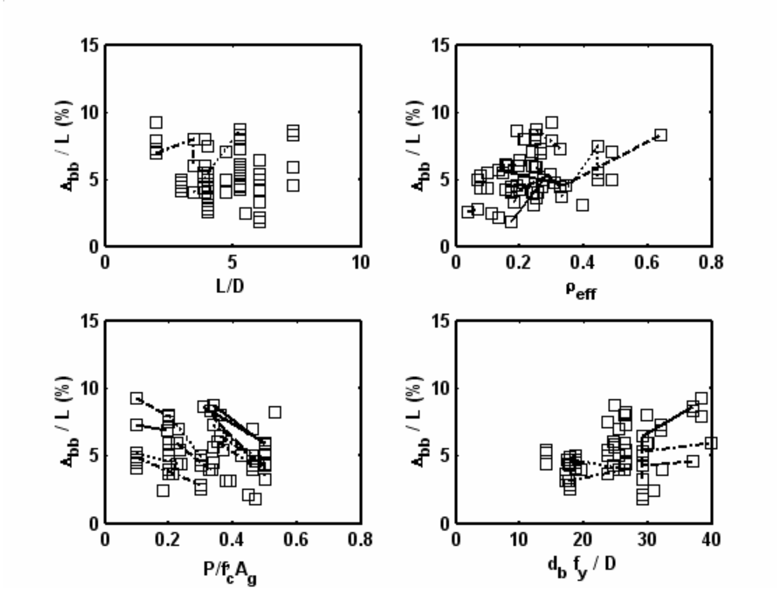

Fig. 4.3 Drift ratio at bar buckling for rectangular reinforced columns

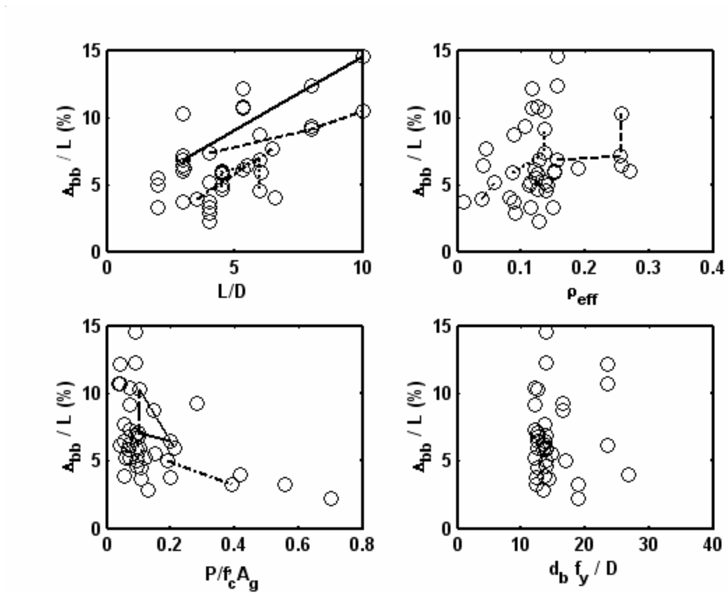

Fig. 4.4 Drift ratio at bar buckling for spiral-reinforced columns

The column database was used to calibrate the column deformation relationships. Specifically, the values of the unknown constants (C_0 ...C_4) in Equation 4.1 were determined such that (1) the ratios of the measured damage displacements (from the column database) to the calculated damage displacements had a mean value equal to 1.0 and (2) the coefficient of variation (COV) of the ratios was minimized. The resulting values of the constants for each measure of column deformation are provided in Table 4.2, along with statistical measures of the accuracy of the resulting equations.

Table 4.2 Results of regression analyses

		Δ_{spall}/L		Δ_{bb}/L	
		Rectangular-Reinforced	Spiral-Reinforced	Rectangular-Reinforced	Spiral-Reinforced
Coefficients	C0	2.1	2.8	1.5	0.31
	C1	0.0	0.0	1.3	5.7
	C2	2.0	4.2	1.9	2.8
	C3	-0.09	0.07	0.29	1.8
	C4	0.02	-0.02	0.078	0.47
Statistics of D_{bb}/D_{calc}	Min	0.12	0.56	0.37	0.58
	Max	1.90	1.67	1.63	1.46
	Mean	1.00	1.00	1.00	1.00
	COV	0.42	0.33	0.26	0.22

Berry and Eberhard (2003) showed that the accuracies of the estimates of Δ_{damage} calculated with Equation 4.1 could be increased slightly by using more complex models. However, the increases in accuracy did not justify the added complexity. Some of the scatter in the values of $\Delta_{damage} / \Delta_{damage\_calc}$ likely arises from the influence of repeated deformation cycling (Kunnath et al. 1997; Ranf et al. 2003). In addition, the identification of damage states is subjective and may vary among observers. The typical practice of imposing a series of successively increasing cycles to discrete levels of deformation leads to further scatter. For example, consider Figure 4.2, in which damage is identified to occur after an imposed displacement of 50 mm. It is clear that the damage did not occur at a displacement of 25 mm, but it is impossible to know whether the damage would have occurred if a displacement between 25 mm and 50 mm had been imposed on the column.

The complexity of Equation 4.1 makes it cumbersome for design, so simpler versions were developed. The drift ratio at the onset of cover concrete spalling for both rectangular-reinforced and spiral-reinforced columns can be approximated by

$$\frac{\Delta_{spall\_calc}}{L}(\%) = 1.6\ \left(1 - \frac{P}{A_g f'_c}\right)\left(1 + \frac{L}{10D}\right) \qquad (4.2)$$

The drift ratio at the onset of bar buckling can be approximated with

$$\frac{\Delta_{bb\_calc}}{L}(\%) = 3.25\,(1 + k_{e\_bb}\rho_{eff}\frac{d_b}{D})\,(1 - \frac{P}{A_g f'_c})\,(1 + \frac{L}{10D}) \tag{4.3}$$

where k_{e_bb} = 50 for rectangular-reinforced columns and 150 for spiral-reinforced columns. The transverse and longitudinal reinforcement properties controlling the onset of bar buckling have been combined into a new parameter, $k_{e\_bb}\rho_{eff} d_b / D$. Statistical measures of the accuracy of Equations 4.2 and 4.3 are provided in Table 4.3.

Table 4.3 Statistics of accuracy of *EDP/DM* equations

	$\Delta_{spall}/\Delta_{spall\_calc}$		$\Delta_{bb}/\Delta_{bb\_calc}$	
	Rectangular-Reinforced	Spiral-Reinforced	Rectangular-Reinforced	Spiral-Reinforced
Min	0.12	0.56	0.32	0.47
Max	1.90	1.67	1.37	1.46
Mean	1.0	1.0	1.0	0.97
COV	0.42	0.33	0.26	0.25

Berry (2003) shows that the accuracies of Equations 4.2 and 4.3 do not vary significantly with the axial-load ratio, aspect ratio, effective confinement ratio, longitudinal reinforcement ratio, or the ratio of the confinement spacing to the bar diameter (s/db).

4.4 DEVELOPMENT OF FRAGILITY FUNCTIONS

To estimate the likelihood of cover concrete spalling and bar buckling, Equations 4.2 and 4.3 can be combined with fragility curves, such as those shown in Figure 4.5. This figure shows the cumulative probability of cover spalling and bar buckling as functions of $\Delta_{damage} / \Delta_{damage\_calc}$ for the database, as well as the corresponding normal cumulative distribution functions (CDF) and the lognormal CDF.

To apply Equations 4.2 and 4.3 in practice, it is necessary to assume that the database is representative of the general population of rectangular- and spiral-reinforced columns. To evaluate existing columns, the displacement demand, Δ_{demand}, is estimated based on an analysis of the full structure. The estimated displacement at bar buckling, $\Delta_{demand} / \Delta_{bb\_calc}$, is then calculated with Equation 4.2 or 4.3 based on the known column properties. The probability that a longitudinal bar will have buckled at or before that displacement demand is then evaluated from the appropriate fragility curve (CDF) shown in Figure 4.5. For example, if $\Delta_{demand} / \Delta_{bb\_calc}$ is equal to 2/3 for a spiral-reinforced concrete column, the probability that a bar will have begun to buckle at or before the displacement demand is 10%.

These general fragility curves can be used to develop fragility curves for a specific column by multiplying $\Delta_{demand} / \Delta_{damage\_calc}$ by Δ_{damage_calc} / L from Equations 4.2 and 4.3. For example, if Equations 4.2 and 4.3 are applied to a typical I-880 column ($k_e = 150$, $\rho_{eff} = 0.11$, $d_b / D = 0.016$, $P / A_g f_c' = 0.044$, $L / D = 2.84$) the resulting mean drift ratios are $\Delta_{spall\_calc} / L = 1.96\%$ and $\Delta_{bb\_calc} / L = 5.1\%$.

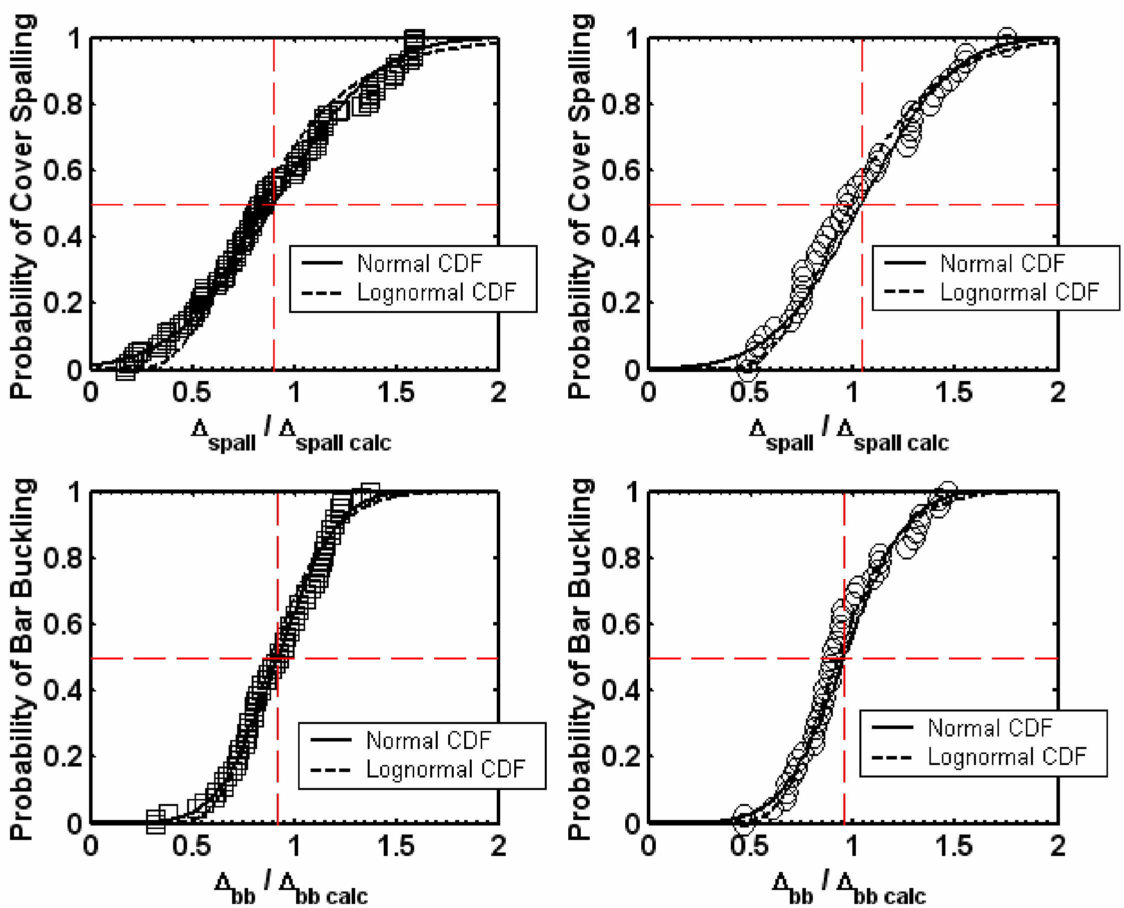

Fig. 4.5 Fragility curves for onset of bar buckling

When the x-axes of the general fragility curves (Fig. 4.5) are multiplied by these mean values, the I-880 specific fragility curves are obtained (Fig. 4.6). The term "typical I-880 column" is used here to convey the meaning that the drift demands in all the columns for these damage states are similar. Following an analysis of all the columns in the three-frame viaduct model used in this study, it was found that the expected demands at spalling and bar buckling were practically identical. For example, the estimated mean drift at bar buckling in the critical bent (the bent that most often experienced the maximum drift for all records) was 5.5%, while the mean drift at bar buckling across all eleven bents was 5.6%. Therefore, the fragility functions shown in Figure 4.6 are used in this study for all columns in the I-880 model.

These column-specific fragility curves are useful tools when studying the probability of column damage. For example, if the deformation demand on an I-880 column is $\Delta_{demand} / L = 4.0$, the probability that the cover concrete will have spalled at or before that demand is 98% and the probability that the longitudinal reinforcement will have begun to buckle at or before that demand is 20%.

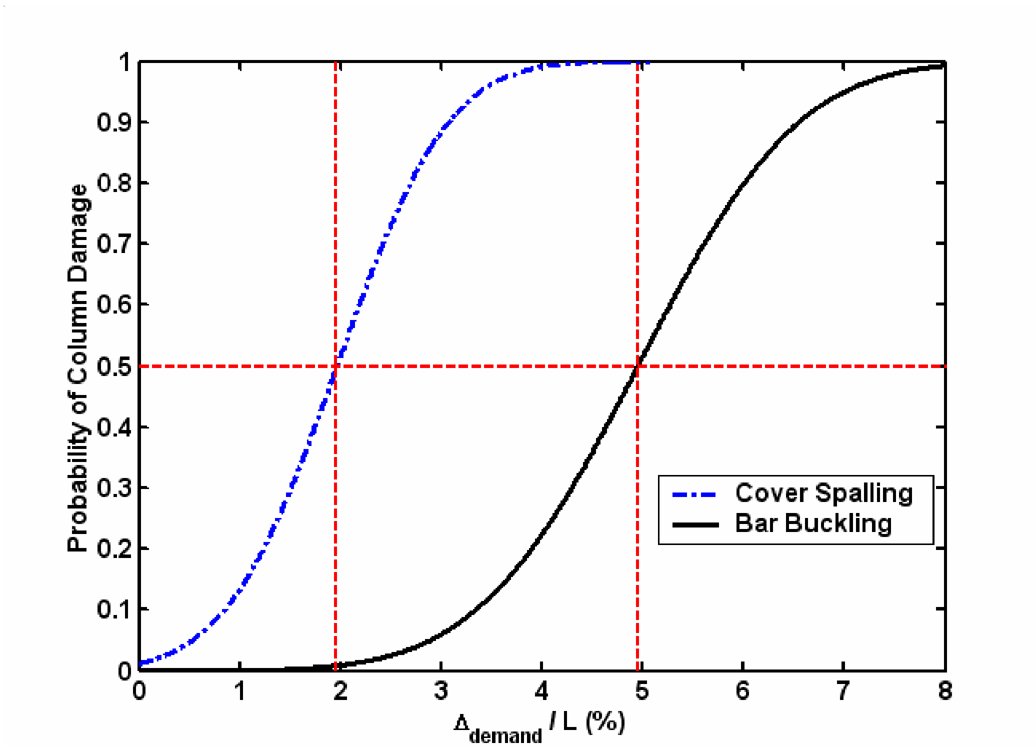

Fig. 4.6 Fragility curves for typical I-880 column

4.5 CONCLUSIONS

The PEER Structural Performance Database provided the information needed to evaluate the accuracy of performance models for reinforced concrete columns. The data made it possible to develop a necessary, quantitative link between lateral deformations in flexure-dominant reinforced concrete columns, and the onset of cover concrete spalling and longitudinal bar buckling.

The mean value of $\Delta_{demand} / \Delta_{damage\_calc}$ was near 1.0 for both damage states, and for both spiral-reinforced and rectangular reinforced concrete columns. For concrete spalling, the coefficients of variation of this ratio were 42% for rectangular-reinforced columns and 33% for spiral-reinforced columns. For both the rectangular and spiral columns, the coefficient of variation of this ratio was near 25% for bar buckling. The accuracy improves slightly if a more complex expression is used, but the increase in accuracy does not justify the increased complexity. By solving Equation 4.3 for the effective confinement ratio, it is also possible to proportion the confinement reinforcement for new columns, based on the column properties, the expected column deformation, and the specified probability of bar buckling.

A comprehensive performance evaluation of a bridge would also consider other types of damage, including spalling and settlement of the abutments, cracking and spalling of the joints, superstructure unseating and restrainer elongation at the joints, and damage to intermediate foundations.

5 Loss Analysis: Investigating Closure Probability of I-880 Viaduct

Sashi Kunnath
University of California at Davis

In Chapter 3, the simulation model of the I-880 viaduct was subjected to 30 scaled ground motions corresponding to three hazard levels. A selected *EDP* was monitored for each analysis and a probabilistic evaluation was carried out to establish the mean annual frequency of exceeding the *EDP* measure. In the previous chapter, fragility functions for two damage measures (*DM*s) conditioned on the selected *EDP* were derived. Before proceeding to the next step in the process, it must be reiterated that the choice of the *EDP* was constrained by the *DM* and that the choice of the *DM* was motivated by the need to use practical visual measures at the structural element level that serve as the primary indicators of damage in rapid post-earthquake reconnaissance. Numerous other measures of demand and damage could also have been used but the intent of this report is to demonstrate the application of the methodology with a selected subset of parameters.

Having examined the demand as a function of the ground motion intensity measure and having set up a probability distribution for selected damage measures as a function of the demand, we now consider the third element in the PEER framework, namely, loss modeling. This phase of the assessment is central to the PEER methodology, since it distinguishes it from other performance-based procedures. While the framework equation implies that the decision variable is conditioned on the damage measure, it is possible to recast the equation to assess losses conditioned directly on the ground motion intensity measure or an engineering demand parameter. In the context of bridge evaluation, possible measures of economic loss are *replacement cost* of the bridge in the event of collapse or irreparable damage, and *closure probability* (including duration of closure) of the bridge for less severe damage. One potential approach to defining and incorporating such a loss measure is presented in this chapter.

5.1 DECISION VARIABLES

Limited research has been conducted on the relationship between bridge damage and bridge performance. In conversations with Caltrans engineers as part of the I-880 testbed project, an attempt was made to describe post-earthquake decision making in terms of performance levels and observed damage. Table 5.1 provides an overview of the relationship between such damage states and the possible actions that might result during post-earthquake reconnaissance.

Table 5.1 Likely decision scenarios arising from observed bridge damage

Performance	Damage State	Decision/Action
Immediately Operational	No evidence of concrete spalling; no significant roadway discontinuities such as expansion joint or abutment movement	Leave open; conduct detailed investigation later and repair any minor damage
Operational	Nonstructural damage and noticeable movement or settlement of joints and supports (less than 1 in) but can be repaired in a short duration (< 3 days)	Partially or fully close bridge (depending on number of traffic lanes); repair damage and reopen
Life Safety	Structural damage; lateral capacity possibly impaired; exposed reinforcement; significant movement and/or settlement at joints and supports	Close bridge, shore and then reopen with certain constraints (reduced load and speed limits) while repair is in progress
Collapse Prevention	Significant reduction in lateral and vertical load capacity; large permanent displacements	Close bridge; for critical bridge — repair or replace (whichever is faster); for noncritical bridge — whichever is cheaper

The primary decision that an inspector needs to make in the case of noncollapsed structures is whether to keep the bridge open to traffic and/or emergency vehicles. A recent study by Porter (2004) in collaboration with other PEER investigators examined the possible relationship between *DM* and one *DV* of interest, namely, whether a bridge will be closed after an earthquake, and if so, for how long. Porter's study is not concerned with what a bridge inspector *should* do given an observed damage state, but rather what the inspector is likely to do when confronted with a bridge with various symptoms of damage. Porter reports that the exploratory study considers only noncritical multispan highway bridges consisting of precast girders on cast-in-place bents resting on a foundation of driven prestressed concrete piles and cast-in-place pilecaps. Despite this stated limitation, the procedure offers a pattern for exploring the *DM-DV* relationship for any number of other bridge categories.

Porter's study consisted of a survey of a small group of bridge inspectors from departments of transportation across the country to determine the relationship between physical damage states and closure probability. The survey consisted of a single-page questionnaire in tabular form with *DM*s as row headers and a possible range of *DV*s as column headers. The initial list of *DM*s was based on discussion between PEER researchers and several Caltrans engineers involved in the seismic evaluation and retrofit of highway bridges. A sample section of the survey form is shown in Table 5.2. The blank column header was provided to respondents to include their own decision if the four options provided were insufficient or inappropriate.

Table 5.2 Sample section of survey (Porter 2004)

Decision → **Damage ↓**	**No closure**	**Close 1-3 days**	**Close > 3days**	**Open with reduced speed**	
Vertical offset at joint	< ½ in.	< ½ in.	< ½ in.	< ½ in.	< ½ in.
	½–1 in.	½–1 in.	½–1 in	½ - 1 in	½–1 in.
	> 1 in.	> 1 in.	> 1 in.	> 1 in.	> 1 in.
Concrete Spalling	No	No	No	No	No
	Yes	Yes	Yes	Yes	Yes
Bar Buckling	No	No	No	No	No
	Yes	Yes	Yes	Yes	Yes

A respondent would circle a likely decision given an observed damage state. As is evident from the table, the survey consisted of both scalar and binary damage measures. In the case of scalar damage measures, such as horizontal offset at the expansion joint, it is possible to develop loss functions based on a statistical analysis of the responses. If the fragility function given by $P[\,DV > dv_i \mid DM = dm_j\,]$ is approximated as a log-normal distribution function, then:

$$P[\,DV > dv_i \mid DM = dm_j\,] = \Phi\left(\frac{ln(\,dm_j \,/\, \overline{dm}\,)}{\sigma_{dm}}\right) \tag{5.1}$$

dm_j = a particular value of the damage measure (taken as the lower limit in the range)

$\overline{dm}$ = median of damage measures

σ_{dm} = standard deviation of damage measures

As an example of establishing the fragility function for bridge closure given an observed damage state, let us consider the vertical offset at an expansion joint following a seismic event. Based on the results of the survey (Table 5.1) conducted by Porter, the following statistical measures were obtained for temporary closure (≥ 1 day):

Mean displacement = 1.75 in.

Standard deviation = 0.50 in.

Application of Equation 5.1 to the above data yields the fragility function shown in Figure 5.1.

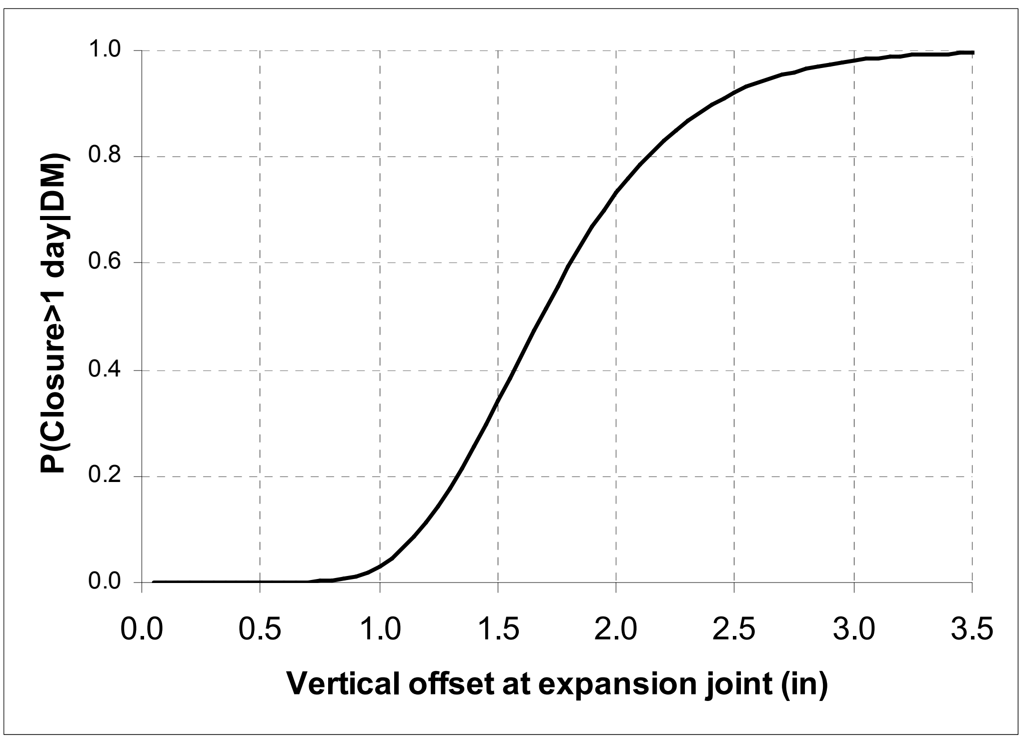

Fig. 5.1 Probability of temporary closure of a bridge as determined from survey of bridge inspectors (Porter 2004) given observed damage state at expansion joint

For the case where the response is a binary measure (Yes/No), the discrete probability is evaluated as follows:

$$P(DV \geq dv_i \mid DM_j = true) = n_r/N \tag{5.2}$$

where dv_i is the decision variable (no closure or temporary closure of the bridge), $\boldsymbol{DM}_j$ is the damage state (spalling/bar buckling), n_r is the number of respondents who feel that the damage state must be "True" to be associated with the selection decision (dv_i), and N is the total number of respondents.

Twelve survey responses were received but only those respondents who self-rated their expertise as 4 or 5 (on a 5-point scale) in responding to questions were considered in developing the closure probabilities for this study. The results indicate that 33% of the respondents would likely close the bridge at least briefly (> 1 day) if they observed concrete spalling. This figure increased to 100% for bar buckling. The survey data resulted in the following discrete probabilities:

$$P\ (DV = Closure \mid Only\ Concrete\ Spalling = True) = 0.33 \tag{5.3}$$

$$P\ (DV = Closure \mid Bar\ Buckling = True) = 1.00 \tag{5.4}$$

The above probabilities raise questions on the validity of the decisions for the stated damage states. It must be reiterated that Equations (5.3)–(5.4) are based on what a bridge inspector is likely to do in a post-earthquake assessment based on the survey as opposed to what the inspector *should* do. It may be argued that concrete spalling is not a critical damage state and experimental data suggest that the integrity of the structure is not compromised at this damage state. Assuming that the small sample collected by Porter (2004) is representative of the decisions that bridge inspectors would make after earthquakes, then there is a considerable probability of bridge closure if spalling occurs. This uncertainty in whether the bridge will be closed conditioned on the occurrence of only concrete spalling depends on the knowledge of bridge inspectors of the consequences of such level of damage. Therefore, this uncertainty can be reduced or even eliminated by improving the knowledge of bridge inspectors. For example, if through training bridge inspectors become aware that cover spalling is not a critical damage state that compromises the integrity of the structure, then well-informed bridge inspectors would most likely keep the bridge open for damage states not exceeding concrete spalling, and Equation (5.3) becomes

$$P\ (DV = Closure \mid Only\ Concrete\ Spalling = True) = 0.0 \tag{5.5}$$

The change from Equation 5.3 to Equation 5.5 in this study is an attempt to incorporate additional uncertainty that exists in the decision-making phase of the performance-based methodology.

5.2 *DV|EDP* RELATIONSHIP

The fragility functions which represent the damage probabilities for concrete spalling and reinforcing bar buckling (Fig. 4.6) can now be combined with the discrete closure probabilities (Eqs. 5.3–5.5) to determine the probability of closing the bridge given an *EDP*, as follows:

$$P(DV \mid EDP) = \sum_{i=1}^{2} P(DV \mid DM_i) dP(DM_i \mid EDP) \tag{5.6}$$

$$\begin{aligned} &= P(Closure \mid Only - Spalling)P(Only - Spalling \mid EDP) \\ &\quad + P(Closure \mid Buckling)P(Buckling \mid EDP) \end{aligned} \tag{5.7}$$

in which *P(Only-Spalling|EDP)* implies only concrete spalling without bar buckling, and *P(Buckling|EDP)* implies both spalling and buckling, since a buckled damage state occurs after spalling. The resulting cumulative probability distributions for two scenarios (closure based on Eqs. 5.3–5.4 in one case, and Eqs. 5.4–5.5 in another) are shown in Figure 5.2.

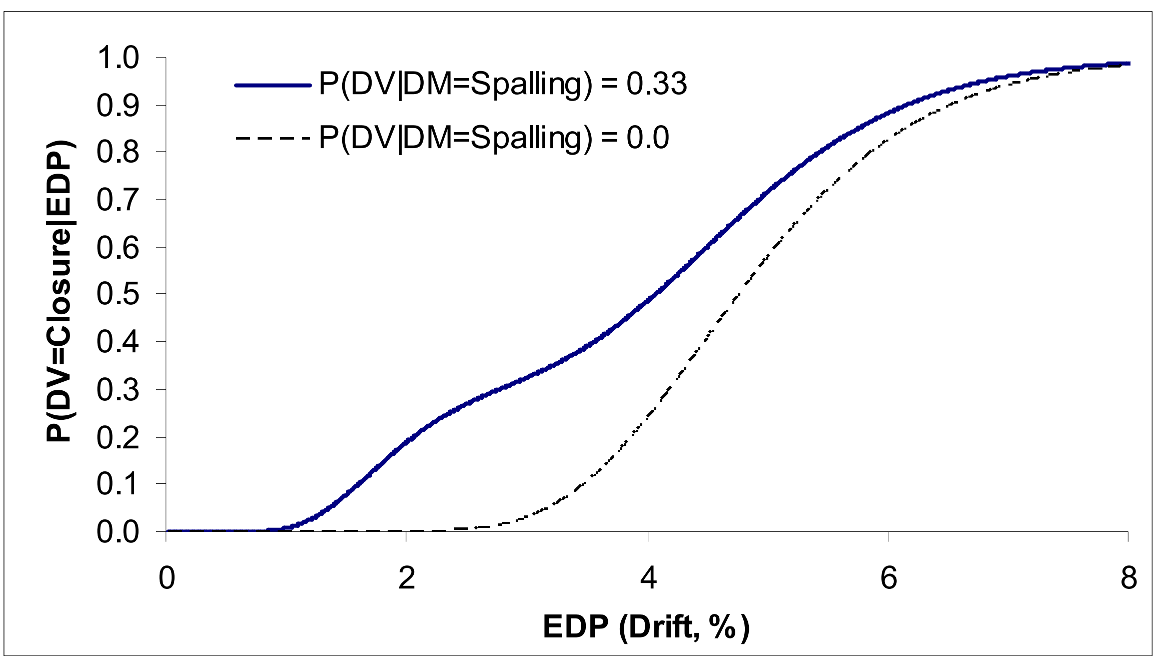

Fig. 5.2 Probability of temporary closure (≥ 1 day) as a function of selected *EDP* measure (tangential drift) for two decision scenarios

5.3 *DV-IM* RELATIONSHIP

One final step remains. This involves integrating the seismic hazard curve into the evaluation methodology as implied in the PEER framework equation. Using the total probability theory, the probability of closure given an intensity measure (*IM*) is

$$P(DV > dv \mid IM) = \int_{0}^{\infty} P(DV > dv \mid EDP) \left| \frac{dP(EDP \mid IM)}{dEDP} \right| dEDP \tag{5.8}$$

The first term on the right-hand side of Equation 5.8, *P(DV>dv|EDP)* expresses the probability of temporary closure given damage states corresponding to spalling or bar-buckling. In order to evaluate the second term that appears on the right hand side of the above expression, it is first necessary to determine *P(EDP|IM)* for each hazard level. Assuming a lognormal distribution, and using the variation of median *EDP* with changes in *IM* shown in Equation (3.8), this conditional probability is computed as

$$P(EDP > edp \mid IM = im) = 1 - \Phi\left(\frac{ln\left(\frac{edp}{a(im)^{b}} \right)}{\sigma_{ln(edp|im)}} \right) \tag{5.9}$$

where $IM = S_a(T)$ is the intensity measure, $\Phi[\ ]$ is the standard normal distribution function, and $\sigma_{ln(EDP|IM)}$ is the standard deviation of the natural log of the *EDP*s computed at the ground motion intensity level, *im*.

Returning to Equation (5.8), the second term on the right-hand side can be re-written as

$$P(DV > dv \mid IM) = \int_{0}^{\infty} P(DV > dv \mid EDP) \left| \frac{dP(EDP \mid IM)}{dEDP} \right| dEDP \tag{5.9}$$

Equation 5.9 is evaluated numerically. By assumption, each *DV* is dependent on a single *EDP*. This means that each *edp* that is associated with the term $\left| \frac{dP(EDP \mid IM)}{dEDP} \right| dEDP$ in Equation 5.9 provides a single value for the annual probability of closure when integrated with the term $P(DV \mid EDP)$. Therefore, applying Equation 5.9 to a *series* of *EDPs* will give the annual probability of closure. Figure 5.3 shows the probability of closing the bridge for at least one day for two different decision scenarios. The higher closure probability resulting from a decision to close the bridge (even temporarily) due to observed spalling in bent columns raises issues related to adequate training of bridge inspectors to avoid indirect economic losses from unnecessary bridge closures.

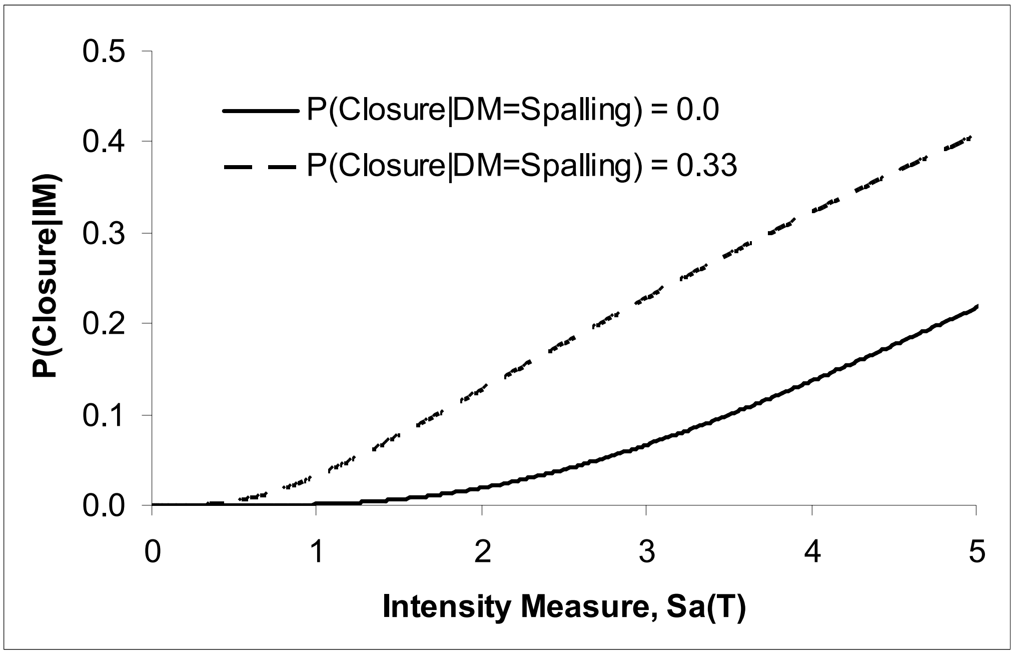

Fig. 5.3 Probability of temporary closure as a function of selected intensity measure for two decision scenarios

5.4 CLOSURE PROBABILITY OF I-880 VIADUCT

The mean annual frequency of closure is given by

$$\nu(DV) = \int_0^\infty P(DV > dv \mid IM) \left| \frac{d\lambda(IM)}{dIM} \right| dIM \tag{5.10}$$

The slope of the hazard curve was derived earlier in Equation (3.4). In equation (5.10) it is assumed that the probability of bridge closure is zero if the ground motion intensity is smaller or equal to 0.02g. This is equivalent to integrating from this intensity value instead of from zero as implied in equation (5.10). It should be noted that integrals in Equations (5.9) and (5.10) are evaluated numerically to obtain the mean annual frequency of closure; hence it is not necessary to assume that the dispersion of the structural response, $\sigma_{ln(EDP|IM)}$, remains constant with changes in *IM* as done in Cornell et al. (2002). Here, a piece-wise linear variation passing through the dispersion computed at the three levels of seismic hazard shown in Figure 3.7 was assumed. Alternatively, one can also use a smooth variation of dispersion with changes in *IM* as suggested by Miranda and Aslani (2003). If the mean annual frequency is smaller than 10^{-2}, then it will, numerically, be practically equal to the annual probability of closure. Hence, the probability of closure in *n* years is approximately given by

$$P(Closure) \approx 1 - \left[1 - \nu(DV)\right]^{n} \tag{5.11}$$

Equations (5.10)–(5.11) are based on some simplifying assumptions. They assume that earthquake occurrence at the site follows a Poisson process and that any damage is repaired so that the bridge is restored to its original condition prior to the occurrence of the next damaging event. Equation (5.11) assumes that repeated annual events are statistically independent; however, since there is uncertainty associated with the reserve capacity in the system, these repeated events cannot strictly be statistically independent. This source of statistical dependence is not considered.

Applying Equation 5.10 to the I-880 simulations, the closure probabilities of the bridge are evaluated assuming two decision scenarios: that a damage state corresponding to spalling will not result in closure of the bridge (fragility function represented by the dashed line in Figure 5.2) or that some inspectors are likely to close the bridge (though temporarily) if concrete spalling is observed. As pointed out earlier, this represents one of the uncertainties that exists in the decision-making phase of the performance-based methodology. The consequence of dealing with this uncertainty was demonstrated in Figure 5.3, where it is plainly evident that the probability of closing the bridge can be significantly reduced if closure decisions are based on more rational judgments.

It was determined that the probability of closure in 50 years ($n = 50$ in Eq. 5.11) would drop significantly from 1.16% to 0.09% if bridge inspectors opted to leave the bridge open for damage states less than or equal to spalling of the concrete cover.

6 Uncertainty and Reliability Analysis

Terje Haukaas[1] and Armen Der Kiureghian[2]
[1]*University of British Columbia, Vancouver, Canada*
[2]*University of California, Berkeley*

6.1 INTRODUCTION

A significant novelty of this report is the utilization of complementing probabilistic approaches to the I-880 bridge structure. The preceding chapters have introduced the fundamental probabilistic concepts, as well as probabilistic models for capacity and demand considerations. This chapter represents a further extension of this effort by introducing full-scale structural reliability analysis. The amalgamation of reliability methods and the finite element model of the I-880 bridge is termed “finite element reliability analysis.” In essence, the approach entails the characterization of all input parameters as random variables to compute the probability of user-specified response events. The methodology is motivated by the recognition that even with sophisticated structural analysis models, response predictions can be made only in a nondeterministic manner. Unavoidable uncertainties are present in the material properties, geometry, loads, as well as in the models themselves.

In this chapter, the I-880 highway bridge testbed is considered for reliability analysis. The reliability analysis presented in the following provides an alternative means of evaluating the same probability described in the PEER triple integral. By incorporating the various models into the reliability analysis, which in fact entails the approximate solution of a multifold integral, the multiple integral in Equations (1.4) and (1.5) are effectively evaluated.

A version of the finite element simulation model described in Chapter 2 is analyzed by utilizing the reliability tools in OpenSees. A frame consisting of four bents is considered and both static pushover and dynamic analysis are conducted. Figure 6.1 depicts the general features of the model which represent the interior segment of the three-frame model described in Chapter 2. Node and element numbers are identified for subsequent discussion of the reliability results.

As mentioned in Chapter 2, the soil-foundation system is modeled using spring elements. The bridge is analyzed as a free-standing structure with no interaction effect from adjacent frames. All parameters describing material properties, cross-sectional geometry, and nodal coordinates are characterized as random variables. Tables A.1–A.4 list the probabilistic information employed in the subsequent analyses. A total of 320 random variables are considered. Aside from determining the propagation of uncertainties and probabilities for specified limit states, an important purpose of the reliability analysis is to determine parameter importance measures in order to identify the most significant sources of uncertainty.

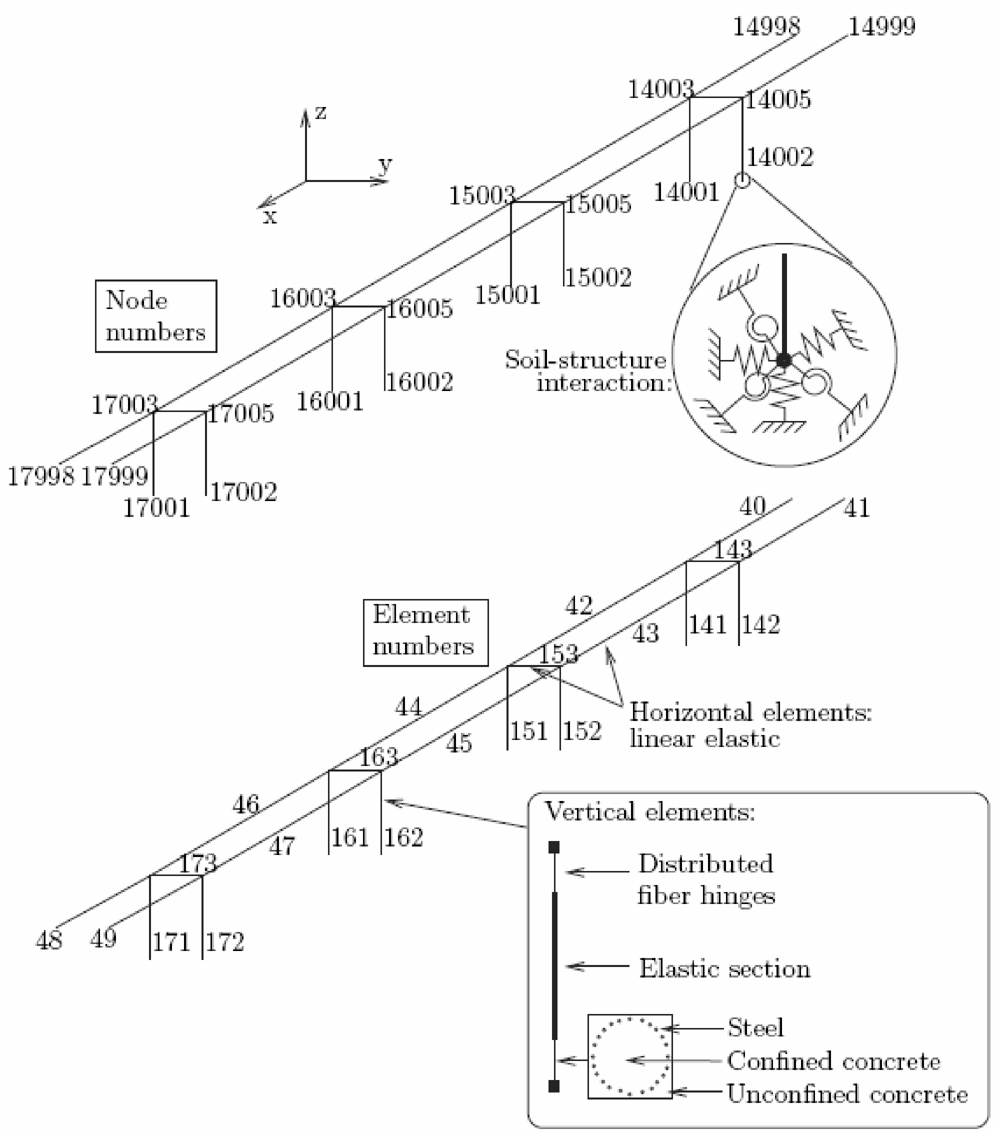

Fig. 6.1 Identification of node and element numbers for I-880 testbed bridge model

6.2 BRIEF REVIEW OF RELIABILITY ANALYSIS

Structural reliability methods are employed in performance-based engineering to obtain probability estimates for various performance events. Structural performance is usually specified in terms of structural response quantities, such as strains and displacements, stresses and forces, and cumulative response measures, such as cumulative plastic strain or cumulative dissipated energy. In the PEER terminology, these are known as engineering demand parameters (*EDP*s). *EDP*s, in turn, are functions of the ground motion intensity, or intensity measures (*IM*s) in the PEER terminology. On the other hand, from an owner's or decision-maker's perspective, performance events must be defined in terms of decision variables (*DV*s), which characterize the cost associated with different structural performance outcomes, e.g., the costs of repair and loss of function of a bridge as a result of an earthquake. *DV*s in general depend on the state of the structure as characterized by a set of damage measures (*DM*s). For example, different levels of drift may be used as indicators of different levels of damage to a bridge or building. *DM*s in general are functions of *EDP*s. Thus, using underlines to denote vector-valued quantities, one can write $\underline{DV}(\underline{DM}(\underline{EDP}(\underline{IM})))$. Each of the relationships $\underline{DV}(\underline{DM})$, $\underline{DM}(\underline{EDP})$ and $\underline{EDP}(\underline{IM})$ is a mathematical model. Some of these models are well developed, while others are subjects of current research within and outside PEER.

In addition to the above, in reliability analysis we must consider the uncertain quantities affecting each of the measures $\underline{IM}$, $\underline{EDP}$, $\underline{DM}$, and $\underline{DV}$. These include material and geometric properties of the structure, as well as the applied loads. Additional uncertainties are present in the models used to describe the relations between these measures. Two types of uncertainty may be considered: (a) time-invariant uncertain quantities, such as material properties and structure geometry, which are characterized by a vector of basic random variables $\mathbf{x}$ and (b) time-variant uncertain quantities, such as the components of ground motion, which are characterized by a vector of stochastic processes $\mathbf{y}(t)$. In the presence of these uncertainties, obviously $\underline{IM}$, $\underline{EDP}$, $\underline{DM}$, and $\underline{DV}$ are also uncertain. Two objectives are then sought from reliability analysis: (a) estimation of the uncertainty in these measures arising from the uncertainties in $\mathbf{x}$ and $\mathbf{y}(t)$, and (b) estimation of the probability of various events defined in terms of *EDP*s, *DM*s, or *DV*s. An equally important objective is to identify variables or stochastic processes that are important sources of uncertainty. Tools currently available in OpenSees for such analysis are briefly described in the following subsections. Because of the limited scope of this report, the presentation is limited to time-invariant uncertainties. Furthermore, important issues such as the nature of uncertainties (aleatory or epistemic) and modeling and statistical uncertainties are not addressed.

6.2.1 Characterization of Performance Events

A performance event, in general, may be defined in terms of one or more limit-state functions involving *DV*s, *DM*s, *EDP*s and, through them, implicitly, the basic random variables $\mathbf{x}$. For example, the event that the sum of two *DV*s, for example, the costs of repair and loss of function of a bridge, exceeds a threshold dv_0 can be expressed as

$$\{g(\mathbf{x}) \leq \mathbf{0}\} \tag{6.1}$$

with

$$g(\mathbf{x}) = \mathbf{dv_0} - \mathbf{DV_1}(\underline{\mathbf{DM}}(\underline{\mathbf{EDP}}(\mathbf{x}),\mathbf{x}),\mathbf{x}) - \mathbf{DV_2}(\underline{\mathbf{DM}}(\underline{\mathbf{EDP}}(\mathbf{x}),\mathbf{x}),\mathbf{x}) \tag{6.2}$$

In the above, we have explicitly shown the dependence of *DV*s on the *DM*s and *EDP*s, and through them on the basic random variables $\mathbf{x}$. Furthermore, we have allowed explicit dependence of *DM*s and *DV*s on the basic random variables $\mathbf{x}$. This is to allow direct dependence of the *DM*s and *DV*s on certain random variables, which may describe such uncertain quantities as damage thresholds and costs of repair. For reliability analysis, it is necessary that all functions described above be continuous and differentiable with respect to $\mathbf{x}$. If this is not the case, then the problem must be defined in terms of several limit-state functions, as described below.

6.2.2 Sensitivity Analysis

An essential ingredient for uncertainty and reliability analysis is the gradient (partial derivatives) of the limit-state function with respect to the basic random variables $\mathbf{x}$. In the context of finite element analysis, this implies the need for computing the sensitivities of the structural response (*EDP*s) with respect to material, geometry and load parameters. Tools for such sensitivity analysis have been developed and implemented in OpenSees by Haukaas and Der Kiureghian (2004). The direct differentiation method (DDM) has been used. This involved the development and implementation of the derivatives of the time- and space-discretized finite element equations at the global, element and material levels. This method has the advantage that the computed sensitivities are consistent with the finite element approximations, and they are computed accurately and efficiently. When the limit-state function includes *DM*s and *DV*s, derivatives of these measures with respect to *EDP*s are needed for use in a chain rule to compute the derivatives with respect to **x**. Since the relations between these measures are typically simple and do not involve finite element computations, the needed derivatives can be either derived analytically or computed by finite differences.

6.2.3 Uncertainty Modeling

A comprehensive library of probability distributions is available in OpenSees. Using the Nataf model (Liu and Der Kiureghian 1986), multivariate distributions are defined by specifying marginal distributions from the library and a correlation matrix. Several options and library models are available for defining the correlation coefficients among the set of random variables. Tools are made available to declare material and load parameters or nodal coordinates as random variables. A stochastic model for specifying the earthquake ground motion as a filtered train of random pulses is also included. This model allows consideration of both temporal and spectral nonstationarity in the ground motion.

6.2.4 Uncertainty Analysis

An important objective in uncertainty analysis is to compute the variance of a *DV*, a *DM*, or an *EDP*. These are equivalent to computing the variance of a function $g(\mathbf{x})$ of the basic random variables $\mathbf{x}$. Two options are presently available in OpenSees for this purpose: (a) Monte Carlo simulation (b) first-order second moment (FOSM) analysis. The latter involves expanding the function around the mean of $\mathbf{x}$ and truncating the series after the first-order terms. The resulting approximation of the variance of $g(\mathbf{x})$ is (Ang and Tang 1975):

$$\sigma_g^2 \cong \sum_i \sum_j \frac{\partial g}{\partial x_i} \frac{\partial g}{\partial x_j} \rho_{ij} \sigma_i \sigma_j \tag{6.3}$$

where $\partial g / \partial x_i$ is the sensitivity with respect to x_i computed at the mean point, σ_i is the standard deviation of x_i, and ρ_{ij} is the correlation coefficient of x_i and x_j. Since sensitivities are available in OpenSees, this estimate of the variance is easily computed with a single finite element run. The direct contribution of a random variable x_i to the variance is $(\partial g / \partial x_i \, \sigma_i)^2$.

Thus, the product $\left|\partial g / \partial x_i\right| \sigma_i$ is a measure of importance of x_i in contributing to the total uncertainty in $g(\mathbf{x})$. These importance measures as well as the variance estimate Equation (6.3) are available as output from FOSM analysis in OpenSees.

6.2.5 Reliability Analysis

Reliability analysis deals with computing probability estimates for performance events such as in (6.1). Methods implemented in OpenSees so far include Monte Carlo simulation, importance sampling using design points, and the first-order reliability method (FORM) for components and series systems. The latter method employs a linearization of the limit-state surface at a "design point," which is the outcome point of the random variables with maximum likelihood in the failure domain. Importance sampling uses simulations centered at the design point. This method is far more efficient than the crude Monte Carlo method, which uses simulations centered at the mean point of the random variables. The design point is obtained as the solution of a constrained optimization problem employing the gradient vector of the limit-state function. Hence, FORM and importance sampling make use of the sensitivity capabilities available in OpenSees.

An important advantage of FORM is that it provides, in addition to a first-order approximation of the probability estimate, measures of parameter importance and reliability sensitivities. Specifically, three importance vectors are provided: vector $\boldsymbol{\gamma}$ that lists the relative contributions of the random variables to the variance of the limit-state function near the design point, vector $\boldsymbol{\delta}$ that lists the relative importance of the random variables with respect to scaled variations in their means, and vector $\boldsymbol{\eta}$ that lists the relative importance of the random variables with respect to scaled variations in their standard deviations. These vectors, which are provided as part of the standard output from FORM analysis in OpenSees, can be used to gain insight into the important sources of uncertainty in a problem. This information can be used to simplify the model, e.g., replace unimportant random variables with deterministic values, or to determine where additional data gathering efforts can be fruitful.

6.3 APPLICATION TO I-880 TESTBED

6.3.1 Probabilistic Pushover Analysis

First, a probabilistic pushover analysis is performed with the model of the bridge in Figure 6.1. The horizontal displacement at node 15005, denoted u, is computed for horizontal loads applied at nodes 1403, 1503, 1603, and 1703 with a load factor λ. Figure 6.2a shows the conditional mean and the mean $\pm$ standard deviation of u for given λ, and Figure 6.2b shows the conditional mean and the mean $\pm$ standard deviation of λ for given u, both computed by FOSM analysis. Both diagrams show that the uncertainty in the response increases with increasing nonlinearity. This is expected, since nonlinear response is more sensitive to uncertainties in the system parameters. It is noted that for each given value of u or λ a single finite element analysis together with sensitivities is carried out.

Suppose we set the displacement and load capacities of the structure as the values at which the tangent stiffness of the structure down-crosses a threshold equal to 20% of the initial elastic stiffness (Vamvatsikos and Cornell 2002). We denote these capacities as $u_{(\text{at 20\% tangent})}$ and $\lambda_{(\text{at 20\% tangent})}$. With uncertain system characteristics, naturally these capacity values are also uncertain. FOSM analysis with OpenSees reveals that $u_{(\text{at 20\% tangent})}$ has a mean of 0.253 m and a standard deviation of 0.017 m, resulting in a coefficient of variation (COV) of 6.6%, and that $\lambda_{(\text{at 20\% tangent})}$ has a mean of 0.201 and a standard deviation of 0.010, resulting in a COV of 4.8%. It appears that the uncertainty in the displacement capacity is much larger. However, both COVs are much smaller than the COVs assumed for the concrete materials and soil stiffnesses.

Importance measures based on FOSM are computed for each of the above response quantities. As expected, these measures vary depending on the considered response quantity and the location within the load-displacement curve. Here, we report some of the results for the propagation of uncertainty in u for given λ (i.e., the case in Fig. 6.2a). Tables A.5 and A.6 (see Appendix) list the forty most important and forty least important variables in the initial region of the load displacement cure (e.g., below $\lambda = 0.15$), respectively. Tables A.7 and A.8 list the 40 most important and 40 least important variables in the yielding region of the load displacement cure (e.g., above $\lambda = 0.15$), respectively. The variables are all ranked in decreasing order of the magnitude of their importance measures $\partial u / \partial x_i \sigma_i$.

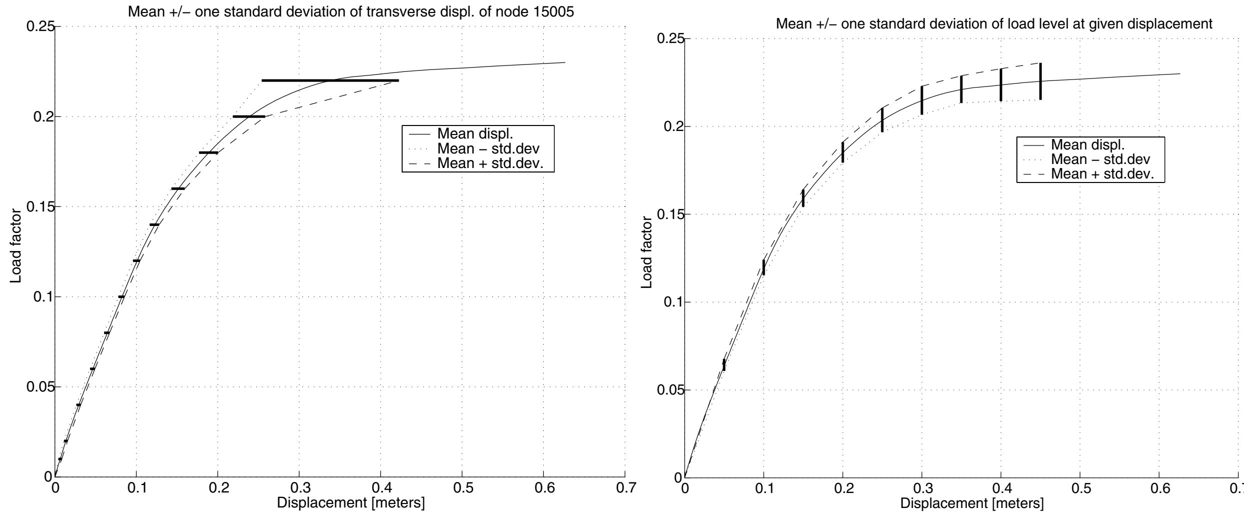

Fig. 6.2 Results from FOSM analysis; conditional mean and mean ± standard deviation for (a) u given λ (left) and (b) λ given u (right)

In the initial region of the load-displacement curve, the stiffness of the soil springs is identified as the most important variable. The stiffness and cross-sectional geometry of the horizontal elastic elements close to the bent with node 15005 also rank high. Nodal coordinates in the y-direction for the nodes of this bent are among the top 25 most important variables. This is remarkable, since the assumed standard deviation is only 1.27 cm. Properties f_c' and ε_{c0} of the cover concrete of the plastic hinges and the elastic modulus E of the elastic regions of elements 151 and 152 also rank among the 40 most important parameters. Among the least important parameters in this region of the load-displacement curve are all the parameters related to material yielding, such as σ_y, the hardening parameters, f_{cu} and ε_{cu}.

In the yielding region of the load-displacement curve, the yield strength parameters of both reinforcing steel and core/cover concrete of the columns are most important, followed by the vertical and horizontal soil spring stiffnesses. y- and z-direction coordinates of several nodes also rank high. Properties of the elastic horizontal elements seem rather unimportant, though properties of element 153 rank as the 36th and 38th most important random variables in the model. The observed high importance of the nodal coordinates may seem counter intuitive. However, this phenomenon can be explained in terms of the well known $P-\Delta$ effect: In the presence of large gravity loads, any deviation in the nodal coordinates produces additional bending moment in the columns, thus resulting in a larger lateral displacement.

Next, we consider reliability pushover analysis. The following four limit-state functions are considered:

$$g_1(\mathbf{x}) = u_0 - u(\mathbf{x}, \lambda) \tag{6.4}$$

$$g_2(\mathbf{x}) = \lambda_0 - \lambda(\mathbf{x}, u) \tag{6.5}$$

$$g_3(\mathbf{x}) = u_0 - u_{\text{at 20\% tangent}}(\mathbf{x}) \tag{6.6}$$

$$g_4(\mathbf{x}) = \lambda_0 - \lambda_{\text{at 20\% tangent}}(\mathbf{x}) \tag{6.7}$$

In the above, u_0 and λ_0 are thresholds, while all other variables are as defined before. Repeated reliability analysis while varying u_0 or λ_0 allows us to compute the complementary cumulative distribution function (CCDF) of each of the response quantities. Furthermore, probability sensitivities with respect to the these thresholds provide us the probability density functions (PDF).

For the limit-state function in Equation (6.4), the computed CCDF and PDF of $u(\mathbf{x}, \lambda)$ for $\lambda = 0.20$ are plotted in Figure 6.3. Three cases are considered: (a) reliability analysis including the uncertainty in only the 10 most important random variables in Table A.7, (b) analysis with the top 100 most important random variables, and (c) analysis with all 320 random variables. It is clear that the analysis with the top 100 most important random variables produces results that are practically identical to those obtained when all 320 random variables are considered. Based on this finding, subsequent reliability analysis is carried out using only the top 100 most important variables with the remaining ones being substituted with their mean values. This simplification greatly reduces the required computational effort.

Figure 6.4 shows the computed CCDF and PDF of $\lambda(\mathbf{x}, u)$ for $u = 0.30\,\text{m}$, obtained by repeated reliability analyses with the limit-state function in Equation (6.5). Due to the asymptotic nature of FORM, these distribution estimates are more accurate in the tail regions (which are of engineering interest) than in the central regions. Comparison of the means and standard deviations indicated in the PDFs in Figures 6.3 and 6.4 with the corresponding second-moment estimates in Figures 6.2a and 6.2b, respectively, reveals good consistency between the two sets of approximations.

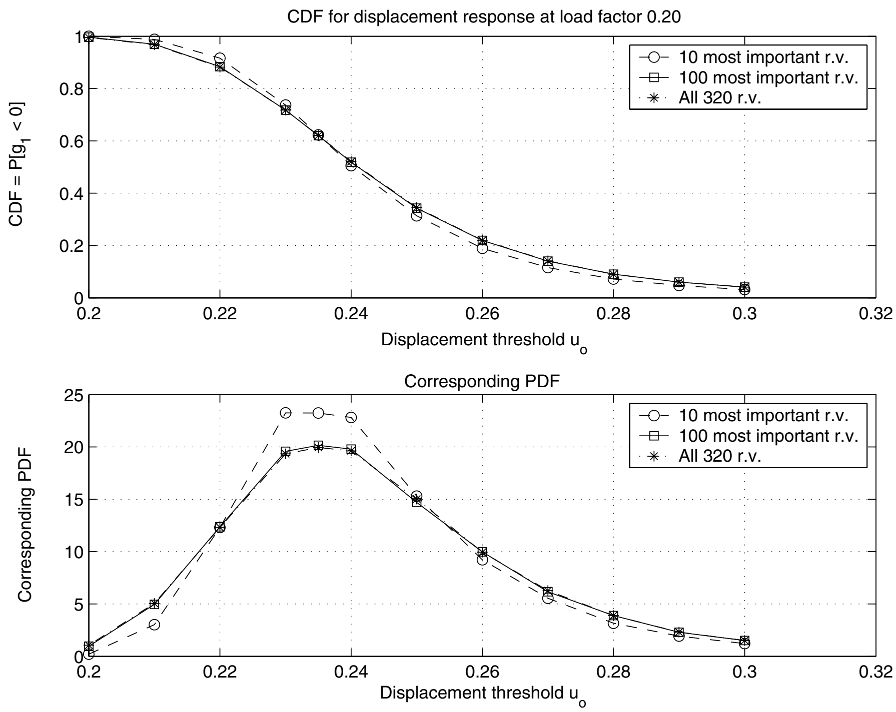

Fig. 6.3 Probability distribution for displacement response at load factor 0.20, obtained by a series of FORM reliability analyses of performance function g_1

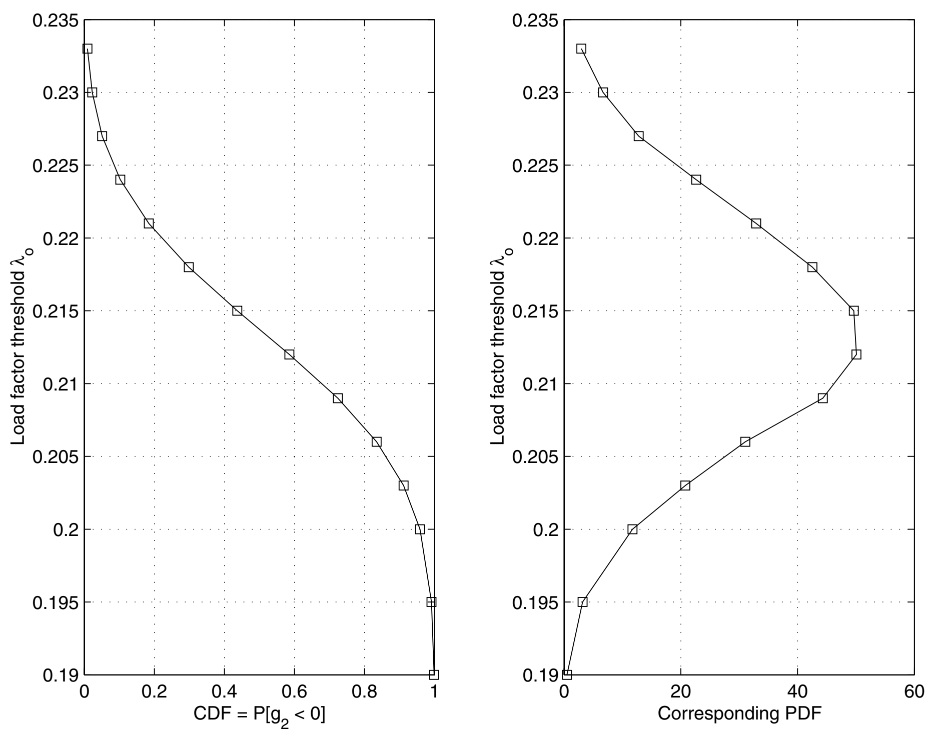

Fig. 6.4 Probability distribution for load factor level at displacement 0.3 m, obtained by a series of FORM reliability analyses of performance function g_2

The limit-state function in Equations (6.6)–(6.7) pose more challenging problems. Since the tangent of the load-displacement curve enters the expressions, the reliability analysis involves second derivatives. The finite difference method is used to compute these derivatives. Initial attempts with these limit-state functions did not lead to convergence of the algorithm. The reason is the jagged behavior of the tangent, as can be seen in Figure 6.5b (solid line). This jaggedness is arising from the many sudden changes in the stiffness due to yielding of individual material fibers. As a remedy for this problem, smooth material models have been developed in OpenSees. The original bilinear steel material model is replaced with a smooth version that exhibits a smooth transition between the elastic and plastic material states. See Haukaas and Der Kiureghian (2004) for the details of the smooth model. The effects of the smoothing on the load-displacement and tangent curves are shown in Figure 6.5. It is seen that, while the load-displacement response has not changed significantly, the tangent curve has become smoother. Reliability analysis with the smoothed material model easily converges. Figures 6.6 and 6.7 show the CCDF and PDF curves for the responses $u_{\text{at 20\% tangent}}(\mathbf{x})$ and $\lambda_{\text{at 20\% tangent}}(\mathbf{x})$, respectively.

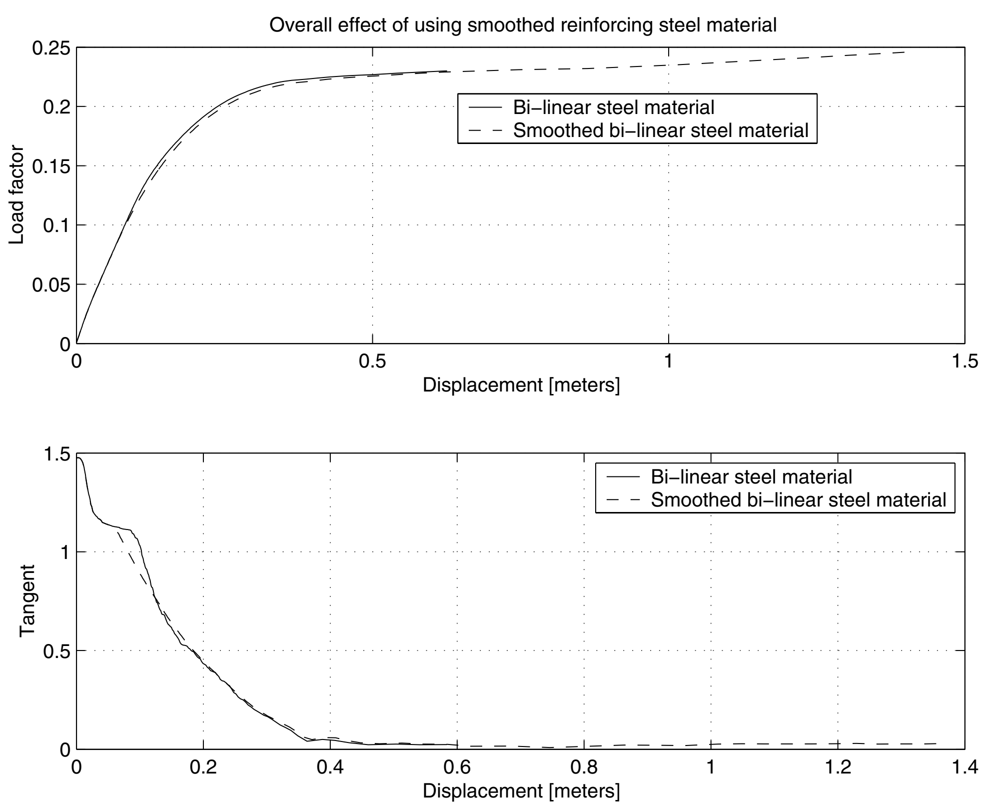

Fig. 6.5 (a) Load-displacement curve and (b) tangent of load-displacement curve

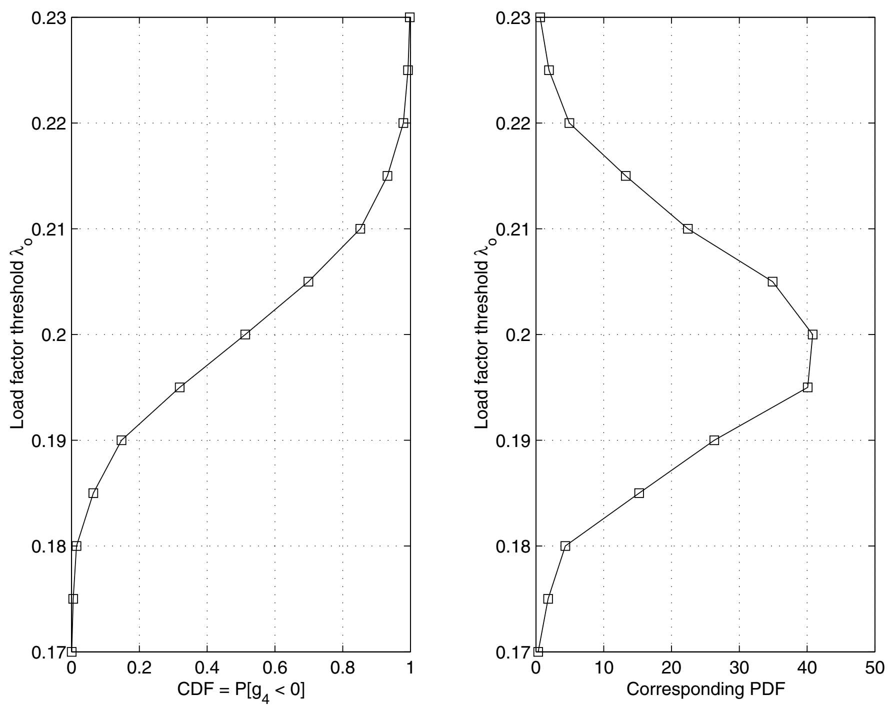

Fig. 6.6 Probability distribution for displacement at 20% of elastic tangent, obtained by a series of FORM reliability analyses of performance function g_3

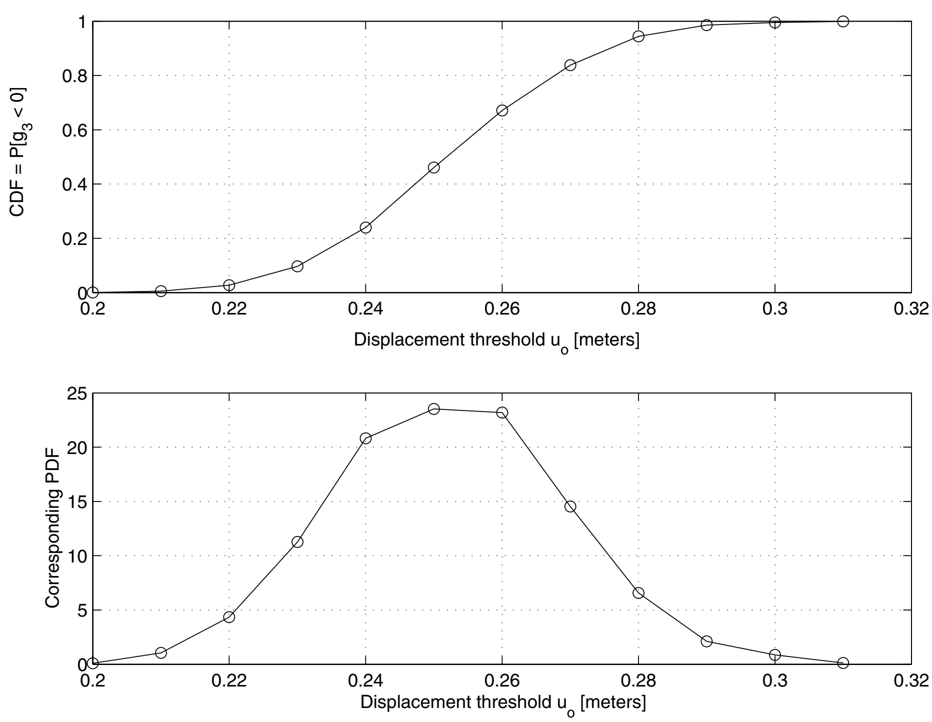

Fig. 6.7 Probability distribution for load factor at 20% of elastic tangent, obtained by a series of FORM reliability analyses of performance g_4

As a means of examining the accuracy of the above results, importance sampling centered at the design point is carried out for the limit-state function $g_1(\mathbf{x})$ for $\lambda = 0.20$ and $u_0 = 0.35$ m. A sample of 1000 simulations produces the failure probability (probability that $u(\mathbf{x},0.20)$ will exceed the level $u_0 = 0.35$ m) estimate $\hat{p}_f = 0.0107$ with 5.5% coefficient of variation. The FORM approximation, $p_{f,\mathrm{FORM}} = 0.0119$, compares favorably with this "exact" estimate. It is noted that a Monte Carlo estimate with 5% COV would require approximately 34,000 simulations.

6.3.2 Probabilistic Dynamic Analysis

OpenSees includes several options for stochastic dynamic analysis. One option is to compute the mean rate of occurrence of events such as $\{g(\mathbf{x}, \mathbf{y}(t)) \leq 0\}$, where $\mathbf{y}(t)$ denotes a vector of stochastic processes, e.g., components of the ground motion, which are represented in a discrete form in terms of a finite number of random variables. This problem can be solved as a parallel system reliability problem (see Der Kiureghian 2000). With the current implementations in OpenSees, unfortunately this option requires a very long computational time. Hence, at the present time this application is practically restricted to linear structures. Ongoing work is aimed at improving the applicability of this method to nonlinear problems.

If the limit-state function exhibits a monotonically decreasing behavior with time, then time-invariant FORM analysis can be used to solve the probabilistic dynamic problem. As an application to the I-880 testbed, consider the limit-state function:

$$g(\mathbf{x}) = E_0 - E_h(\mathbf{x}) \tag{6.8}$$

where $E_h(\mathbf{x})$ is a (nonnegative) cumulative damage measure, such as the hysteretic energy dissipated by an element during a ground motion, and E_0 is an acceptable threshold. Since $E_h(\mathbf{x})$ is a cumulative measure, the above limit-state function monotonically decays with time. Therefore, the probability of failure can be computed at the end of the excitation period. For this application we have selected $E_h(\mathbf{x})$ as the cumulative hysteretic energy dissipated by the reinforcing bar of a particular column in the bridge model. We also select $E_0 = 22\times10^6\,\mathrm{N/m}^2$. The structure is subjected to the ground motion record at the Gilroy historic station during the 1989 Loma Prieta earthquake. Significant inelastic deformation occurs in the reinforcing bar.

Now, FORM analysis with the limit-state function in Equation (6.13) and the top 20 most important random variables is carried out to compute the failure probability. The result is $p_{f,\text{FORM}} = 0.00167$, indicating a small probability that the hysteretic energy dissipated by the selected reinforcing bar will exceed the specified threshold.

6.4 CONCLUDING REMARKS

Given the scope of the testbed report, only selected aspects of the reliability tools in OpenSees could be presented here. The interested reader should consult Haukaas and Der Kiureghian (2004) for details. Furthermore, the reliability tools within OpenSees are continuously being improved and enhanced. We invite researchers within and outside PEER to explore the reliability capabilities of OpenSees. Comments by other users will help us address shortcomings and further develop the tools.

As a final note, we want to stress that the reliability tools implemented in OpenSees allow probabilistic performance-based analysis involving all the measures: *IM*, *EDP*, *DM*, and *DV*. The examples described in this chapter involved performance criteria specified in terms of *EDP*s (limit-state functions Eqs. (6.9)–(6.12)) and *DV*s (limit-state function Eq. (6.13)). Clearly, similar analysis can be performed for any specified criteria in terms of *DV*s.

7 Advancing Performance-Based Seismic Design of Highway Bridges: A Practitioner Perspective

Majid Sarraf and Roy Imbsen
Imbsen & Associates, Sacramento, CA.

This chapter describes the analysis approach and methodologies commonly used in practice followed by a critique of the PEER methodology and its relevance in advancing the state of practice in seismic design of highway bridges.

7.1 CURRENT STATE OF PRACTICE

A general flow diagram of the seismic design process for normal bridges commonly used in practice to meet Caltrans Seismic Design Criteria (SDC 1.3) is shown in Figure 7.1. First, the preliminary sizes of superstructure and substructure members are determined based on service load design requirements in accordance with Caltrans Bridge Design Specifications. This is followed by generating elastic dynamic models for seismic demand estimation using a commercial software tool such as SEISAB, SAP2000, or GTSTRUDL.

For a given site, the design earthquake loading is selected from a series of ARS (Acceleration Response Spectrum) curves provided in SDC 1.3. For the selected design spectrum, multimode spectral analyses are performed based on initial and revised boundary conditions to determined elastic force and displacement demands. Concurrently, the bending capacity and curvature capacity of critical components are determined using commonly available sectional analysis programs (such as XTRACT and X-SECTION). These capacities are used in evaluating limit states and also incorporated into pushover models of substructures of the bridge system.

A pushover analysis of the model is also required by SDC and represents the capacity computation of the structural system and its components. Using SDC criteria, both the global capacity of the structure and local capacity of the critical substructure components are checked against the predicted demands to ensure that a ductile response is achieved. If this check is satisfactory, no major adjustment in the size of the members are needed; however additional seismic detailing requirements must be met before the design is completed. If the capacity/demand requirements are not satisfied, the members are resized and the analyses are repeated. A number of multimode spectral and pushover analyses may be necessary before the design is completed.

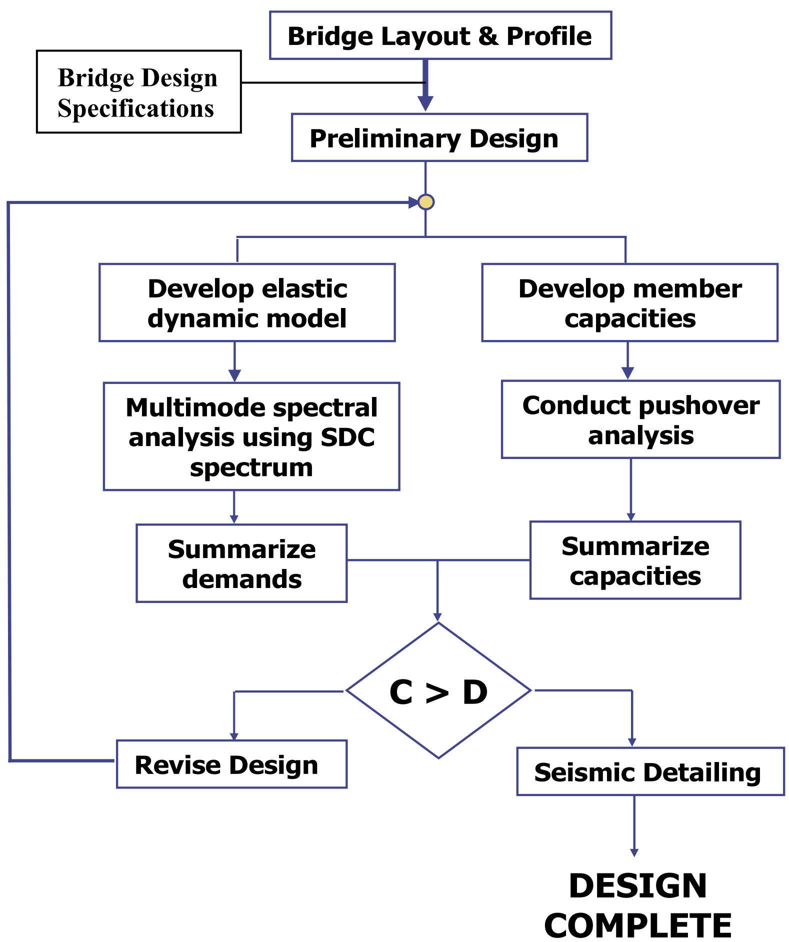

Fig. 7.1 Overview of Caltrans seismic design procedure for highway bridges

CalTrans SDC Version 1.3 is the most current seismic criteria applicable to Ordinary Standard bridges in California. In SDC 1.3, structural components are divided into two categories: ductile, and nonductile- or capacity-protected members. A displacement-based approach is used to evaluate seismic performance of the ductile components where the provided displacement capacities at both local and global levels must be greater than displacement demands. In addition, special seismic details are provided to ensure that the ductility capacity of the component is greater than those assumed in the evaluation process. In the case of nonductile components, the provided nominal capacity of components must be greater than expected force demands to ensure that they are protected against damage resulting from overstrength of ductile components, or maximum probable force demands.

7.2 APPLICATION OF SDC TO I-880 VIADUCT

The subject bridge being conventional with span lengths not exceeding 300 ft is considered an Ordinary Standard Bridge and within the range of applicability of SDC.

7.2.1 Site Geology and Hazard Spectrum

The deterministic approach adopted by SDC requires that the seismic hazard be established based on the ground motions associated with maximum credible earthquakes of nearby active faults. In the case of the I-880, the Hayward fault located approximately 7 km east of the site is considered to produce a maximum credible earthquake with a magnitude M_w= 7.0. The peak rock acceleration obtained from the attenuation relationship (Mualchin and Jones 1992) for a scenario earthquake of magnitude 7.0 at a fault distance of 7.0 km is 0.43g. Given the dense soil profile of the I-880 bridge site, a soil profile of type "D" is assumed for the evaluation. In addition, SDC requires amplification factors due to near-fault effects to be applied to the standard ARS when the distance to the nearby fault is smaller than 15 km. The original ARS and the modified ARS curve incorporating near-fault effects are shown in the Figure 7.2. For comparison with SDC design spectrum, the site-specific spectra generated for the testbed project by Somerville and Collins (2002) are also plotted. It is noted that SDC spectral demands are generally lower than the 10%/50 site-specific spectrum but that the spectral magnitude (including near-fault effects) at the characteristic period of T = 1.2 sec is comparable to the 10%/50 hazard.

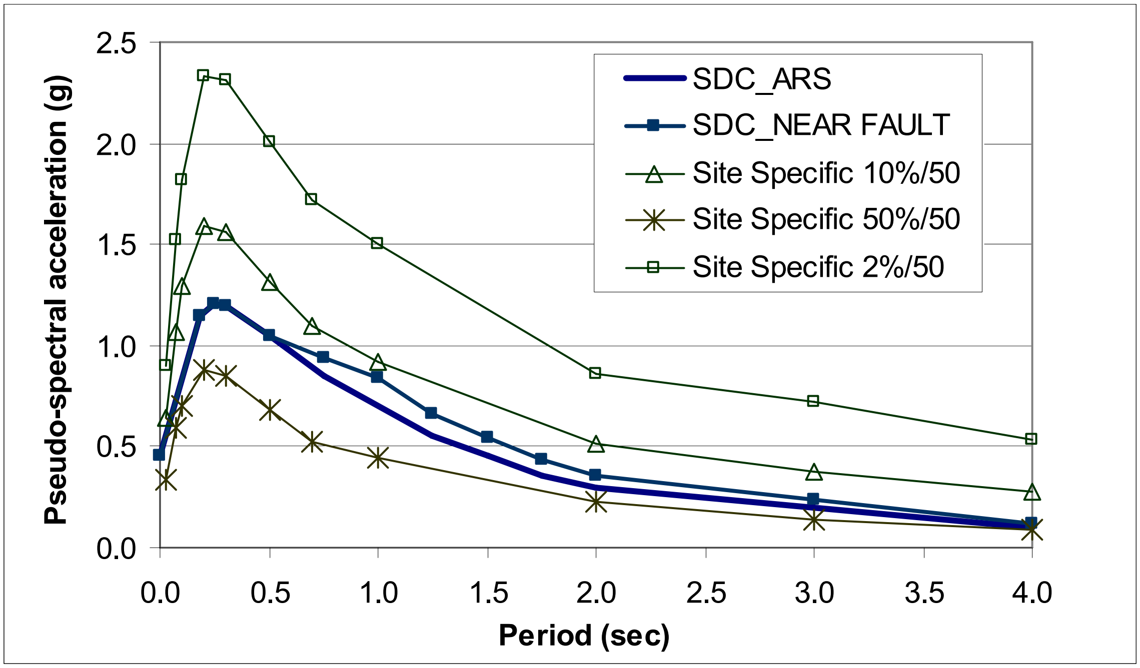

Fig. 7.2 Comparison of SDC design spectrum and site specific spectra used in simulations presented in Chapter 4

7.2.2 Modeling and Evaluation

The global model of the structure consists of three connected spine-like frames representing bents 10–20 and two expansion joints. For elastic dynamic analysis (EDA), gross sectional properties were used for the superstructure members, while cracked sectional properties were used to model bent cap, and columns. Sectional properties of the members are summarized in Table A.9. Distributed masses of the members were assumed as lumped at 1/3 points. Superstructure elements were also included in the model. For the initial run, cable restrainers and shear keys were modeled as linear springs with initial elastic stiffness. It was found that shear keys and vertical restrainers remain elastic, while longitudinal restrainers would yield. Subsequently, a reduced (effective) stiffness was calculated and used for longitudinal restrainers to capture their inelastic behavior and displacements due to yielding. The reduced stiffness property corresponds to the effective stiffness at which the force in the restrainer under the applied loading condition brings the restrainer to its yield limit. A similar approach is used for all yielding elements to ensure that force limit states are not violated.

The following analyses were carried out using SEISAB:

1. Dead load analysis to verify the total assumed mass and distribution.
2. Modal analysis with and without soil-foundation springs to verify assumed boundary conditions, mode shapes, and modal mass participations.
3. Multimode response spectra analysis.

The results of SEISAB modal analysis for two modeling assumptions are summarized in Table 7.1. The final model incorporates soil-foundation elastic springs, expansion joint elements (shear keys and restrainers), and adjustments made to the longitudinal restrainers to account for yielding. Table 7.2 summarizes the initial and reduced stiffness of the hinge restrainers and shear keys at the final stage of the analysis.

Table 7.1 Vibration characteristics of simulation models

Model 1: Fixed-base model				
		Mass Participation (%)		
MODE	**Period**	**Long.**	**Vertical**	**Trans.**
1	0.99	0.031	0.000	16.403
2	0.92	0.079	0.000	32.504
3	0.91	1.076	0.002	53.888
4	0.86	29.250	0.012	55.145
5	0.81	58.244	0.037	55.149
6	0.79	58.551	0.039	66.608
7	0.78	94.356	0.063	66.716
8	0.72	94.377	0.064	84.195
9	0.48	94.402	0.064	92.588
10	0.47	94.540	0.133	92.589
Model 2: Final model with soil-foundation springs				
1	1.26	0.368	0.000	15.075
2	1.24	48.468	0.002	53.053
3	1.18	49.618	0.013	53.532
4	1.14	83.821	0.014	74.053
5	1.04	84.445	0.076	74.053
6	0.86	84.446	4.483	74.139
7	0.81	84.594	4.847	76.686
8	0.80	84.627	7.256	77.075
9	0.69	84.630	25.876	77.079
10	0.67	84.630	45.108	77.079

Multimode spectral analysis of the three-frame spine model subjected to the SDC design spectrum was performed using SEISAB. First, the tension-only models (stand-alone frame models without frame-frame interaction) of the frames were considered to predict the maximum relative displacements between frames. Since the displacements were large enough to cause substantial tension in the restrainers and shear keys, the model was revised to include all shear keys and restrainers. The revised model considered initial elastic stiffness of the components. Where the force demands exceeded the yield capacity of any component, the stiffness of the component was reduced such that the force response of the component would be close to yield limits. The calibration of the force response was achieved by adjusting the stiffness of the components through an iteration process. Such a procedure is commonly employed in practice to incorporate yielding elements in a linear elastic model.

Table 7.2 Restrainer and shear key properties used in final model

	Member	Restrainer	Shear Key	Restrainer
		Longitudinal	Transverse	Vertical
Force (kips)	hinge 13	1488.6	808.3	554.5
	hinge 17	1179.1	1336.1	499.5
Δ_{gap} (in.)	hinge 13	2.25	0.5	-
	hinge 17	1.75	0.5	-
Δ_y (in.)	hinge 13	1.49	0	0.36
	hinge 17	1.37	0	0.36
P_y (kips)	hinge 13	1590	2514	530
	hinge 17	1590	5028	530
K_i (kip/ft)	hinge 13	12808.8	-	17548.8
	hinge 17	13972.8	-	17548.8
K_r (kip/ft)	hinge 13	1676.7	100000	4892.4
	hinge 17	6045.6	100000	2052.0

7.2.3 Pushover Analysis of I-880 Model

Two-dimensional models of each bent in the transverse direction and of each frame in the longitudinal direction are subjected to pushover analysis using CAPP (2004). Idealized bilinear moment-rotation relationships are developed at potential plastic hinge locations (in this case, the ends of each column bent) using EXTRACT. A moment-rotation relationship for a typical plastic hinge is shown in Figure 7.3.

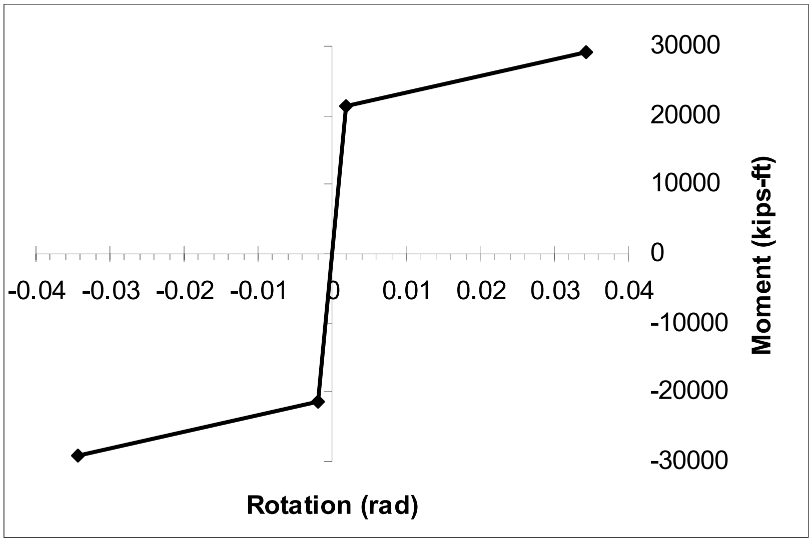

Fig. 7.3 Typical bilinear moment-rotation relationship at potential plastic hinge

The results of pushover analyses in transverse and longitudinal directions for bents 10 to 20 are summarized in Table 7.3. The ultimate displacement corresponds to the failure limit (ultimate moment specified in bilinear moment-rotation relationship) in any column section being reached during the pushover analysis.

Table 7.3 Yield and ultimate displacement capacity of bents

	Transverse		**Longitudinal**	
Bent #	Δ_y (in.)	Δ_u (in.)	Δ_y (in.)	Δ_u (in.)
10	8.6	37.0	3.7	19.4
11	4.0	22.5	3.3	19.4
12	3.8	20.1	3.4	19.4
13	5.9	26.1	3.7	19.4
14	4.0	24.5	5.0	19.2
15	7.0	26.8	4.4	19.2
16	7.2	22.6	4.0	19.2
17	5.9	22.3	2.9	19.2
18	5.4	20.7	3.1	13.3
19	4.9	18.4	3.0	13.3
20	4.0	15.3	2.9	13.3

7.2.4 Dynamic Analysis of I-880 Model

An elastic response spectrum analysis of the I-880 model using the SDC response spectrum (including near-fault effects) indicated that superstructure elements and most expansion joint elements remain elastic. However, longitudinal restrainers would yield in tension at hinge 13 (at the expansion joint between frames 3 and 4). Therefore, the elastic stiffness of the springs representing the longitudinal restrainers was calibrated as discussed earlier by reducing their effective stiffness. The final simulation model used in the analysis does not violate the capacity limits in any element. The following observations are made following the elastic dynamic analysis:

- Columns will be subjected to large bending moments that cause plastic hinging;
- The cable restrainers used at the expansion joints would yield in tension;
- Vertical restrainers will remain elastic;
- All shear keys will remain elastic; and
- Bearings will slide but no unseating is expected.

A summary of force and displacement demands in the substructure elements is provided in Table A.10.

7.2.5 Assessment of Performance

The assessment of seismic performance of the viaduct is made by checking the following:

- column ductility demands
- joint shear and bending capacity of bent cap
- shear and bending capacity of footings
- axial uplift, bending and shear capacity of piles
- bending capacity of superstructure elements
- restrainer capacity and seat width limits at expansion joints

Columns: Based on the computed displacement demands (Table A.10) and yield displacements obtained from pushover analysis, column ductility demands were calculated and plotted as shown in Figure 7.4. SDC 1.3 limits the ductility of a column in a multicolumn bent to 5. In this case, the maximum ductility is 4.3 and occurs at bent 10, and therefore, satisfies the SDC ductility limit.

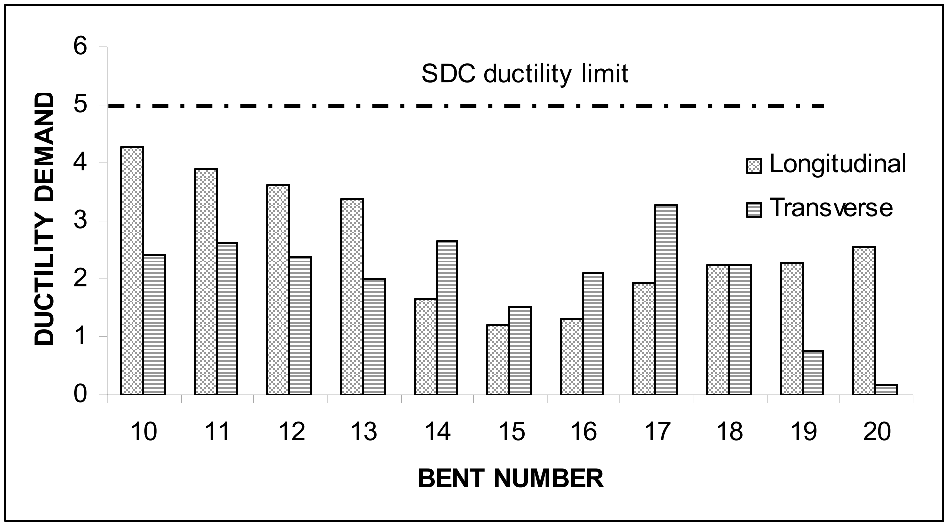

Fig. 7.4 Ductility demands on column elements

Superstructure elements: According to SDC, the superstructure girders are considered to be capacity-protected components; thus during an extreme event, plastic hinging may be expected only in the substructure while the superstructure remains essentially elastic. Thus, the longitudinal superstructure moments due to permanent loads (dead load and prestressing forces) combined with the overstrength moment of the column resulting from potential plastic hinging should not exceed the nominal bending capacity of superstructure. Table 7.4 summarizes the moment demands and nominal capacity of superstructure girders. It is evident that the superstructure girder capacities are in conformance with SDC requirements.

Similarly, the bent cap is a considered a capacity-protected member. The nominal moment capacity of the bent in the transverse direction should not be exceeded. A check of the joint shear capacity check is also performed to ensure that a premature shear failure of the column to bent cap joint is prevented. Typically, the shear stresses in the joint region producing principal tensile and compressive stresses should not exceed $12\sqrt{f_c'}$ and $0.5 f_c'$, respectively. All checks satisfied SDC requirements indicating satisfactory performance.

Table 7.4 Superstructure moment capacity checks

Bent	M_D	M_{PS}	M_O	M_{EQ}	M_{D1}	M_{D2}	M_n^+	M_n^-	Super-Structure capacity
14Rt	21377	11894	41460	20730	30213	-11247	23430	35260	O.K.
15Lt	18592	12572	34240	17120	23140	-11100	23430	35260	O.K.
15Rt	19702	11755	34240	17120	25067	-9173	23430	35260	O.K.
16Lt	19529	12757	34855	17428	24200	-10655	23430	35260	O.K.
16Rt	21895	14905	34855	17428	24418	-10438	23430	35260	O.K.
17Lt	18979	6149	36475	18238	31068	-5408	23430	35260	O.K.

Notes: Units are k-ft
M_D = Dead load moment; M_{PS} = Moment due to prestress; M_O = Moment considering overstrength; M_{EQ} = Earthquake moment; M_{D1} and M_{D2} = Moment demand; M_n^+ and M_n^- = Nominal moment capacities.

The expansion joints each move 2.25 in. and 1.75 in., respectively, in the longitudinal direction. SDC requires the following minimum seat width:

$$\Delta_{min} = (\Delta_{eq} + \Delta_{temp} + \Delta_{cs} + \Delta_{ps} + 4.0)\ in. \tag{7.1}$$

Δ_{eq} = movement due to earthquake loads

Δ_{temp} = movement due to temperature

Δ_{cs} = movement due to creep and shrinkage

Δ_{ps} = movement due to prestressing forces

The minimum required seat-width in this case is 10.75 in. which is smaller than the provided seat width of 36 in. Therefore, no unseating of the superstructure is expected.

Foundation: To prevent premature joint shear or bending failure of the footings, SDC requires that the footings be designed as capacity-protected components for overstrength moment resulting from plastic hinging at the base of the column. In this case, both joint shear and flexural capacity of the footings were found to be adequate. Additionally, the axial uplift and compressive capacity of each pile should not be exceeded when the pile group is subjected to combined dead load and overstrength moment capacity of the column. The lateral shear and bending capacity of the piles against overstrength moment and associated plastic shear of the column also needs to be checked. In all cases, SDC requirements were satisfied.

7.3 PRACTITIONER APPRAISAL OF PEER METHODOLOGY

The PEER methodology is a comprehensive probabilistic approach to seismic assessment of structures for a given seismic hazard considering uncertainties in the loading and the expected performance of critical components. In this section, the application of the PEER methodology, as outlined in Chapters 1–6, in routine bridge design practice is examined. We begin with a comparison of the estimated seismic demands in the bents followed by an appraisal of the general PEER approach for performance-based seismic evaluation of bridge structures.

7.3.1 Comparison of PEER Demand Estimates vs. State of Practice

The primary parameter used in the PEER evaluation is the probable deformation demands in the columns. In the PEER methodology, tangential drift was used as the *EDP*. In the analysis performed by Imbsen and Associates, the monitored *EDP* was the relative column drift (between the base and deck level). The practitioner approach involved a linear elastic multimode response spectrum analysis using a single Caltrans-specified ARS curve. The PEER evaluation was based on ten simulations at each of three hazard levels. Recalling that the site-specific hazard for 10% in 50 years was closest to the ARS curve used in the multimode analysis, the maximum response displacements obtained from the linear response spectrum analysis are compared to the PEER response statistics for the 10%/50 events. Shown in Figure 7.5 are the results of all ten PEER simulations along with the mean *EDP* measures. Note that the deformations shown in the figure correspond to the column drift (which is approximately twice the tangential drift, since the inflection point typically occurs around midheight). The spectral magnitude at T=1.2 sec for the ARS curve was approximately 0.66g while that for the site-specific spectrum used in the PEER evaluation was 0.84g. Hence, the estimated demands using the ARS curve were scaled by a factor of 1.27 to simulate elastic demands corresponding to the same spectral magnitude as the PEER spectra. The comparative demands are displayed in Figure 7.5.

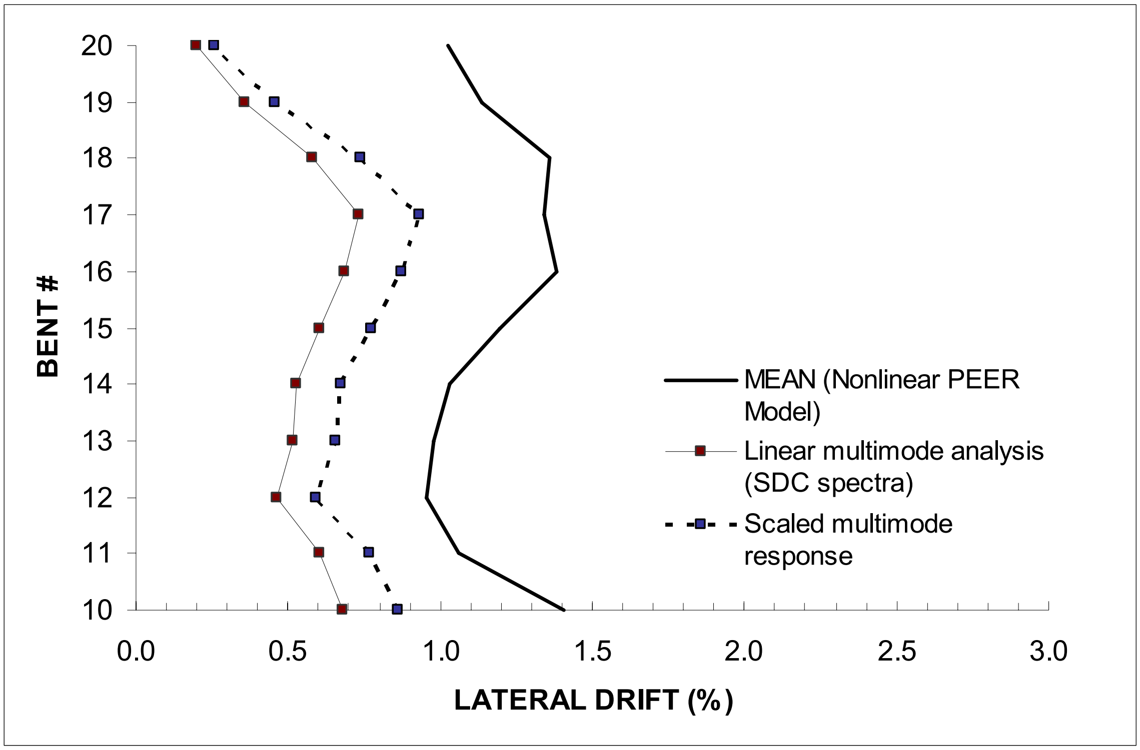

Fig. 7.5 Comparison of deformation demands from PEER evaluation with demands determined using typical procedure in modern practice

The mean demands estimated by the PEER nonlinear model vary considerably from the demands predicted by the multimode analysis. This is most likely due to variations in the frequency content of the ground motions resulting from scaling the original records to match the hazard spectrum at a particular period.

7.3.2 Hazard Definition and Ground Motions

The seismic loading in the PEER approach is characterized by an intensity measure which is consistent with the overall evaluation for a probabilistic definition of the hazard. The use of peak ground acceleration and spectral acceleration at a characteristic period are generally used in practice and are appropriate parameters for characterizing the intensity measure. In the PEER methodology used in this study, various ground motions are amplitude-scaled at a characteristic period of the structure. However, at other periods, the scatter resulting from variation in frequency content of these ground motions result in spectral accelerations significantly different from those of target hazard spectrum. Thus, a uniform approach in choosing the ground motions and scaling process is needed to reduce scatter in predicted response. In the case of bridges having a highly nonlinear response, the concept of a characteristic period would no longer be valid. Thus, it may be more appropriate to use alternative scaling procedures as suggested below:

- A combination of frequency scaling and amplitude scaling, such that resulting spectral accelerations over a larger range of period would more closely match the hazard spectra.
- Use of more than just a single period. It is important to distinguish between longitudinal, and transverse modes, as well as some higher modes with significant modal mass participations.
- Defining some other type of characteristic period based on equivalent effective stiffness of the nonlinear structure, or using amplitude scaling to match the inelastic target hazard spectrum for a given ductility (based on preliminary analysis).

Other alternatives include the choice of a different intensity measure or the use of spectrum-compatible artificially simulated ground motions.

7.3.3 Engineering Demand Parameters

In order to establish a statistical distribution of the demand, it is necessary to carry out a set of simulations either by varying the ground motion or introducing variations in the material behavior. Since engineering practice currently relies on elastic dynamic analysis, it may be reasonable to assume that the response from a multimode analysis represents the mean demand and to then incorporate an acceptable standard deviation to generate the required fragility functions of demand versus intensity measure.

Engineering demand parameters in the form of a vector of *EDP*s as suggested in the general PEER methodology is too broad and ambiguous for practical use. In practice, demand parameters are typically broken into two categories: deformation or displacement quantities for yielding components, and force quantities for essentially elastic or brittle components. Since the approach should encompass the performance of all structural components regardless of whether they are force or deformation controlled, it is essential to clearly identify a few demand parameters such as drift and associated axial loads that can be correlated to damage measures.

7.3.4 Damage Measures and Decision Variables

In current seismic design practice, damage measures are typically established through a deterministic approach using prescribed ductility limits of the element. The PEER methodology allows for consideration of variations in material and element properties and variations in the response of the structure from uncertainties in modeling and seismic input. Such an approach is logical and consistent with assessing the probabilistic response of critical components of the structure. However, there is insufficient data to calibrate damage with the response of numerous critical components of the bridge system such as restrainers, shear keys, abutments, and foundation elements. Research is needed to develop probabilistic damage measures as a function of the seismic demand in all critical components of the system.

In the case of bridge structures, the economic impact of bridge damage is best measured in terms of repair and/or replacement cost and the likelihood of closing the bridge. The procedure presented in this study to develop fragility curves from a survey of bridge inspectors is useful but not representative of the actual decision that "should" be made. In this context, it would again be useful to develop prescriptive guidelines for bridge inspectors so that decisions are made in a rational manner.

7.3.5 Value of Methodology for Assessment of I-880 Viaduct

The modeling and simulations of the I-880 viaduct using OpenSees is essential to capture the nonlinear dynamic response of the system and its components. It is recognized that for this particular structure the foundations have sufficient stiffness and strength, and the effect of uncertainties in foundation impedances is limited; thus use of linear springs with constant stiffness for modeling foundation-soil interaction appears to be suitable and practical for this bridge. The reliability analyses carried out in this study was limited to variations in material behavior. However, considering more variables such as foundation soil stiffness, and ground motion characteristics, would have resulted in a more comprehensive seismic assessment.

The value of the methodology in seismic assessment of the I-880 is its capacity to predict the damage, such as spalling and bar buckling, to structural components in a probabilistic manner and to offer meaningful and tangible performance measures to practitioners. Likewise, the decision variables that are defined as a function of the damage state will be very helpful to transportation authorities in making economical decisions. For example, the probability of closure as a function of intensity measure as presented in the assessment is extremely useful to bridge authorities in providing awareness about the degree of seismic risk involved and the impact of the closure of the bridge on the economy for this critical structure.

7.3.6 Broader Impact

The PEER methodology is a very comprehensive performance-based approach applicable to all types of existing and new bridges. Since it is a probabilistic-based approach, it allows a designer to establish a meaningful and logical process to correlate the extent of earthquake damage to probable hazard, and can effectively help bring together owners and public agencies to assess cost-benefit ratios to retrofit, replace, and repair bridges through decision variables.

Though the proposed approach can be used for any type of bridge, the vulnerability and the damage potential are much greater in existing bridges than in newly designed and constructed bridges conforming to the most current seismic design provisions. Existing bridges are usually the subject of seismic evaluation for possible retrofit, or known risk of damage and associated post-earthquake repairs. In existing bridges, many vulnerable components could contribute to the risk of collapse, full closure, or spread of damage, requiring extensive post-earthquake repairs. In such cases, bridge owners often consider a shorter life span for the bridge requiring a smaller exposure to damage from a seismic event than for new bridges. This is where PEER methodology could be of great value.

A comprehensive and detailed approach is not warranted in the design of ordinary new bridge structures where limited and well-detailed structural components are expected to yield and dominate the structural seismic response. However, PEER methodology can be applied in the seismic design of unconventional bridge structures, or cases where there may be many considerable uncertainties in soil-foundation response such as liquefaction.

7.3.7 Barriers to Implementation

Practicing engineers are well accustomed to deterministic methods in seismic evaluation and to quantifying the seismic response of structures. Analyses are performed with assumed constant material properties throughout. The foundation soil properties and ground motion parameters, however, are known to be the least certain properties used in an analysis. Often a number of different analyses are performed to establish upper- and lower-bound values for such properties, when their impact on the seismic performance is expected to be significant. The main advantage of the PEER methodology is to account for all uncertainties throughout the seismic assessment and structural performance using a probabilistic approach. However, a number of barriers still exist which may inhibit practitioners from effective and full adaptation of the PEER approach. Some of the perceived barriers to implementing the methodology are itemized below:

1. **Familiarity with statistical methods in analyses:** Structural engineers and designers rarely deal with probabilistic quantities. For example, ground motions are typically provided by geotechnical engineers for a given hazard which is recommended by a panel of experts. Reliability analyses are often performed by the expert independently and transformed into load and reduction factors which are then embodied into prescriptive design codes. Similarly though engineers are familiar with damage measures, they tend to use deterministic limits associated with ductility and or plastic rotation capacity. Introducing probabilistic methods mean that engineers need to be trained to use and understand the process without ambiguity. Engineers will rarely adopt a procedure that they cannot properly and fully comprehend. Even if the probabilistic tools are offered as a "black-box" for post-processing, adequate training and reference material must be made available to render the process as transparent as possible.
2. **Modeling and available analytical tools:** One of the most useful aspects of the PEER methodology is correlating damage measures as functions of engineering demand parameters. This is best achieved through accurate representation of dynamic response of using nonlinear analyses that require elaborate modeling techniques. Practitioners are generally experienced in elastic dynamic analyses; however only a small percentage would perform nonlinear analyses. Since this requires advanced knowledge of structural analysis and modeling of nonlinear material behavior, such tasks are subcontracted to specialists and researchers. If the methodology is to be used routinely in engineering practice, the process must be simplified to the extent that design offices should not have to rely on expert knowledge to carry out the evaluation. For example, Imbsen & Associates, an industry leader in developing and using nonlinear analysis for seismic design and evaluation, often face users with different backgrounds who are not comfortable with the use of nonlinear elements and pushover analysis.
3. **Standardization of PEER's methodology:** Practicing engineers are always required to perform analysis and design that conforms to the provisions of a specification or

prescribed design criteria, such as AASHTO and Caltrans SDC. The importance of such standards is two-fold: uniformity in engineering analysis and design of structures, and degree of liability that engineers assume in performing analysis and design. The PEER methodology offers a very comprehensive yet to a great extent a liberal approach in the selection of variables and modeling of uncertainties, and these choices can lead to inconsistencies from one application to the next and to variations in implementation from one engineering firm to another. For example, in carrying out a fully nonlinear time-history analysis, there are many choices for nonlinear elements: lumped versus distributed plasticity, and hardening and stiffness degradation properties for various conditions. In some cases, research may be warranted to properly select and incorporate a nonlinear element for a particular application, something that the time and priority of engineering work does not accommodate, and the assumed liability for their skill would be grave.

Thus it is important to develop simple prescriptive guidelines for the selection of all elements of the PEER methodology: from the choice of intensity measure to the selection of engineering demands parameters, damage measures and decision variables.

7.3.8 Possible Steps to Mitigate Barriers

Numerous examples of scientific theories and engineering innovation exist that were once limited in application and only appreciated by academicians, but that have been fully adopted over time to be part of routine analysis and design practice today. The PEER performance-based framework has the potential to evolve and be fully adopted in practice. The following steps may help mitigate some of the barriers to implementing the PEER framework for performance-based seismic engineering, thus paving the way for practitioners to embrace the methodology.

- It is imperative that OpenSees evolve into a user-friendly interactive tool with graphical interfaces and built-in reliability and probabilistic tools so that engineers can use the program with the same comfort afforded by commercial software such as SEISAB and SAP2000.
- Efforts should continue to address research needs in calibrating damage measures and decision variables to demand parameters through collaboration with industry partners and practitioners.

- Workshops and hands-on training sessions should be offered jointly by practitioners and academics.
- A series of easy-to-follow examples for seismic assessment of bridges of various configurations should be developed, with the opportunity to review and incorporate comments from practitioners.
- Guidelines for the scope and application of the methodology (modeling techniques and use of nonlinear elements, engineering demand parameters) should be developed in close partnership with industry.
- Definitions and nomenclature should be standardized for terms such as decision variables, damage measures, and intensity measures (including procedures for ground motion selection and scaling) based on consensus among researchers, transportation authorities, and bridge owners.

REFERENCES

Abrahamson, N. A., and W. J. Silva. 1997. Empirical response spectral attenuation relations for shallow crustal earthquakes. *Seismological Research Letters* 68: 94–127.

Ang, A. H-S., and W-H. Tang. 1975. *Probability concepts in engineering planning and design, vol. I - basic principles*. John Wiley & Sons, New York.

Baker, J. W., and C. A. Cornell. 2004. Choice of a vector of ground motion intensity measures for seismic demand hazard analysis. Paper No. 3384, *Proc. 13th World Conference on Earthquake Engineering,* Vancouver, Canada.

Berry, M. P. 2003. Estimating flexural damage in reinforced concrete columns. Master's thesis, Dept. of Civil and Environmental Engineering, University of Washington, Seattle.

Berry, M. P., and M. O. Eberhard. 2003. *Performance models for flexural damage in reinforced concrete columns.* Pacific Earthquake Engineering Research Center Report 2003/18, University of California, Berkeley, California.

Berry, M. P., M. Parrish, and M. O. Eberhard. 2004. *PEER structural performance database user's manual.* Pacific Earthquake Engineering Research Center. University of California, Berkeley, California. http://nisee.berkeley.edu/spd/performance_database_manual_1-0.pdf

Camarillo, Haili R. 2003. Evaluation of shear strength methodologies for reinforced concrete columns. Master's thesis, Department of Civil and Environmental Engineering, University of Washington, Seattle.

CAPP 2004. Capacity Analysis Pushover Program. www.imbsen.com/capp.htm.

Cornell C. A. 1996. Calculating building seismic performance reliability; a basis for multi-level design norms 1996. *Proc. Eleventh Conf. on Earthquake Engineering*, Acapulco, Mexico.

Cornell, C. A., F. Jalayer, R. O. Hamburger, and D. A. Foutch. 2002. Probabilistic basis for 2000 SAC Federal Emergency Management Agency steel moment frame guidelines. *ASCE J. Structural Engineering* 128(4): 526–33.

Der Kiureghian, A. 2000. The geometry of random vibrations and solutions by FORM and SORM. *Probab. Engrg. Mech*. 15(1): 81–90.

Eberhard, M. O. 2000. Consequences of bridge damage on functionality. *Proceedings, PEER Invitational Workshop on Performance-Based Engineering Concepts for Bridges*, Palo Alto, California.

FEMA-350. 2000. Recommended seismic design criteria for new steel moment-frame buildings. developed by the SAC Joint Venture for the Federal Emergency Management Agency, Washington D.C.

FEMA-356. 2000. Prestandard and commentary for the seismic rehabilitation of buildings. Federal Emergency Management Agency, Washington D.C.

Haukaas, T., and A. Der Kiureghian. 2004. *Finite element reliability and sensitivity methods for performance-based engineering.* Report No. PEER 2003/14, Pacific Earthquake Engineering Research Center, University of California, Berkeley.

Kennedy, R. P., S. A. Short. 1994. Basis for seismic provisions of DOE-STD-1020 1994. *UCRL-CR-111478*, Prepared for U.S. Department of Energy, Washington, D.C.

Kunnath, S., A. El-Bahy, A. Taylor, and W. Stone. 1997. *Cumulative seismic damage of reinforced concrete bridge piers.* Technical Report NCEER-97-0006, National Center for Earthquake Engineering Research, Buffalo, New York.

Lehman, D. E., S. E. Gookin, A. M. Nacamuli, and J. P. Moehle. 2001. Repair of earthquake-damaged bridge columns. *ACI Struct. J.* 98(2): 233–42.

Liu, P-L., and A. Der Kiureghian. 1986. Multivariate distribution models with prescribed marginals and covariances. *Probab. Engrg. Mech*. 1(2): 105–12.

Miranda, E., and H. Aslani. 2003. *Probabilistic response assessment for building-specific loss estimation*. Report 2003/03, Pacific Earthquake Engineering Research Center, University of California, Berkeley, CA.

Mualchin, L., and A. L. Jones. 1992. *Peak acceleration from maximum credible earthquakes in California.* California Department of Conservation, Division of Mines and Geology Open-File Report 92-01.

Office of Emergency Services. 1995. Vision 2000: Performance based seismic engineering of buildings. Structural Engineers Association of California (SEAOC), Sacramento, CA.

Ranf, R. T., J. Nelson, Z. Price, M. O. Eberhard, and J. F. Stanton. 2003. *Accumulation of flexural damage in lightly reinforced concrete columns.* Pacific Earthquake Engineering Research Center Report PEER-2003, University of California, Berkeley.

SEAOC. 1999. *Conceptual framework for performance-based seismic design.* Structural Engineers Association of California (SEAOC), Sacramento, CA.

Sewell R. T., G. R. Toro, and R. K. McGuire. 1991. *Impact of ground motion characterization on conservatism and variability in seismic risk estimates.* Report NUREG/CR-6467, U.S. Nuclear Regulatory Commission, Washington D.C.

Shome, N., and C. A. Cornell. 1996. Normalization and scaling accelerograms for nonlinear structural analysis. Paper No.243, *Proceedings of the 6th US National Conference on Earthquake Engineering,* Seattle, WA.

Somerville, P., and N. Collins. 2002. *Ground motion time histories for the I880 bridge, Oakland.* Technical report prepared for the PEER testbed project, URS Corporation, Pasadena, CA.

Somerville, P., N. F. Smith, R. W. Graves, and N. A. Abrahamson. 1997. Modification of empirical strong ground motion attenuation relations to include the amplitude and duration effects of rupture directivity. *Seismological Research Letters* 68: 199–222.

Vamvatsikos, D., and C. A. Cornell. 2002. Incremental dynamic analysis. *Earthq. Eng. and Struct. Dyn.* 31(3): 491–514.

Appendix

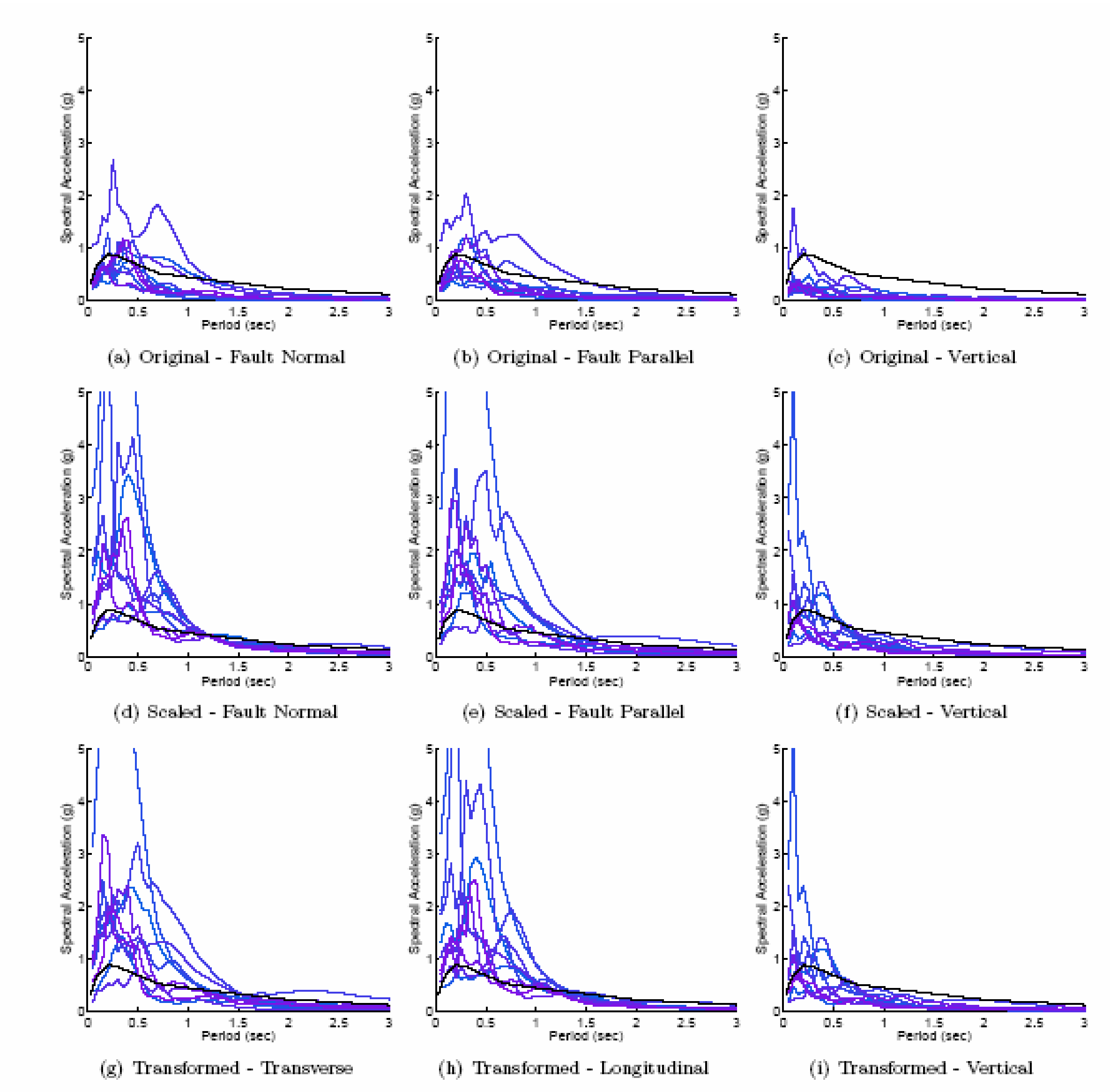

(a) Original - Fault Normal (b) Original - Fault Parallel (c) Original - Vertical

(d) Scaled - Fault Normal (e) Scaled - Fault Parallel (f) Scaled - Vertical

(g) Transformed - Transverse (h) Transformed - Longitudinal (i) Transformed - Vertical

Fig. A.1 Spectra of records corresponding to 50%/50 hazard level

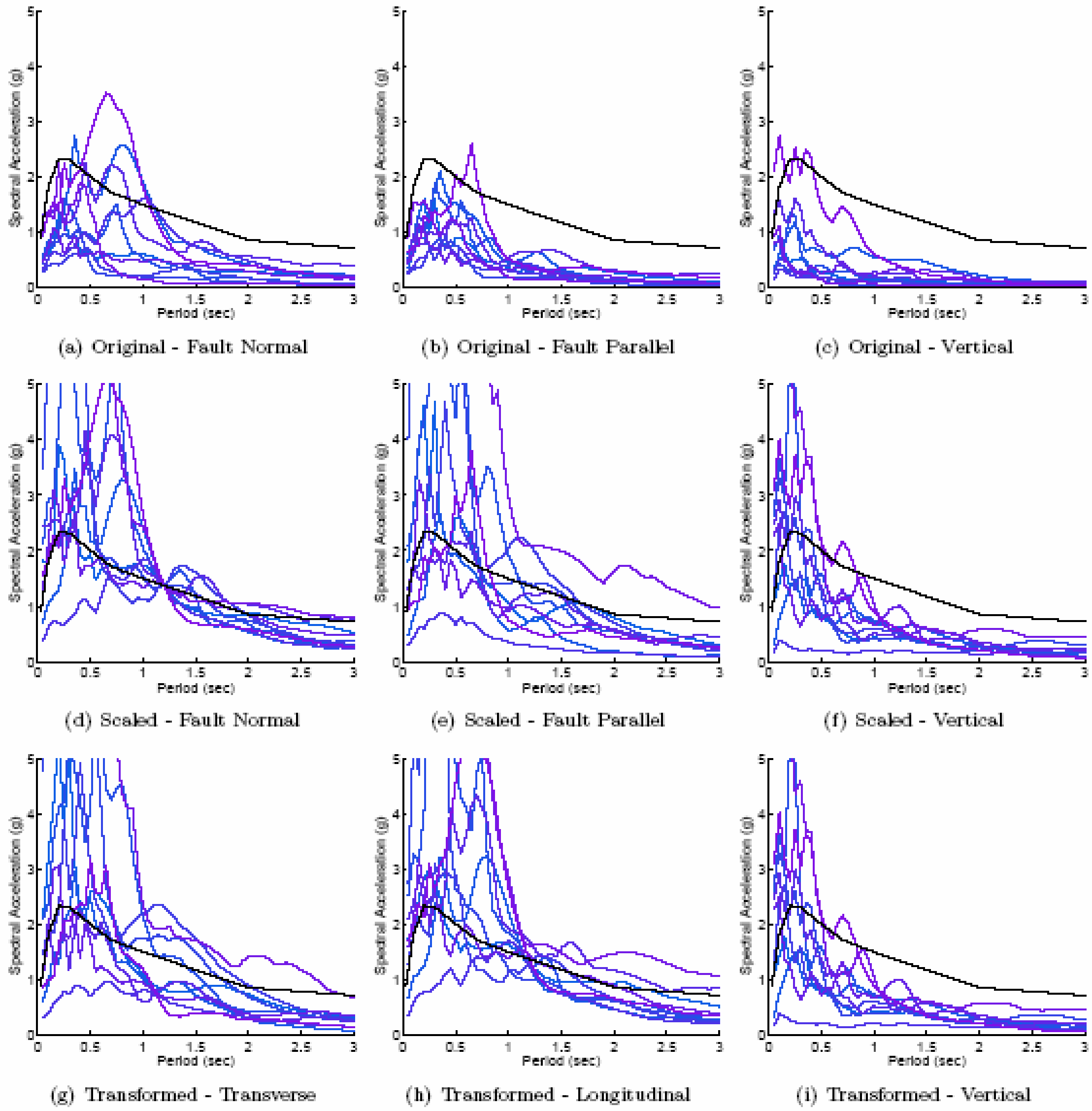

Fig. A.2 Spectra of records corresponding to 2%/50 hazard level

Table A.1 Uncertain parameters in I-880 testbed bridge model, part 1

Parameter	Distribution	Mean	C.o.V.	Correlation
E of reinforcement steel of column hinges (8 r.v.)	Lognormal	$199,948.04\frac{\mathrm{N}}{\mathrm{mm}^2}$	5.0%	0.3
σ_y of reinforcement steel of column hinges (8 r.v.)	Lognormal	$455.05\frac{\mathrm{N}}{\mathrm{mm}^2}$	10.0%	0.3
Second stiffness ratio of reinforcement steel of column hinges (8 r.v.)	Lognormal	0.01	15.0%	0.3
f'_c of core concrete of column hinges (8 r.v.)	-Lognormal	$-46.97\frac{\mathrm{N}}{\mathrm{mm}^2}$	15.0%	0.3
f_{cu} of core concrete of column hinges (8 r.v.)	-Lognormal	$-35.85\frac{\mathrm{N}}{\mathrm{mm}^2}$	15.0%	0.3
ϵ_{c0} of core concrete of column hinges (8 r.v.)	-Lognormal	-0.003	15.0%	0.3
ϵ_{cu} of core concrete of column hinges (8 r.v.)	-Lognormal	-0.02	15.0%	0.3
f'_c of cover concrete of column hinges (8 r.v.)	-Lognormal	$-35.85\frac{\mathrm{N}}{\mathrm{mm}^2}$	15.0%	0.3
ϵ_{c0} of cover concrete of column hinges (8 r.v.)	-Lognormal	-0.002	15.0%	0.3
ϵ_{cu} of cover concrete of column hinges (8 r.v.)	-Lognormal	-0.006	15.0%	0.3
E of linear elastic region of columns (8 r.v.)	Lognormal	$28337.46\frac{\mathrm{N}}{\mathrm{mm}^2}$	5.0%	0.3
A of linear elastic region of columns (8 r.v.)	Lognormal	$6.32\mathrm{m}^2$	5.0%	0.3
I_z of linear elastic region of columns (8 r.v.)	Lognormal	$\frac{2.59\mathrm{m}\,(2.44\mathrm{m})^3}{12}$	5.0%	0.3
I_y of linear elastic region of columns (8 r.v.)	Lognormal	$\frac{2.44\mathrm{m}\,(2.59\mathrm{m})^3}{12}$	5.0%	0.3
G of linear elastic region of columns (8 r.v.)	Lognormal	$0.4 \cdot 28337.46\frac{\mathrm{N}}{\mathrm{mm}^2}$	5.0%	0.3
J of linear elastic region of columns (8 r.v.)	Lognormal	$2.93\mathrm{m}^4$	5.0%	0.3

Table A.2 Uncertain parameters in I-880 testbed bridge model, part 2

Parameter	Distribution	Mean	C.o.V.	Correlation
A of linear elastic transverse beam elements (4 r.v.)	Lognormal	6.65 m^2	5.0%	0.3
E of linear elastic transverse beam elements (4 r.v.)	Lognormal	$28337.46\frac{\mathrm{N}}{\mathrm{mm}^2}$	5.0%	0.3
G of linear elastic transverse beam elements (4 r.v.)	Lognormal	$11376.35\frac{\mathrm{N}}{\mathrm{mm}^2}$	5.0%	0.3
J_x of linear elastic transverse beam elements (4 r.v.)	Lognormal	$0.21\mathrm{m}^4$	5.0%	0.3
I_y of linear elastic transverse beam elements (4 r.v.)	Lognormal	$2.17\mathrm{m}^4$	5.0%	0.3
I_z of linear elastic transverse beam elements (4 r.v.)	Lognormal	$2.17\mathrm{m}^4$	5.0%	0.3
A of linear elastic longitudinal beam elements (10 r.v.)	Lognormal	$12.22\mathrm{m}^2$	5.0%	0.3
E of linear elastic longitudinal beam elements (10 r.v.)	Lognormal	$28337.46\frac{\mathrm{N}}{\mathrm{mm}^2}$	5.0%	0.3
G of linear elastic longitudinal beam elements (10 r.v.)	Lognormal	$11376.35\frac{\mathrm{N}}{\mathrm{mm}^2}$	5.0%	0.3
J_x of linear elastic longitudinal beam elements (10 r.v.)	Lognormal	$0.146\mathrm{m}^4$	5.0%	0.3
I_y of linear elastic longitudinal beam elements (10 r.v.)	Lognormal	$7.49\mathrm{m}^4$	5.0%	0.3
I_z of linear elastic longitudinal beam elements (10 r.v.)	Lognormal	$7.49\mathrm{m}^4$	5.0%	0.3

Table A.3 Uncertain parameters in I-880 testbed bridge model, part 3

Parameter	Distribution	Mean	C.o.V.	Correlation
Stiffness of x-direction soil spring under elements 141 and 142 (1 r.v.)	Lognormal	$1.030 \cdot 10^6$ kN/m	10.0%	N/A
Stiffness of y-direction soil spring under elements 141 and 142 (1 r.v.)	Lognormal	$8.965 \cdot 10^5$ kN/m	10.0%	N/A
Stiffness of z-direction soil spring under elements 141 and 142 (1 r.v.)	Lognormal	$2.1724 \cdot 10^6$ kN/m	10.0%	N/A
Stiffness of x-rotation soil spring under elements 141 and 142 (1 r.v.)	Lognormal	$5.4692 \cdot 10^7 \frac{\mathrm{kN\,m}}{\mathrm{rad}}$	10.0%	N/A
Stiffness of y-rotation soil spring under elements 141 and 142 (1 r.v.)	Lognormal	$5.6403 \cdot 10^7 \frac{\mathrm{kN\,m}}{\mathrm{rad}}$	10.0%	N/A
Stiffness of z-rotation soil spring under elements 141 and 142 (1 r.v.)	Lognormal	$4.8223 \cdot 10^7 \frac{\mathrm{kN\,m}}{\mathrm{rad}}$	10.0%	N/A
Stiffness of x-direction soil spring under elements 151 and 152 (1 r.v.)	Lognormal	$1.064 \cdot 10^5$ kN/m	10.0%	N/A
Stiffness of y-direction soil spring under elements 151 and 152 (1 r.v.)	Lognormal	$1.065 \cdot 10^5$ kN/m	10.0%	N/A
Stiffness of z-direction soil spring under elements 151 and 152 (1 r.v.)	Lognormal	$1.1623 \cdot 10^5$ kN/m	10.0%	N/A
Stiffness of x-rotation soil spring under elements 151 and 152 (1 r.v.)	Lognormal	$1.420 \cdot 10^7 \frac{\mathrm{kN\,m}}{\mathrm{rad}}$	10.0%	N/A
Stiffness of y-rotation soil spring under elements 151 and 152 (1 r.v.)	Lognormal	$1.4232 \cdot 10^7 \frac{\mathrm{kN\,m}}{\mathrm{rad}}$	10.0%	N/A
Stiffness of z-rotation soil spring under elements 151 and 152 (1 r.v.)	Lognormal	$1.004 \cdot 10^7 \frac{\mathrm{kN\,m}}{\mathrm{rad}}$	10.0%	N/A

Table A.4 Uncertain parameters in I-880 testbed bridge model, part 4

Parameter	Distribution	Mean	C.o.V.	Corr.
Stiffness of x-direction soil spring under elements 161 and 162 (1 r.v.)	Lognormal	$1.065 \cdot 10^5$ kN/m	10.0%	N/A
Stiffness of y-direction soil spring under elements 161 and 162 (1 r.v.)	Lognormal	$1.066 \cdot 10^5$ kN/m	10.0%	N/A
Stiffness of z-direction soil spring under elements 161 and 162 (1 r.v.)	Lognormal	$1.1728 \cdot 10^5$ kN/m	10.0%	N/A
Stiffness of x-rotation soil spring under elements 161 and 162 (1 r.v.)	Lognormal	$1.5937 \cdot 10^7 \frac{\mathrm{kN\,m}}{\mathrm{rad}}$	10.0%	N/A
Stiffness of y-rotation soil spring under elements 161 and 162 (1 r.v.)	Lognormal	$1.595 \cdot 10^7 \frac{\mathrm{kN\,m}}{\mathrm{rad}}$	10.0%	N/A
Stiffness of z-rotation soil spring under elements 161 and 162 (1 r.v.)	Lognormal	$5.0049 \cdot 10^6 \frac{\mathrm{kN\,m}}{\mathrm{rad}}$	10.0%	N/A
Stiffness of x-direction soil spring under elements 171 and 172 (1 r.v.)	Lognormal	$1.2692 \cdot 10^5$ kN/m	10.0%	N/A
Stiffness of y-direction soil spring under elements 171 and 172 (1 r.v.)	Lognormal	$1.2698 \cdot 10^5$ kN/m	10.0%	N/A
Stiffness of z-direction soil spring under elements 171 and 172 (1 r.v.)	Lognormal	$1.3988 \cdot 10^5$ kN/m	10.0%	N/A
Stiffness of x-rotation soil spring under elements 171 and 172 (1 r.v.)	Lognormal	$2.3739 \cdot 10^7 \frac{\mathrm{kN\,m}}{\mathrm{rad}}$	10.0%	N/A
Stiffness of y-rotation soil spring under elements 171 and 172 (1 r.v.)	Lognormal	$2.3790 \cdot 10^7 \frac{\mathrm{kN\,m}}{\mathrm{rad}}$	10.0%	N/A
Stiffness of z-rotation soil spring under elements 171 and 172 (1 r.v.)	Lognormal	$4.1651 \cdot 10^6 \frac{\mathrm{kN\,m}}{\mathrm{rad}}$	10.0%	N/A
Nodal coordinates in x, y and z direction (60 r.v.)	Normal	As is	Stdv= 1.27cm	0.0

Table A.5 40 most important random variables in initial region of load-displacement curve of I-880 testbed bridge

Rank	Importance	Identification of random model parameter						
1	-0.6842	element	1502	material	153	E		
2	0.5816	element	1501	material	153	E		
3	-0.3098	element	1602	material	163	E		
4	0.2463	element	1601	material	163	E		
5	-0.0760	element	1502	material	152	E		
6	-0.0722	element	1501	material	152	E		
7	-0.0688	element	1504	material	154	E		
8	-0.0631	element	1503	material	154	E		
9	-0.0448	element	1402	material	143	E		
10	-0.0386	element	1702	material	173	E		
11	0.0335	element	1701	material	173	E		
12	-0.0319	element	1602	material	162	E		
13	0.0303	element	1401	material	143	E		
14	-0.0298	element	1604	material	164	E		
15	-0.0293	element	1601	material	162	E		
16	-0.0282	element	43	E				
17	-0.0267	element	1603	material	164	E		
18	0.0218	element	152	section	150	material	2	fc
19	-0.0208	element	152	section	150	material	2	epsco
20	0.0205	node	15003	coord	2			
21	-0.0199	node	15002	coord	2			
22	0.0197	element	151	section	150	material	2	fc
23	-0.0188	element	151	section	150	material	2	epsco
24	-0.0183	element	143	E				
25	0.0179	node	15005	coord	2			
26	0.0170	element	142	section	140	material	2	fc
27	-0.0166	element	42	Iy				
28	-0.0163	element	43	Iy				
29	-0.0160	element	142	section	140	material	2	epsco
30	-0.0144	node	15001	coord	2			
31	-0.0134	element	152	E				
32	-0.0122	element	43	Iz				
33	-0.0109	element	152	Iz				
34	0.0106	element	162	section	160	material	2	fc
35	-0.0104	element	142	E				
36	-0.0100	element	162	section	160	material	2	epsco
37	-0.0097	element	151	Iz				
38	0.0097	element	42	Iz				
39	-0.0095	element	143	Iz				
40	0.0091	node	15005	coord	3			

Table A.6 40 least important random variables in initial region of load-displacement curve

Rank	Importance	Identification of random model parameter							
281	≈ 0.0	element	161	section	160	material	2	epscu
282	≈ 0.0	element	152	section	150	material	2	epscu
283	≈ 0.0	element	151	section	150	material	2	epscu
284	≈ 0.0	element	142	section	140	material	2	epscu
285	≈ 0.0	element	172	section	170	material	1	fcu
286	≈ 0.0	element	171	section	170	material	1	fcu
287	≈ 0.0	element	162	section	160	material	1	fcu
288	≈ 0.0	element	161	section	160	material	1	fcu
289	≈ 0.0	element	152	section	150	material	1	fcu
290	≈ 0.0	element	151	section	150	material	1	fcu
291	≈ 0.0	element	142	section	140	material	1	fcu
292	≈ 0.0	element	141	section	140	material	1	fcu
293	≈ 0.0	element	172	section	170	material	1	epscu
294	≈ 0.0	element	171	section	170	material	1	epscu
295	≈ 0.0	element	162	section	160	material	1	epscu
296	≈ 0.0	element	161	section	160	material	1	epscu
297	≈ 0.0	element	152	section	150	material	1	epscu
298	≈ 0.0	element	151	section	150	material	1	epscu
299	≈ 0.0	element	142	section	140	material	1	epscu
300	≈ 0.0	element	141	section	140	material	1	epscu
301	≈ 0.0	node	17999	coord	2			
302	≈ 0.0	node	17998	coord	2			
303	≈ 0.0	node	17998	coord	1			
304	≈ 0.0	node	14999	coord	3			
305	≈ 0.0	node	14998	coord	3			
306	≈ 0.0	node	14998	coord	2			
307	≈ 0.0	element	48	Iy				
308	≈ 0.0	element	40	Iy				
309	≈ 0.0	element	40	G				
310	≈ 0.0	element	48	A				
311	≈ 0.0	node	14999	coord	2			
312	≈ 0.0	node	14999	coord	1			
313	≈ 0.0	element	49	Iz				
314	≈ 0.0	element	41	Iy				
315	≈ 0.0	element	49	Jx				
316	≈ 0.0	element	41	Jx				
317	≈ 0.0	element	40	Jx				
318	≈ 0.0	element	41	E				
319	≈ 0.0	element	40	E				
320	≈ 0.0	element	49	A				

Table A.7 40 most important random variables in yielding region of load-displacement curve of I-880 testbed bridge

Rank	Importance	Identification of random model parameter						
1	-0.6280	element	141	section	140	material	3	sigmaY
2	-0.5633	element	142	section	140	material	3	sigmaY
3	-0.2808	element	151	section	150	material	3	sigmaY
4	-0.2268	element	1502	material	153	E		
5	0.1711	element	142	section	140	material	2	fc
6	-0.1611	element	152	section	150	material	3	sigmaY
7	0.1428	element	142	section	140	material	2	epscu
8	-0.1360	element	1602	material	163	E		
9	0.1234	element	142	section	140	material	1	fc
10	-0.1188	element	161	section	160	material	3	sigmaY
11	0.0729	element	152	section	150	material	2	fc
12	-0.0656	element	162	section	160	material	3	sigmaY
13	0.0584	element	141	section	140	material	2	fc
14	-0.0541	element	1502	material	152	E		
15	-0.0489	element	141	section	140	material	3	b
16	-0.0451	element	142	section	140	material	1	epsco
17	0.0414	element	142	section	140	material	2	epsco
18	0.0361	element	162	section	160	material	2	fc
19	-0.0324	element	142	section	140	material	3	b
20	0.0312	element	152	section	150	material	1	fc
21	0.0282	element	162	section	160	material	2	epscu
22	-0.0266	element	141	section	140	material	3	E
23	-0.0254	node	14002	coord	2			
24	-0.0252	element	1602	material	162	E		
25	0.0247	node	14005	coord	2			
26	0.0246	element	152	section	150	material	2	epscu
27	0.0244	element	151	section	150	material	2	fc
28	0.0243	element	162	section	160	material	1	fc
29	-0.0204	element	142	section	140	material	3	E
30	-0.0187	element	151	section	150	material	3	b
31	-0.0182	element	152	section	150	material	1	epsco
32	-0.0160	node	15002	coord	2			
33	-0.0159	element	152	section	150	material	3	E
34	-0.0142	element	151	section	150	material	3	E
35	-0.0128	element	1702	material	173	E		
36	-0.0118	element	153	Iz				
37	0.0106	node	15005	coord	2			
38	-0.0106	element	153	E				
39	-0.0106	element	171	section	170	material	3	sigmaY
40	0.0104	element	1501	material	153	E		

Table A.8 40 least important random variables in yielding region of load-displacement curve of I-880 testbed bridge

Rank	Importance	Identification of random model parameter						
281	≈ 0.0	element	48	G				
282	≈ 0.0	node	14999	coord	3			
283	≈ 0.0	node	14998	coord	3			
284	≈ 0.0	element	40	Jx				
285	≈ 0.0	element	40	Iz				
286	≈ 0.0	element	49	Jx				
287	≈ 0.0	element	49	G				
288	≈ 0.0	node	14998	coord	1			
289	≈ 0.0	node	17998	coord	3			
290	≈ 0.0	element	48	Iz				
291	≈ 0.0	element	48	Iy				
292	≈ 0.0	element	41	Jx				
293	≈ 0.0	element	41	G				
294	≈ 0.0	node	17998	coord	2			
295	≈ 0.0	element	48	A				
296	≈ 0.0	node	14999	coord	2			
297	≈ 0.0	element	172	section	170	material	1	fcu
298	≈ 0.0	element	171	section	170	material	1	fcu
299	≈ 0.0	element	162	section	160	material	1	fcu
300	≈ 0.0	element	161	section	160	material	1	fcu
301	≈ 0.0	element	152	section	150	material	1	fcu
302	≈ 0.0	element	151	section	150	material	1	fcu
303	≈ 0.0	element	142	section	140	material	1	fcu
304	≈ 0.0	element	141	section	140	material	1	fcu
305	≈ 0.0	element	172	section	170	material	1	epscu
306	≈ 0.0	element	171	section	170	material	1	epscu
307	≈ 0.0	element	162	section	160	material	1	epscu
308	≈ 0.0	element	161	section	160	material	1	epscu
309	≈ 0.0	element	152	section	150	material	1	epscu
310	≈ 0.0	element	151	section	150	material	1	epscu
311	≈ 0.0	element	142	section	140	material	1	epscu
312	≈ 0.0	element	49	A				
313	≈ 0.0	element	41	Iz				
314	≈ 0.0	element	48	Jx				
315	≈ 0.0	element	48	E				
316	≈ 0.0	element	40	A				
317	≈ 0.0	element	141	section	140	material	1	epscu
318	≈ 0.0	element	40	G				
319	≈ 0.0	element	41	Iy				
320	≈ 0.0	node	17998	coord	1			

Table A.9 Summary of member properties used in elastic dynamic analysis (Chapter 7)

	BENT #	A (ft^2)	$(I_{xx})_{gross}$ (ft^4)	$(EI_{xx})_{eff}$ ($x10^8$ kip-ft^2)	$(I_{xx})_{eff}$ (ft^4)	$(I_{yy})_{gross}$ (ft^4)	$(EI_{yy})_{eff}$ ($x10^7$ kip-ft^2)	$(I_{yy})_{eff}$ (ft^4)
Cap	**10**	101.1	793.7	2.06	354.9	1253.0	NA	NA
	11	96.3	615.3	1.75	301.5	1197.0	NA	NA
	12	96.3	757.9	2.02	348.0	1306.0	NA	NA
	13	72.6	320.4	0.97	167.5	1087.0	NA	NA
	14	82.4	313.7	1.00	172.3	1420.0	NA	NA
	15	88.7	419.2	1.13	194.7	1721.0	NA	NA
	16	73.6	290.9	0.86	148.2	1059.0	NA	NA
	17	73.6	290.9	0.86	148.2	1059.0	NA	NA
	18	73.6	313.3	0.73	125.8	1054.0	NA	NA
	19	73.6	313.3	0.73	125.8	1054.0	NA	NA
Col	**10 Lt**	68.0	409.4	0.57	98.3	362.7	5.29	91.24
	10 Rt	68.0	409.4	0.64	110.0	362.7	6.03	104.05
	11 Lt	68.0	409.4	0.60	103.9	362.7	5.63	96.98
	11 Rt	68.0	409.4	0.63	108.5	362.7	5.81	100.10
	12 Lt	68.0	409.4	0.72	123.3	362.7	6.78	116.86
	12 Rt	68.0	409.4	0.69	119.7	362.7	6.51	112.19
	13 Lt	68.0	409.4	0.62	107.5	362.7	5.81	100.22
	13 Rt	68.0	409.4	0.62	107.5	362.7	5.81	100.22
	14 Lt	68.0	409.4	0.62	107.6	362.7	5.82	100.34
	14 Rt	68.0	409.4	0.62	107.6	362.7	5.82	100.34
	15 Lt	68.0	409.4	0.53	91.4	362.7	4.92	84.77
	15 Rt	68.0	409.4	0.53	91.4	362.7	4.92	84.77
	16 Lt	68.0	409.4	0.54	93.6	362.7	5.04	86.93
	16 Rt	68.0	409.4	0.54	93.6	362.7	5.04	86.93
	17 Lt	68.0	409.4	0.56	96.0	362.7	5.29	91.24
	17 Rt	68.0	409.4	0.56	96.0	362.7	5.29	91.24
	18 Lt	52.5	246.1	0.37	63.7	214.4	3.40	58.67
	18 Rt	52.5	246.1	0.37	63.7	214.4	3.40	58.67
	19 Lt	52.5	246.1	0.36	62.3	214.4	3.33	57.35
	19 Rt	52.5	246.1	0.36	62.3	214.4	3.33	57.35
	20 Lt	52.5	246.1	0.36	62.1	214.4	3.32	57.23
	20 Rt	52.5	246.1	0.36	62.1	214.4	3.32	57.23

Table A.10 Summary of force and deformation demands in substructure elements

Column Forces, Moments and Displacements

Member		DL Axial Reaction	Max Shear Force		Moment		Displacement	
			Longitudinal	Transverse	Longitudinal	Transverse	Longitudinal	Transverse
		(kips)	(kips)	(kips)	(kip-ft)	(kip-ft)	(in)	(in)
Bent 10 Left	Top	677.0	420.0	423.9	0.0	0.0	12.38	12.56
	Bottom	1027.9	567.6	555.8	28007.0	27764.4	0.43	0.42
Bent 10 Right	Top	3512.1	2061.8	1848.1	74986.0	64219.0	12.40	12.63
	Bottom	4038.5	2284.6	2039.4	37614.0	36494.0	2.39	2.18
Bent 11 Left	Top	1598.1	2247.7	1759.3	64326.0	51005.0	12.29	9.34
	Bottom	2115.5	2430.2	1893.3	54811.0	41996.0	1.38	1.07
Bent 11 Right	Top	2633.0	2460.0	1879.4	69255.0	53418.0	12.33	9.34
	Bottom	3150.5	2642.0	2011.8	60643.0	45638.0	1.39	1.05
Bent 12 Left	Top	2314.9	2435.1	1668.5	73505.0	50198.0	12.27	8.67
	Bottom	2839.2	2624.2	1812.3	57007.0	39627.0	1.42	0.98
Bent 12 Right	Top	2495.6	2434.7	1640.4	73292.0	49269.0	12.36	8.68
	Bottom	3019.9	2626.0	1784.2	57264.0	39119.0	1.41	0.97
Bent 13 Left	Top	1968.7	720.1	1252.8	39975.0	41171.0	12.34	10.08
	Bottom	2509.1	935.4	1435.6	4348.0	30519.0	1.38	1.18
Bent 13 Right	Top	1884.7	733.2	1251.0	40700.0	41089.0	12.39	10.12
	Bottom	2425.1	952.0	1433.4	4415.0	30498.0	1.35	1.19
Bent 14 Left	Top	1988.2	1883.2	2342.8	46418.0	58101.0	7.38	9.43
	Bottom	2516.0	2001.9	2472.7	54530.0	66951.0	0.43	0.47
Bent 14 Right	Top	1995.3	1843.7	2343.6	45416.0	58129.0	7.36	9.44
	Bottom	2523.0	1960.8	2473.5	53446.0	66964.0	0.43	0.47
Bent 15 Left	Top	1908.7	1241.4	1143.1	34199.0	23451.0	7.40	10.67
	Bottom	2417.6	1402.5	1292.5	32040.0	37664.0	2.48	2.31
Bent 15 Right	Top	1888.1	1230.9	1148.7	33921.0	23672.0	7.39	10.75
	Bottom	2397.0	1390.7	1298.5	31757.0	37730.0	2.48	2.34
Bent 16 Left	Top	1751.3	1361.8	1365.2	35548.0	23585.0	7.40	12.47
	Bottom	2241.3	1518.8	1515.3	33900.0	45947.0	2.68	2.66
Bent 16 Right	Top	2166.4	1350.7	1372.8	35272.0	23871.0	7.41	12.55
	Bottom	2656.4	1506.4	1523.4	33609.0	46030.0	2.67	2.70
Bent 17 Left	Top	1817.4	1441.2	2043.6	30517.0	32395.0	7.36	14.10
	Bottom	2276.1	1574.6	2201.7	37547.0	63411.0	2.38	3.29
Bent 17 Right	Top	1959.1	1426.3	2053.7	30170.0	32744.0	7.37	14.19
	Bottom	2417.8	1558.7	2212.2	37207.0	63512.0	2.39	3.34
Bent 18 Left	Top	2023.5	1769.5	1464.6	36735.0	23644.0	8.91	10.59
	Bottom	2344.4	1892.1	1552.1	38037.0	37996.0	3.29	2.71
Bent 18 Right	Top	2023.4	1765.8	1463.4	36676.0	23619.0	8.93	10.44
	Bottom	2344.2	1888.1	1550.9	37939.0	37984.0	3.28	2.65
Bent 19 Left	Top	1836.6	2078.5	1022.2	39409.0	14651.0	8.87	6.42
	Bottom	2128.9	2194.4	1083.1	40024.0	24531.0	3.76	1.93
Bent 19 Right	Top	1832.0	2071.9	1022.9	39278.0	14663.0	8.88	6.28
	Bottom	2124.3	2187.4	1083.7	39903.0	24538.0	3.77	1.87
Bent 20 Left	Top	1735.9	1398.6	407.0	0.0	0.0	8.89	2.99
	Bottom	1975.4	1474.2	431.5	43769.0	12776.0	2.60	0.83
Bent 20 Right	Top	1758.2	1393.8	407.1	0.0	0.0	8.91	2.71
	Bottom	1997.7	1469.2	431.5	43621.0	12778.0	2.61	0.75